JOURNAL OF ADVANCES IN

ENGINEERING AND TECHNOLOGY

VOLUME II, ISSUE I
OCTOBER 2023

ISSN 2961 - 5410

Civil Engineering | Electrical and Electronic Engineering | Materials Engineering | Mechanical Engineering | Mechatronics Engineering | Quantity Surveying

About the Journal of Advances in Engineering and Technology

The Journal of Advances in Engineering and Technology (JAET) is an international, open access, double blind peer-reviewed journal. It is published by the Faculty of Engineering of Sri Lanka Institute of Information Technology (SLIIT). The JAET aims at fostering research and development work in Engineering and Technology and bringing researchers on to a common platform. Furthermore, JAET will also accept review articles on appropriate subject areas including concept papers of academic opinions, book reviews, etc. for publication therein.

The views and opinions expressed by the authors are their own and would not necessarily reflect the views of the Faculty of Engineering. The research articles submitted to JAET have not been nor envisaged to be published elsewhere and will not simultaneously be published elsewhere. It is also stated that at time of acceptance to publish an article submitted to JAET, the authors agree that the copyright for their accepted articles is transferred to JAET. The copyright covers the exclusive right to reproduce and distribute the article in any form by JAET without the permission of the author.

Notes for the authors: Please see page VI.

All correspondence should be addressed to:

Editor-in-Chief
Journal of Advances in Engineering and Technology
Faculty of Engineering
SLIIT
Kandy Road, Malabe, 10115
Sri Lanka

Email: **jaet@sliit.lk**

Official website: **https://jaet.sliit.lk**

ISSN 2950-7138 (Printed)

ISSN 2961 - 5410 (Online)

Journal of Advances in Engineering and Technology

Volume II, Issue I, October 2023

Contents

ISSN 2961 - 5410 (Online) |

Journal of Advances in Engineering and Technology (JAET)

Volume II Issue (I)-2023

Sri Lanka Institute of Information Technology
Malabe, Sri Lanka

Faculty of Engineering

Sri Lanka Institute of Information Technology (SLIIT)

Malabe, 10115, Sri Lanka

EDITORIAL TEAM

ISSN 2961 - 5410 (Online) |

Notes to the Authors

Journal of Advances in Engineering and Technology (JAET) is a biannual peer review journal which aims at publishing original, theoretical and practice-oriented research papers related to Engineering and Technology. This journal provides a forum for researchers, scholars, academicians, and practitioners in the field of Engineering at international level to discuss and disseminate their findings in advanced and emerging technologies in Engineering.

Articles/ contributions should be sent to:

Editor-in-Chief
Journal of Advances in Engineering and Technology (JAET)
Faculty of Engineering
SLIIT, New Kandy Road, Malabe, Sri Lanka
E – mail: jaet@sliit.lk

- Your article will be subjected to a double-blind review process by two reviewers who are experts in their relevant field. In order to facilitate anonymous review process, you are requested to provide the title page separately.
- The title page should include the title of the article, your full name, affiliation, address, email and telephone/ mobile number.
- Recommendations of two reviewers are necessary for the publication of your article.
- The article should not exceed 6,000 words.
- Abstract should be between 150-200 words with 4-5 keywords.
- Article should include the following:
- Introduction to the research statement/ background to the research/ rationale
- Methods and Material
- Results and Discussion
- Conclusions and Recommendations
- References
- Footnotes can be numbered and given at the end of the article.
- Referencing should conform to the APA style.
- Tables/ graphs should be included in the appropriate places. Longer tables should be added at the end of the article as annexes.
- Use Times New Roman Fonts - Abstract 11pt; Article 11pt; Spacing Single

Evaluation of Mechanical Characteristics of Rice-Husk-Bricks

Ravindu S. Tilakasena
Department of Civil Engineering, Sri Lanka Institute of Information Technology
New Kandy Road, Malabe, 10115, Sri Lanka
ravindutilakasena@gmail.com

G Tharmarajah
Department of Civil Engineering, Sri Lanka Institute of Information Technology
New Kandy Road, Malabe, 10115, Sri Lanka
gobithas.t@sliit.lk

ABSTRACT

Construction activities and materials extraction are major contributors to environmental pollution. To address this issue, the utilization of bio-based materials presents a promising sustainable alternative for the construction industry. Bio-based materials encompass a broad category of organic matter that can be either synthesized or naturally derived. One such noteworthy bio-based material is rice husk, which exhibits pozzolanic properties. Abundantly available as an agricultural waste product, rice husk holds potential as a viable substitute in construction processes. This study is dedicated to investigating the feasibility of replacing fine aggregates, traditionally comprised of sand, in cement blocks with untreated rice husk on a volumetric basis. In contrast to being used merely as an additive, this research delves into the possibility of substantially replacing sand with a higher proportion of rice husk, ranging from 20% to 80%, in the composition of cement blocks. The findings of this study reveal that up to 40% of the sand content in cement blocks can be effectively replaced with untreated rice husk while still meeting the requisite strength standards for non-load bearing blocks. Moreover, this study demonstrates an additional advantage in terms of weight reduction. Substituting sand with rice husk leads to a remarkable 30% reduction in the overall weight of the blocks. These results underscore the potential benefits of integrating rice husk into construction materials as an environmentally friendly and weight-efficient alternative.

KEYWORDS: *bio-based materials, rice husk, fine aggregate, SLS 855, BS EN 771*

1 INTRODUCTION

Construction sector holds a significant position in Sri Lanka's economy, being a major contributor. According to Karunaratne (2021), approximately 9% of the country's gross domestic product (GDP) in 2018 originated from construction-related activities. These activities, however, come with environmental implications. The production of construction materials and the upkeep of buildings collectively account for roughly 28% of the global carbon dioxide (CO2) emissions (Global Alliance for Buildings and Construction & United Nations Environment Programme, 2018). A report from the UK Green Building Council highlights an alarming yearly consumption of over 400 million tons of construction materials (The Environmental Impact of Construction - ProHort, 2020). Construction industry heavily relies on primary resources like sand, timber, and cement, which are mainly obtained through virgin sources. In Sri Lanka, the demand for sand in construction reaches around 40 million cubic meters, significantly surpassing the sustainable supply threshold of 10 million cubic meters. This scenario presents a complex challenge to the construction sector, as it not only strains legal and sustainable sand mining practices but also poses a potential threat to the environment.

ISSN 2961 - 5410 (Online) |https://doi.org/10.54389/ZFMV6827

Figure 1 (a) Timbercrete block (Reproduced from timbercrete.com.au, 2023)

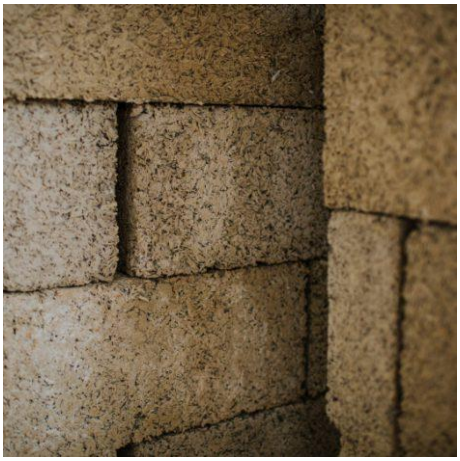

Figure 1(b) Hempcrete blocks (Reproduced from H.G Matthews Limited, 2023)

Preserving the environment and mitigating pollution are pivotal factors in ensuring the ongoing sustenance of life. Our commitment to the environment is essential for upholding the long-term viability of materials and resources. Given this context, there has been a growing emphasis on the utilization of bio-wastes as viable construction materials. Coir, hemp, and corn starch (Abdullah & Lee, 2017; Arnaud & Gourlay, 2012; Asasutjarit et al., 2007; Caruso et al., 2021; Chabannes et al., 2014; Geetha & Selvakumar, 2019; Hettiarachchi & Thamarajah, 2020; Jeyaraj & Tharmarajah, 2019) represent some commonly explored bio-wastes that offer potential alternatives to traditional construction materials. Across numerous developed nations, a tangible trend of using sawdust-based masonry blocks (timbercrete.com.au, 2023) and hemp-derived materials (H.G Matthews Limited, 2023) for both residential and commercial construction purposes (Figure 1a,b) can be observed.

Similarly, rice husks present a notable avenue for integration into masonry blocks, either partially or entirely substituting sand. Rice husks constitute the outer layer of the rice grain, separated during the cleansing process in rice mills. In 2017, Sri Lanka harvested approximately 5.15 million metric tons (MT) of paddy (Department of Census and Statistics, 2018), with rice husks accounting for around 20% of the paddy's weight (Singh, 2018). Regrettably, a significant portion of the annual 1 million MT of rice husks generated, becomes discarded waste in landfills. The potential of rice husks extends beyond waste, as they can be employed in incineration for heat and thermal energy generation, and even for electricity production due to their elevated calorific value (Zou & Yang, 2019).

Rice husks contain approximately 20% amorphous silica (Mansaray & Ghaly, 1997; Nair et al., 2008; Yogananda & Jagadish, 1988), with pozzolanic properties. This characteristic has led to numerous experimental investigations (Ganesan et al., 2008; Hossain et al., 2018; Makul, 2019; Rodríguez De Sensale, 2006; Saraswathy & Song, 2007; Tharshika et al., 2019) evaluating the potential of rice husk ash as an alternative binder, partially replacing cement. However, studies exploring the direct application of raw rice husk in civil engineering contexts remain scarce. A majority of these studies are confined to areas such as lightweight concrete and the creation of wall panels (Abdullah & Lee, 2017; Chabannes et al., 2014; Jauberthie et al., 2003; Liu et al., 2021; Obilade, 2014; Tamba et al., 2000). A preliminary exploration by Jeyaraj and Tharmarajah (2019) revealed that incorporating rice husk up to 23% of a masonry block's volume does not compromise its strength.

Ordinarily, cement blocks used in construction contain a mixture of cement and sand at a 1:6 ratio to achieve requisite strength. Consequently, approximately 85% of the mixture's volume comprises sand. If rice husk were to replace sand entirely without compromising strength, a considerable quantity of sand used in masonry block manufacturing could be conserved.

This study focuses on utilizing untreated rice husk as a substitute for fine aggregate (sand) in the production of rice husk blocks, with cement serving as the binding agent. Sand was gradually replaced

with rice husk at levels of 20%, 40%, 60%, and 80% by volume. The compressive strength of these diverse blocks was assessed and compared to gauge their performance.

2 EXPERIMENTAL INVESTIGATION

The primary constituents of the block encompass cement, sand, unprocessed rice husk sourced from rice mills, and water. Four distinct blends were subjected to testing, adopting mix ratios of 1:6 for cement to aggregate, while varying the proportions of rice husk to replace sand. The substitutions were made at rates of 20%, 60%, 70%, and 80% of rice husk based on the total volume of the fine aggregate (refer to Figure 2).

Figure 2: The composition of the block

2.1 Materials

2.1.1 Cement

Commercially available ordinary Portland cement was used for the study. Typical chemical composition of the cement is given in Table 1.

Table 1: Chemical composition of ordinary Portland cement

	SiO2	**Al2O3**	**Fe2O3**	**CaO**	**MgO**	**K2O**	**Na2O**	**SO3**	**LOI**	**TiO2**	**Free CaO**
Cement	19.70 %	5.18%	2.76%	65.13 %	0.69 %	0.99 %	0.17 %	2.85 %	1.51 %	-	1.31%

2.1.2 Rice husk

Rice Husk (RH) is the leafy outer covering of the seed, about 20-25% of the total weight. RH reflects a more spherical shape with a width between 1-4 mm and the maximum length is to be about 0.01m. Natural RH contains 75% organic compound and 25% of inorganic compound. Out of the organic compound percentage 45-60% Cellulose/Hemi-cellulose and 25-30% Lignin according to past literature. RH contains minor rate of open interior porosity. RH is considered by very minor pores under 0.1 μm and nearly no pores were detected for RH from 1μm to 30μm. Typical composition of the rice husk is given in Table 2.

Table 2: Composition of the rice husk

	Cellulose	**Hemicelluloses**	**Lignin**	**Extractives**	**Silica ash**
Rice Husk	25-35%	18-21%	26-31%	2-5%	15-25%

Cement blocks were prepared using cement block casting machine to the size 350 mm × 180 mm × 100 mm. After 24 hours, they were removed from the moulds and allowed for curing under wet conditions for 28 days. After curing, the blocks were tested for density and compressive strength as part of this preliminary investigation. Four different compositions were used for the experiments as shown in Table 3.

ISSN 2961 - 5410 (Online) |

Table 3: Ratio of cement: sand: rice husk by volume

Sample	Cement	Sand	Rice Husk
R1	1	4.8	1.2
R2	1	3.6	2.4
R3	1	2.4	3.6
R4	1	1.2	4.8

The content of the rice husk was increased while reducing the sand content by replacing sand with the rice husk. The water cement ratio was 0.3 for R1 samples and was increased to 0.5 as rice husk content increased. For each composition, 9 cellular-block samples were prepared and tested for 7-day, 14-day and 28-day strength.

Similarly, the density of the bricks was obtained by measuring the weight and volume of the brick on three samples of each composition.

3 RESULTS

3.1 Compressive strength

Figure 3 illustrates the compressive strength of the masonry blocks throughout the 7-day, 14-day, and 28-day curing periods. Notably, a linear upsurge in strength is observed in blocks containing 20% added rice husk. However, a distinct strength gain profile is evident in blocks incorporating 40%, 60%, and 80% rice husk fibers. Up to the 14-day mark, the rate of strength gain remains comparable across all four compositions, with a subsequent decline in this rate observed beyond the 14-day curing period. Despite uniform cement content across all compositions, the deceleration in strength gain can be attributed to various factors linked to rice husk and the availability of water for the hydration process.

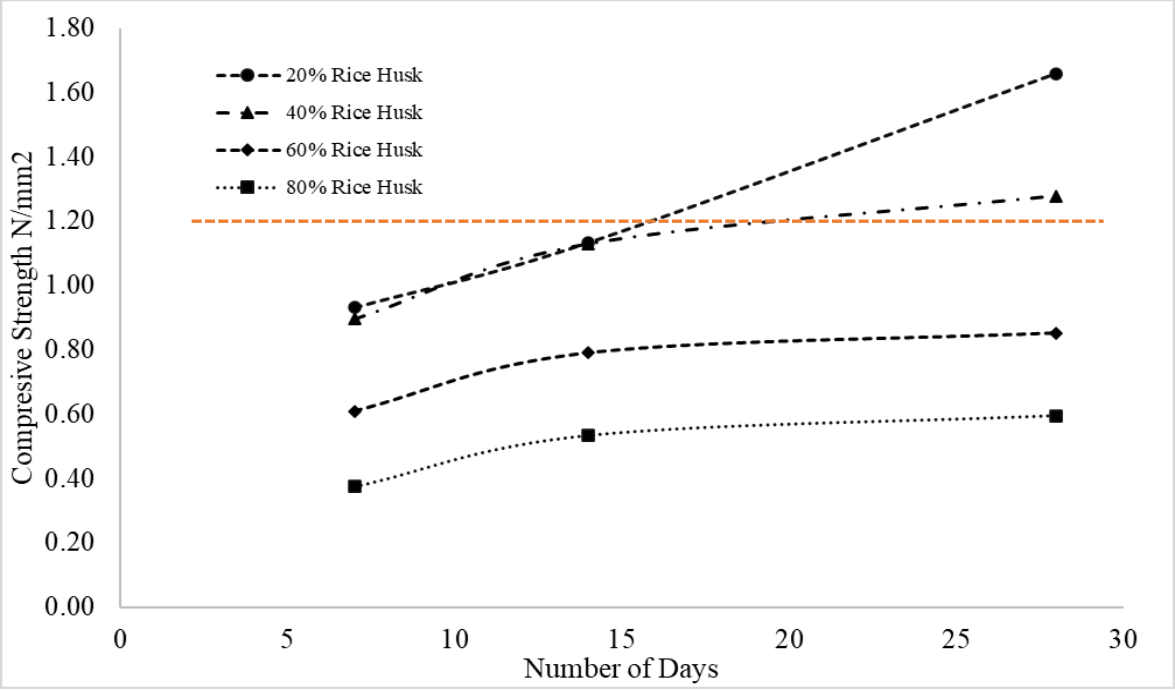

Figure 3: Strength increment with the number of days of curing

Among the tested compositions, the blocks with 40% rice-husk demonstrate sufficient strength as per SLS 855 (SLS 855, 1989). SLS 855 recommends a minimum of 1.2 N/mm^2 for masonry blocks. Although other blocks with higher rice-husk content do not demonstrate sufficient strength after 28 days, there is a possibility for enhancement of strength with longer curing periods. This requires further investigation.

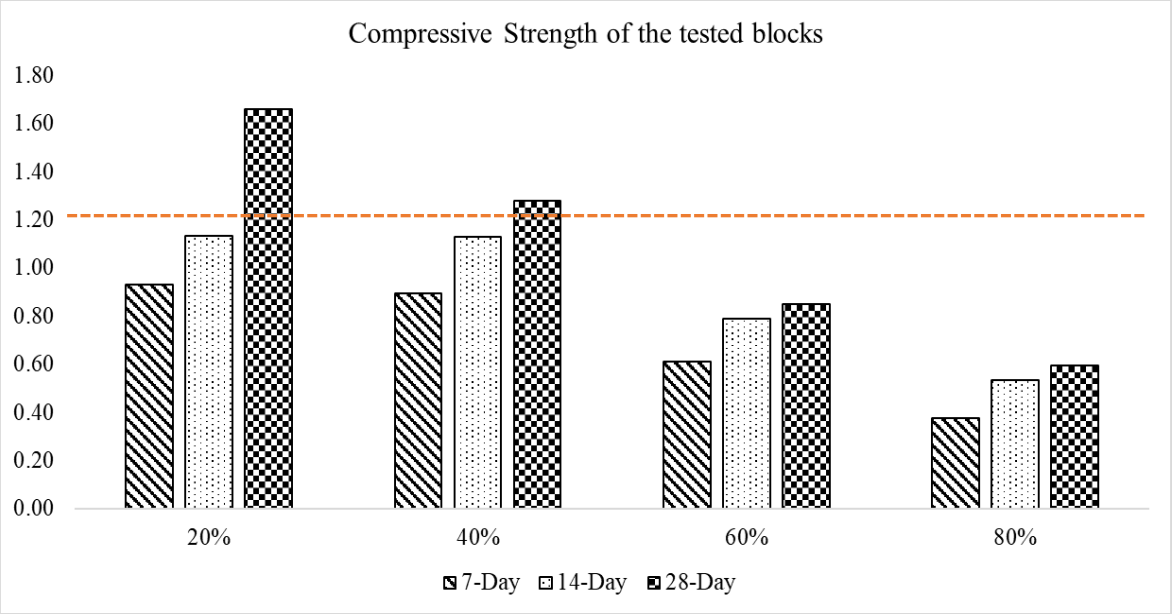

Figure 4: Compressive strength of all the tested blocks

3.2 Density

The wet density of the test blocks was measured by calculating the weight of the specimens. The change in density with time is shown in Figure 5. It can be seen from Figure 5 that the density of all the specimens were lesser than the average density of 2100 kg/m^3 recorded for commercially available cement blocks.

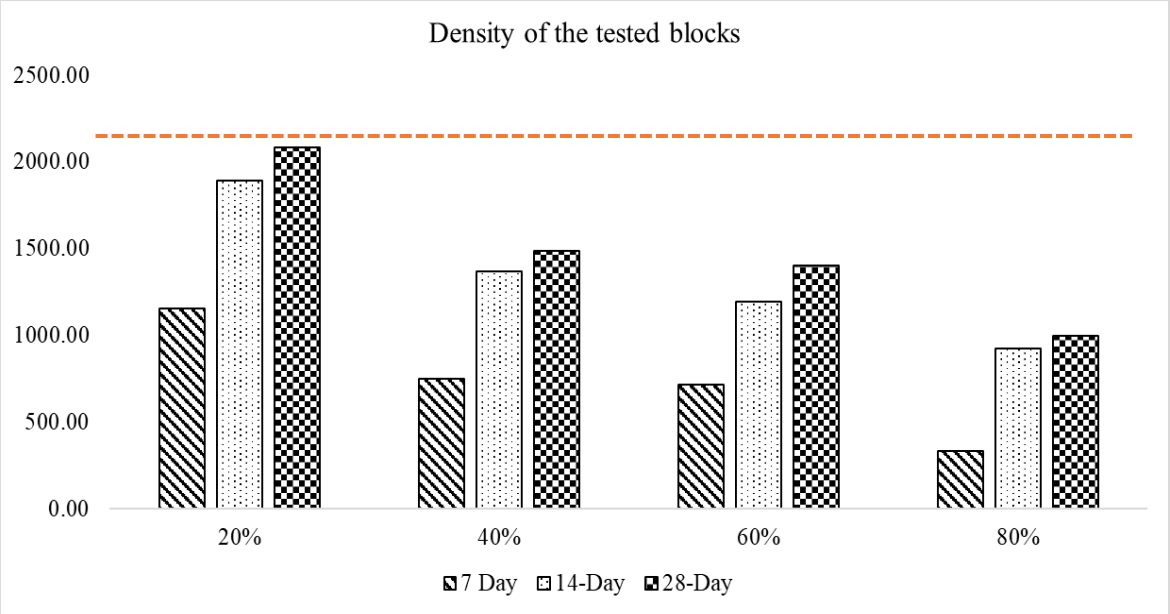

Figure 5: Density of the masonry blocks

ISSN 2961 - 5410 (Online) |

It can also be seen that the density of the blocks increased with the number of days of curing. However, the change in density between 14-day and 28-day was lesser in all the samples. Compared to the control value of 2100 kg/m^3 the blocks with 40% rice husk have 30% lesser density while satisfying the strength required for masonry blocks.

4 DISCUSSION

Lightweight cement blocks are commonly manufactured using autoclaved aerated concrete (AAC) technology. Existing literature reveals that AAC blocks exhibit compressive strengths ranging from 2.3 N/mm^2 to 7.0 N/mm^2 across diverse compositions, while densities span from 425 kg/m^3 to 700 kg/m^3 (Pachideh & Gholhaki, 2019; Yang & Lee, 2015). Commercial lightweight cement blocks available in the market showcase compressive strengths surpassing 2.5 N/mm^2, with dry densities ranging between 700 kg/m^3 and 800 kg/m^3 (Tokyo Cement Group, 2022). The production of AAC blocks involves intricate procedures and specialized equipment to achieve such lightness. Interestingly, the inclusion of rice husk indirectly amplifies block porosity, resulting in density reduction.

Various design codes prescribe distinct strength criteria for masonry blocks. The Australian code (AS/NZ 4455, 2008) stipulates a minimum of 3.0 N/mm^2 for solid or vertically cored non-load bearing units. Correspondingly, the Eurocode (BS EN 771, 2016) mandates a minimum strength of 1.5 N/mm^2 for load bearing AAC blocks or other lightweight variants. Sri Lanka's standards (SLS 855, 1989) advocate for 1.2 N/mm^2 in non-load bearing cement blocks. A comparative analysis of these code requisites reveals that units replacing 20% of sand with rice husk meet the strength specifications of both SLS 855 and BS EN 771 recommendations. Both 20% and 40% rice husk-added units satisfy the SLS requirement for non-load bearing masonry blocks.

When contrasted with conventional commercially available cement blocks, both 20% rice husk-added and 40% rice husk-added units exhibit lower density, attributable to the incorporation of rice husk. On a broader scale, it becomes apparent that substituting sand with rice husk in masonry units at a volume of 40% of the total sand demonstrates potential as a feasible option.

5 CONCLUSION

This study focused on evaluating compressive strength and wet density of cement blocks produced using cement, fine aggregate and rice husk. Rice husk replaced the sand on volumetric basis up-to 80% to evaluate the compressive strength and wet density. The following conclusions were obtained from the study.

1. Both 20% and 40% rice-husk added cement blocks demonstrated a similar strength up-to 14 days. However, the strength of 40% sand replaced with rice-husk specimen achieved a lower strength than 20% rice-husk added specimen at 28-day.
2. Compressive strength of 20% and 40% rice husk added samples satisfy the SLS 855 strength requirement for non-load bearing cement blocks. It can be noticed that 20% rice-husk added samples satisfy both BS EN 771:4 and SLS 855 requirements.
3. It can be seen from Figure 5 that the wet density decreases with the increase of rice husk percentage. The densities increased with the number of days of curing. This can be attributed to the addition of raw rice husk and its absorption of water.
4. The study indicates the possibility of using rice-husk to replace sand in cement blocks up-to 40% of the volume. Further studies can be carried out to enhance the strength and durability characteristics.

6 ACKNOWLEDGEMENTS

Authors would like to acknowledge the support provided by the Department of Civil Engineering, Faculty of Engineering, SLIIT for the experimental investigation and other facilities.

REFERENCES

Abdullah, A. C., & Lee, C. C. (2017). Effect of Treatments on Properties of Cement-fiber Bricks Utilizing Rice Husk, Corncob and Coconut Coir. *Procedia Engineering*. https://doi.org/10.1016/j.proeng.2017.04.288

Arnaud, L., & Gourlay, E. (2012). Experimental study of parameters influencing mechanical properties of hemp concretes. *Construction and Building Materials*, *28*(1). https://doi.org/10.1016/j.conbuildmat.2011.07.052

Asasutjarit, C., Hirunlabh, J., Khedari, J., Charoenvai, S., Zeghmati, B., & Shin, U. C. (2007). Development of coconut coir-based lightweight cement board. *Construction and Building Materials*. https://doi.org/10.1016/j.conbuildmat.2005.08.028

AS/NZ 4455, :1. (2008). *Masonry units, pavers, flags and segmental retaining wall units. Part 1, Masonry units*. Standards Australia ; Standards New Zealand.

BS EN 771, :4. (2016). *Specification for masonry units Autoclaved aerated concrete masonry units* (Confirmed).

Caruso, M., Cefis, N., Dotelli, G., & Sabbadini, S. (2021). Mechanical characterization of hemp-lime blocks. *AIP Conference Proceedings*, *2343*. https://doi.org/10.1063/5.0048116

Chabannes, M., Bénézet, J. C., Clerc, L., & Garcia-Diaz, E. (2014). Use of raw rice husk as natural aggregate in a lightweight insulating concrete: An innovative application. *Construction and Building Materials*, *70*. https://doi.org/10.1016/j.conbuildmat.2014.07.025

Department of Census and Statistics, S. L. (2018). *Paddy Statistics—Maha Season* (pp. 1–3). Government of Sri Lanka.

Ganesan, K., Rajagopal, K., & Thangavel, K. (2008). Rice husk ash blended cement: Assessment of optimal level of replacement for strength and permeability properties of concrete. *Construction and Building Materials*, *22*(8). https://doi.org/10.1016/j.conbuildmat.2007.06.011

Geetha, S., & Selvakumar, M. (2019). Properties of Aerated Hempcrete as a potential sustainable Building Material. *IOP Conference Series: Materials Science and Engineering*, *577*(1). https://doi.org/10.1088/1757-899X/577/1/012074

Global Alliance for Buildings and Construction & United Nations Environment Programme. (2018). *2018 Global Status Report*.

Hettiarachchi, C., & Thamarajah, G. (2020). Effect of Surface Modification and Fibre Content on the Mechanical Properties of Coconut Fibre Reinforced Concrete. *Advanced Materials Research*, *1159*, 78–99. https://doi.org/10.4028/www.scientific.net/AMR.1159.78

H.G Matthews Limited. (2023). *Hempcrete Blocks*. https://www.hgmatthews.com/lime-and-cob/natural-building-blocks/hempcrete-blocks/

Hossain, S. K. S., Mathur, L., & Roy, P. K. (2018). Rice husk/rice husk ash as an alternative source of silica in ceramics: A review. *Journal of Asian Ceramic Societies*, *6*(4). https://doi.org/10.1080/21870764.2018.1539210

Jauberthie, R., Rendell, F., Tamba, S. E., & Cissé, I. K. (2003). Properties of cement—Rice husk mixture. *Construction and Building Materials*, *17*(4). https://doi.org/10.1016/S0950-0618(03)00005-9

Jeyaraj, K. D., & Tharmarajah, G. (2019). Alternative Masonry Blocks using Rice Husk and Fly Ash. *Annual Transactions of Institution of Engineers*, 81–89.

Karunaratne, C. S. (2021). Sri-Lanka The Construction Industry: 1995–2019. In M. Anson, Y. H. Chiang, P. Lam, & J. Shen (Eds.), *Construction Industry Advance and Change: Progress in Eight Asian Economies Since 1995* (pp. 163–182). Emerald Publishing Limited. https://doi.org/10.1108/978-1-80043-504-920211008

Liu, X., Li, J., Li, F., Wang, J., & Lu, H. (2021). Study on the Properties of an Ecotype Mortar with Rice Husks and Sisal Fibers. *Advances in Civil Engineering*, *2021*. https://doi.org/10.1155/2021/5513303

Makul, N. (2019). Combined use of untreated-waste rice husk ash and foundry sand waste in high-performance self-consolidating concrete. *Results in Materials*, *1*. https://doi.org/10.1016/j.rinma.2019.100014

ISSN 2961 - 5410 (Online) |

Mansaray, K. G., & Ghaly, A. E. (1997). Physical and thermochemical properties of rice husk. *Energy Sources*, *19*(9). https://doi.org/10.1080/00908319708908904

Nair, D. G., Fraaij, A., Klaassen, A. A. K., & Kentgens, A. P. M. (2008). A structural investigation relating to the pozzolanic activity of rice husk ashes. *Cement and Concrete Research*, *38*(6), 861–869. https://doi.org/10.1016/j.cemconres.2007.10.004

Obilade, I. O. (2014). Experimental Study On Rice Husk As Fine Aggregates In Concrete. *The International Journal Of Engineering And Science (IJES)*, *3*(8).

Pachideh, G., & Gholhaki, M. (2019). Effect of pozzolanic materials on mechanical properties and water absorption of autoclaved aerated concrete. *Journal of Building Engineering*, *26*, 100856. https://doi.org/10.1016/j.jobe.2019.100856

Rodríguez De Sensale, G. (2006). Strength development of concrete with rice-husk ash. *Cement and Concrete Composites*, *28*(2). https://doi.org/10.1016/j.cemconcomp.2005.09.005

Saraswathy, V., & Song, H. W. (2007). Corrosion performance of rice husk ash blended concrete. *Construction and Building Materials*, *21*(8). https://doi.org/10.1016/j.conbuildmat.2006.05.037

Singh, B. (2018). 13—Rice husk ash. In R. Siddique & P. Cachim (Eds.), *Waste and Supplementary Cementitious Materials in Concrete* (pp. 417–460). Woodhead Publishing. https://doi.org/10.1016/B978-0-08-102156-9.00013-4

SLS 855, P. I. (1989). *Cement blocks—Requirements* (Code No. 855). Sri Lanka Standards Institution.

Tamba, S. E., Cissé, I. K., Rendell, F., & Auberthie, R. (2000). Rice Husk in Light Weight Mortars. *Second International Symposium on Structural Light Weight Concrete*, 117–127.

Tharshika, S., Thamboo, J. A., & Nagaretnam, S. (2019). Incorporation of untreated rice husk ash and water treatment sludge in masonry unit production. *Sustainable Environment Research*, *1*(1). https://doi.org/10.1186/s42834-019-0010-y

The Environmental Impact of Construction—ProHort. (2020, August 25). https://prohort.co.uk/the-environmental-impact-of-construction/

timbercrete.com.au. (2023). *Mud Brick Alternative*. https://timbercrete.com.au/building-products/mud-brick-alternative

Tokyo Cement Group. (2022). *Cellular Lightweight Concrete Blocks*. Tokyo Cement Group.

Yang, K.-H., & Lee, K.-H. (2015). Tests on high-performance aerated concrete with a lower density. *Construction and Building Materials*, *74*, 109–117. https://doi.org/10.1016/j.conbuildmat.2014.10.030

Yogananda, M. R., & Jagadish, K. S. (1988). Pozzolanic properties of rice husk ash, burnt clay and red mud. *Building and Environment*, *23*(4), 303–308. https://doi.org/10.1016/0360-1323(88)90036-4

Zou, Y., & Yang, T. (2019). Rice husk, rice husk ash and their applications. In *Rice Bran and Rice Bran Oil: Chemistry, Processing and Utilization*. https://doi.org/10.1016/B978-0-12-812828-2.00009-3

Development of a Simplified Method of Designing Pervious Concrete Mixes using chip aggregate

B. J. S. Fernando
Department of Civil Engineering, Faculty of Engineering, University of Moratuwa
jsfernando78@gmail.com.

D. Naanayakkara
Department of Civil Engineering, Faculty of Engineering, University of Moratuwa
dn@uom.lk

ABSTRACT

Pervious concrete can be referred to a sustainable paving material which reduces urban runoff, heat-island effect and improves the ground water quality. Due to the lack of awareness and the unavailability of a simplified design method, the applications are limited in the local context. In this research study, a new method of preparing pervious concrete mixes using commercially available chip aggregate together with coarse aggregate was developed. Five volume based binary combinations were prepared with varying coarse aggregate and chip aggregate proportions. A simple mix design method which is based on the porosity of the pervious concrete was used to determine the required cement paste content. For each aggregate combination, cement paste contents were calculated for four different design porosities. Overall, twenty pervious concrete mixes were prepared and test specimens for compressive strength, bending strength and permeability tests were conducted. Based on the test results, relationships between aggregate combination, compressive strength, permeability, and cement paste content were identified and a simplified graphical method of designing pervious concrete mixes to achieve required strength and permeability characteristics was introduced. Further, the addition of chip aggregate enhanced the strength characteristics while retaining adequate permeability.

KEYWORDS: *Chip aggregate, Coarse aggregate, Pervious concrete, Cement paste, Mix design.*

1 INTRODUCTION

Pervious concrete [PC] is a special concrete which has a higher void content with interconnected pore structure that allows water to pass through. With rapid urbanization, most of the earth's surface is covered with impermeable pavements reducing the storm water infiltration which results in ponding and excessive runoffs while affecting ground water quality. PC is used as a pavement material which is an effective remedy for controlling excessive runoff, flash floods and ponding. Also, PC differs from the conventional concrete as it contains little or no fine aggregate which leads to sustainable aspects as it saves natural resources. PC has excellent antiskid properties. The presence of interconnected pore structure ensures improved heat and humidity exchange than conventional pavement hence the possibility of a considerable reduction in the "Heat-Island effect". (Tun et al.,2014).

Considering the properties, PC has relatively lower density in a range of 1600kg/m^3 – 2000kg/m^3. Typically, the porosity of PC varies between 15%-35%. Relatively lower values of W/C ratio than conventional concrete are selected for PC mixes which vary between 0.27-0.4 in general. The coefficient of permeability of PC varies between 0.2 mm/s-5.4 mm/s (Nguyen, 2014). Due to high porosity, the compressive strength of PC is lower than the compressive strength of conventional concrete hence applicable where lesser loads are applied. It is used as a paving material for parking lots, walkways, foot paths, light traffic areas, slope stabilisation systems etc. (Tun et al.,2014). Typically, the compressive strength of PC generally varies between 5 MPa- 30MPa and flexural strength varies between 1 MPa- 3.5 MPa (Mohammed, 2016).

Lower compressive strength and the absence of a simplified mix design method have limited the applications of PC. Though many studies have been carried out globally, there are limited studies in the

ISSN 2961 - 5410 (Online) | https://doi.org/10.54389/BJON1401

local context. Development of a simplified mix design method is difficult due to the lack of data obtained by experimental studies. The objective of this research is to study the variation of strength and permeability with aggregate content and cement paste content and how chip aggregate can be used to enhance the strength characteristics of PC.

2 STRATEGIES TO ENHANCE STRENGTH CHARACTERISTICS

To improve the performance of PC which can expand its applications, it is mandatory to enhance the compressive strength of PC. The strength characteristics depend on the microstructure of PC as it governs the load transferring mechanism. Figure 1 shows a generalized model of Pervious Concrete.

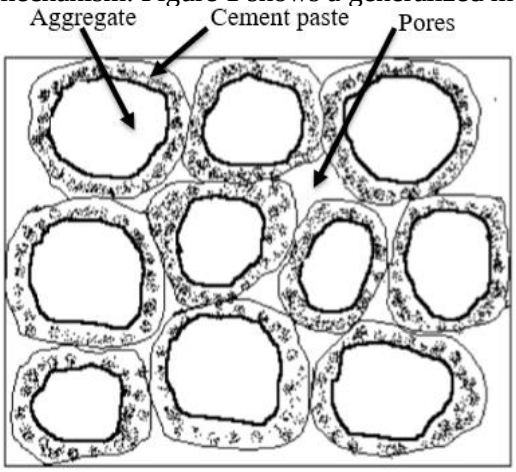

.

Figure 1: Pervious Concrete model

Quantified results about the microstructure of PC can be obtained by means of X-ray microtomography. Experimental studies have concluded that mechanical properties of PC primarily depend on the properties of the aggregate (Ayda, 2013). Coarse aggregate effectively contributes to form the skeleton structure. A study on crack pattern using X-ray microtomography has shown, a higher tendency to develop cracks through the cement paste when the used aggregate is finer (Cosic, 2015). Based on the literature survey, the following strategies can be adopted to enhance the strength characteristics of PC (Jing, 2003).

- **Enhancing the binder strength**

With the presence of pores, cement paste becomes thinner which results in lower compressive strength. There are micro-pores and microcracks in cement paste and the presence of those in transition zone significantly contributes to the reduction of strength. Mineral admixtures and intensifiers such as Silica fume, fly ash can be used to improve the micro-structure which enhance bond properties (Jing, 2003).

- **Increasing the binder area**

Using a smaller aggregate, particle density can be increased in order to increase the specific surface area.. This increases the binder area resulting in an improvement of the strength (Tiejun et al., 2019).
A majority of studies used a narrow range particle size of coarse aggregate. In this study, the full range of commercially available coarse aggregate was used considering the practical means. Particles finer than 4mm were removed as well as particle greater than 20mm, to avoid the reduction of permeability and strength respectively. To enhance the strength by increasing the binder area, commercially available aggregates smaller than 10mm which is known as chips were also added to remove particles finer than 4mm. In the design of PC, strength and permeability are the major considerations and the cement paste content and aggregate content are the governing factors for these properties.

3 METHODOLOGY

3.1 Materials

- Cement: Rapid flow cement with strength class 42.5 N/mm^2
- Coarse Aggregate (CA): Commercially available coarse aggregate in the size range of 4mm - 20mm
- Chips: A type of commercially available coarse aggregate having smaller size range (< 10mm). For this study, particles finer than 4mm were removed.
- No fine aggregate was used in this study.

3.2 Mix design

Five volume based binary combinations of CA and chips were used in this study. CA and chips were volumetrically proportioned as 0%:100%. 25%:75%, 50%:50%, 75%:25% and 100%:0% which were coded as combination A, B, C, D, and E respectively. PC was designed using a simple approach which is mainly based on the porosity of PC (Sumanasooriya, 2012). Porosity of the relevant compacted sample of CA and chips was found to be approximately 40% for every combination.

Table 1: Porosity of the compacted aggregate

Chips: CA	**Code**	**Porosity of compacted aggregate sample (%)**
100:0	A	40.10
75:25	B	41.17
50:50	C	38.68
25:75	D	39.40
0:100	E	41.98

The design porosity of PC was varied as 0.1m^3/ m^3, 0.15 m^3/ m^3, 0.2 m^3/ m^3 and 0.25 m^3/ m^3. After the selection of design porosity value and determination of the porosity of the compacted aggregate, the required paste content per 1 m^3 of PC can be calculated as follows.

*Total Void Volume = Design porosity + cement paste conten*t (1)

Since the total void content per 1m^3 of the compacted aggregate is known, if the design porosity is decided, the design cement paste content can be determined using the above equation. Throughout this study, W/C ratio was kept constant and W/C of 0.3 was used based on the literature (Cosic, 2015). Then, the required cement mass(x) can be calculated as follows.

$$V_{cement\ paste} = V_{cement} + V_{water} \quad (2)$$

$$V_{cement\ paste} = \frac{x}{Density\ of\ cement} + \frac{0.3x}{Density\ of\ water} \quad (3)$$

4 EXPERIMENTAL STUDY

As mentioned earlier, five volumetric combinations of CA and chips were used in this study and prior to mix design calculation, the porosity of the compacted aggregate sample must be determined. It can be determined using a simple water displacement test with an aggregate sample which has been

ISSN 2961 - 5410 (Online) |

compacted using a similar compaction method used for the trial mixes by filling 1/3 by 1/3 and giving 35 blows per each layer. Per each combination, four PC mixes were batched varying the design porosity as 25%,20%,15% and 10% hence the design paste content varied as well. However, for a particular aggregate combination, aggregate requirement does not vary with the paste content. Aggregate proportions used in this study for $1m^3$ of PC and the numbering code for prepared trial mixes are shown in Table 2 and Table 3, respectively.

Table 2: Aggregate proportions

Aggregate combination	**CA (kg)**	**Chips (kg)**
A	-	1581.36
B	401.51	1164.83
C	837.018	809.424
D	1240.785	399.96
E	1583.946	-

Table 3: PC trial mixes numbering

		Design Porosity			
		25%	**20%**	**15%**	**10%**
Aggregate combination	A	A1	A2	A3	A4
	B	B1	B2	B3	B4
	C	C1	C2	C3	C4
	D	D1	D2	D3	D4
	E	E1	E2	E3	E4

In total, 20 mixes of PC were prepared and for each mix 150mm×150mm×150mm cube specimens and permeability test specimens (100mm radius and 200mm height) were made. To study the variation of the flexural strength of PC, 150mm × 150mm × 750mm beams were made for each aggregate combination. Trial mix A1 was not effective because of the insufficient coating of cement paste. Mixing and compaction method used in Wang et al. (2006) was used in this study (Wang, 2006). All the samples were cured for 28 days and tested for compressive strength, flexural strength, permeability, and porosity in accordance with relevant standards.

5 RESULTS AND DISCUSSION

5.1 Compressive strength

Variation of the compressive strength of PC with cement paste content for different aggregate combinations is plotted as shown in Figure 2. Results show that compressive strength increases with the cement paste content for all the aggregate combinations. Trial mix D4 yielded the highest compressive strength of 38MPa while A2 yielded the lowest strength of 9.9MPa. The compressive strength of B2 and B3 mixes exceeded 35MPa.

Results indicate that, compressive strength can be enhanced by introducing smaller particles which make the aggregate combination more likely well graded hence the formation of the well packed skeleton structure. .

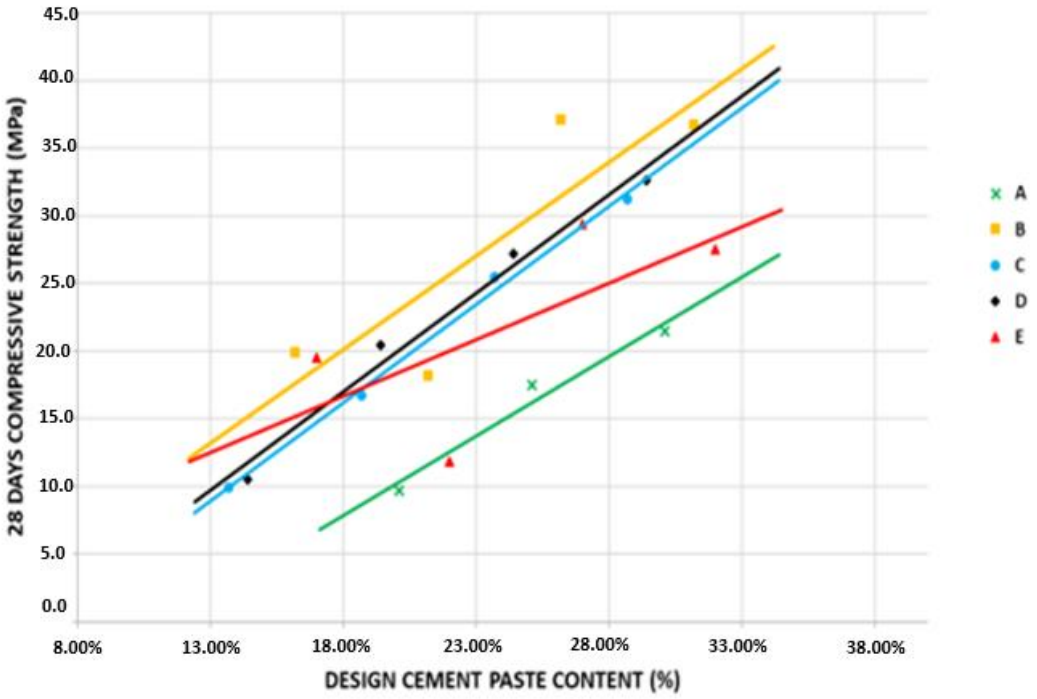

Figure 2 : 28 days compressive strength vs design cement paste content

However, PC mixes made only with smaller particles, show lower compressive strengths. In this study, the strength of the cement paste binder was not improved by using admixtures or intensifiers. Results confirm the fact that the cracks initiate and propagate through the cement paste when a higher fraction of smaller particles is present.

5.2 Permeability

The coefficient of permeability was calculated using Darcy's equation.

$$v = kI \quad (4)$$

Where: v = velocity of the flow
k = coefficient of permeability
I = hydraulic gradient

Using the experimental results, permeability vs design cement paste graphs were plotted as shown in Figure 3.

ISSN 2961 - 5410 (Online) |

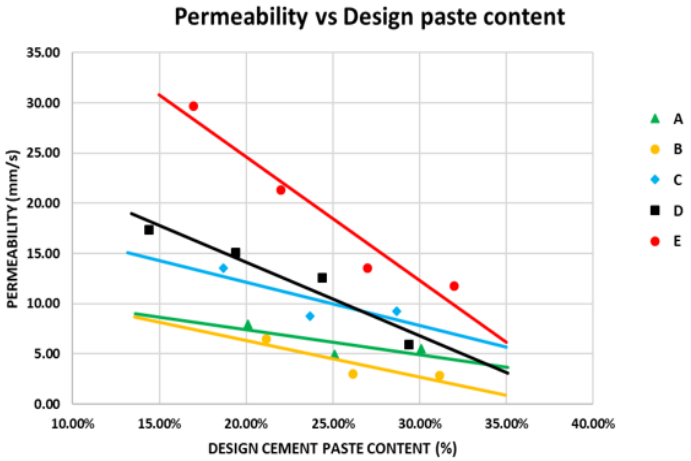

Figure 3: Permeability vs design cement paste content

Aggregate combination A shows the lowest coefficient of permeability whereas combination E has the highest. Permeability decreases when the chip content increases. In combination A, PC mixes were only made with the chip aggregate hence the particles are in a well packed structure, blocking the capillaries. Since combination E has the highest fraction of larger particles, larger sized and more connected pores can be expected. On the other hand, in all aggregate combinations, the coefficient of permeability reduces when the cement paste content increases as a result of the blockage of the interconnected pores.

As observed in the previous section, compressive strength increases with the cement paste content. Therefore, it implies that the higher the compressive strength, lesser the permeability is. However, the requirement of permeability from a PC mix totally depends on the permeability of the underlaying soil layer of the site unless a separate drainage is provided. It is not efficient to have a higher coefficient of permeability than that of the underlaying soil layer. General values of coefficient of permeability are shown in Table 4 (Das, 2015).

Table 4: Range of the Coefficient of permeability for various soils

Type of soil	**Coefficient of permeability *k* (cm/sec)**
Medium to coarse gravel	Greater than 10^{-1}
Coarse to fine sand	10^{-1} to 10^{-3}
Fine sand, silty sand	10^{-3} to 10^{-5}
Silt, clayey silt, silty clay	10^{-4} to 10^{-6}
Clays	10^{-7}

Referring to the experimental results, the least coefficient of permeability obtained was 2.81×10^{-1} cm/s which matches the range of medium to coarse gravel which is positively above the coefficient of permeability of all kinds of subgrades in the local context.

5.3 Flexural strength

A three-point bending test was performed on the specimens cast with a design porosity of 20% for all the aggregate combinations. Results show relatively lower flexural strength values than the typical flexural strength of conventional concrete. Combination C has the highest flexural strength value of 2.64MPa which is approximately half of the typical flexural strength of conventional concrete (Concrete in Practice, 2000). Figure 4 shows the variation between Modulus of rupture and chip percentage, and it indicates that the percentage of chips does not have a significant impact on flexural strength.

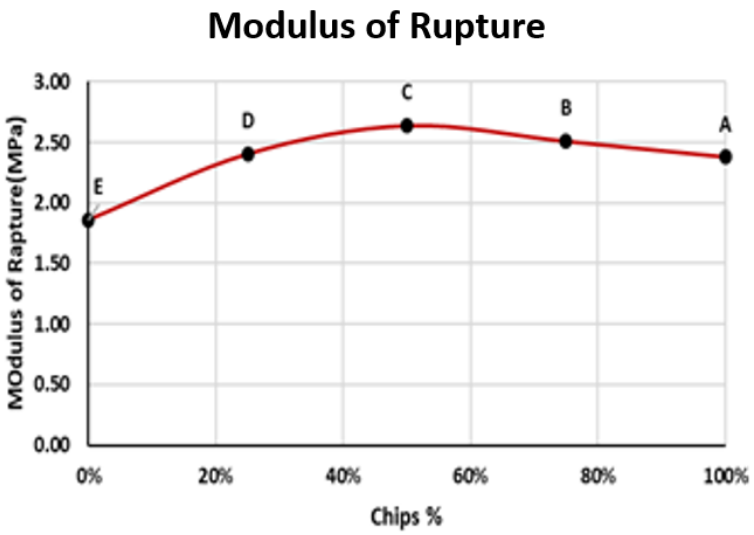

Figure 4: Flexural strength vs chips percentage

5.4 Actual porosity

Referring to the results, the actual porosity vs design porosity graph is plotted as shown in Figure 5. Results show that the actual porosity values are considerably lower than the design values. The porosity was determined using a water displacement method recording the amount of water required to fill the voids. However, the isolated voids may not be accounted for with this method, and it may lead to deviations.

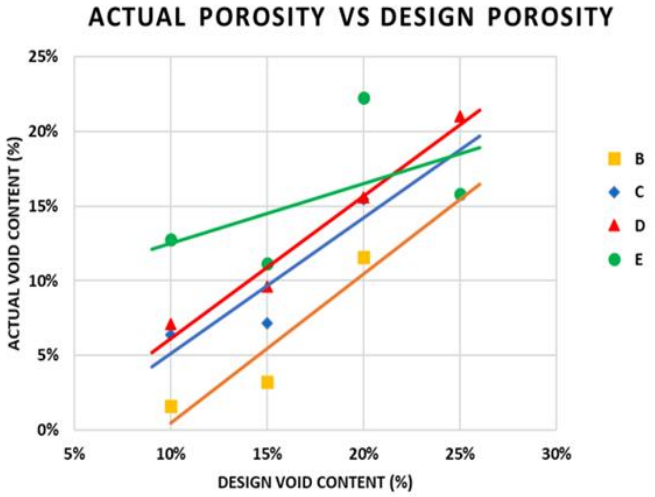

Figure 5: Actual porosity vs design porosity

6 PROPOSED CONCEPTUAL MIX DESIGN METHOD

Using the experimental data obtained and the patterns and relationships between the major parameters observed, a simplified concept of designing PC mixes was developed. The required compressive strength and the permeability are the key input parameters for the proposed method. In order to increase the strength characteristics, combinations of full range of particle sizes of CA and chips were used removing particles finer than 4mm and larger than 20mm. Prior to design, a basic idea about the required permeability which can be estimated considering the soil strata or provided drainage at the proposed site, is needed. Considering the application of the pavement, strength requirement can be obtained. The design concept is to determine a suitable aggregate combination and a cement paste content using the developed compressive strength vs design paste content graph. The selected combinations should be

ISSN 2961 - 5410 (Online) |

checked for the coefficient of permeability using the developed permeability vs design cement paste graph and the adjustment should be made to meet both compressive strength and permeability requirements.

7 CONCLUSION

Applications of PC are limited mainly because of the unavailability of a simplified mix design method which is suitable for local industry and the relatively lower strength characteristics. Enhancing the binder strength and increasing the binder area are the major methods of enhancing the strength characteristics of pervious concrete. In this research study, the full-size range of coarse aggregate and commercially available smaller version of coarse aggregate known as chips were mixed in order to enhance the strength characteristics by increasing the bond area between cement paste and aggregate particle with the means of practicality and simplicity. Results confirmed that PC can be made with relatively higher compressive strength exceeding 30MPa while obtaining adequate coefficient of permeability without using admixtures with this new method. A conceptual method of designing pervious concrete mixes was proposed using experimental results which simplify the design process.
It is recommended to conduct further experimental studies to improve the proposed design method and to further enhance the strength characteristics by enhancing the binder strength which was not studied in this research study.

REFERENCES

Ayda, S. A. O. W. (2013). Investigating porous concrete with improved strength: testing at different scales. *Construction and Building Material*, 480-490.

Das, B. M. (2015). *Principles of foundation engineering.* Cengage Learining.

Concrete in Practice. (2000). *CIP16-Flexural Strength Concrete.* Silver Spring: NRMCA.

Cosic, K. K. L. (2015). Influence of aggregate type and size on properties of pervious concrete. *Construction and Building Materials*, 69-76.

Nguyen, D. H. N. S. (2014). A modified method for the design of pervious concrete mix. *Construction and Building Materials*, 271-282.

Jing, Y. G. J. (2003). Experimental study on properties of pervious concrete pavement materials. *Cement and Concrete Research*, 381–386.

Wang, K. V. R. (2006). Development of mix proportion for functional and durable pervious concrete. *Nashville: Dans Concrete Technology Forum*, 1-12.

Sumanasooriya, M. S. D. O. (2012). Particle packing-based material design methodology for pervious concretes. *ACI materials Journal*, 205-214.

Mohammed S, M. (2016). Pervious Concrete: Mix Design, Properties and Applications. *RILEM Technical Letters*, 109-115.

Tiejun, L., Zhongzhen, W., Dujian, Z., Ao, Z., & Junze, D. (2019). Strength enhancement of recycled aggregate pervious concrete using a cement paste redistribution method. *Cement and Concrete Research, 122*, 72 - 82.

Tun, C. F., Weichung, Y., Jiang, J. C., & Ran, H. (2014). The Influence of Aggregate Size and Binder Material on the Properties of Pervious Concrete. *Hindawi, Advances in Materials Science and Engineering.*

Off-Grid Wind-Solar Hybrid Energy System for Analaitivu Island in Sri Lanka

Nipuna Liyanagama, Dhananjana Ravindra & Priyan Bopitiya
Department of Electrical and Electronic Engineering, Sri Lanka Institute of Information Technology
New Kandy Road, Malabe, 10115, Sri Lanka.
{nlwijesekara, dhananjanaraveendra, priyanbopitiya96}@gmail.com

Kasuni Guruvita
Department of Electrical and Electronic Engineering, Sri Lanka Institute of Information Technology
New Kandy Road, Malabe, 10115, Sri Lanka.
kasuni.g@sliit.lk

ABSTRACT

The objective of this project is to implement an off-grid wind-solar hybrid energy system with a battery bank system for Analaitivu island in Sri Lanka, which has no connection to the main grid. The hybrid model is developed by analyzing the wind-solar weather pattern of the island to fulfill the energy demand by choosing the ideal combination of solar cells and wind generators.

KEYWORDS: *Wind-Solar Hybrid Energy System, Battery Bank System, Off-grid Energy System, Analaitivu Island, Northern Province, Sri Lanka.*

1 INTRODUCTION

Wind-Solar hybrid systems that are used for rural residences are stand-alone systems that operate "off-grid" and are not connected to an electricity distribution system. When solar and wind power resources are used together, reliability is improved, and the continuous system energy service can be enhanced with the battery storage system. When compared to other forms of renewable energy, such as biomass and hydro, solar and wind power stand out for their abundance and limitless potential, as well as the absence of any costs associated with their acquirement.

Islands of Nagadeepa, Delft, Analaitivu, and Eluvaithivu in the northern province of Sri Lanka are primarily recognized as being isolated from the main grid. Eluvaithivu island has already implemented an off-grid wind-solar and diesel generator system. This project proposed an off-grid wind-solar hybrid energy system with a battery bank system for Analaitivu island. The system is capable of fulfilling the power and energy demand of the entire island in an economically viable manner. As a result of Sri Lanka's ongoing political, economic, and energy crisis, people have recently experienced more than 10-hour power cuts. The proposed wind-solar hybrid strategy can also be used in other rural areas of Sri Lanka to address this serious problem.

2 SOLAR AND WIND ENERGY POTENTIAL IN THE NORTHERN PROVINCE

2.1 Site selection

Data was collected from the Ceylon Electricity Board (CEB) on the main islands of Jaffna that have no link to the main grid. Islands of Nagadeepa, Delft, Analaitivu, and Eluvaithivu are already identified as being isolated from the main grid, with Eluvaithivu island having already implemented a wind and diesel-generating hybrid system. Other major islands rely entirely on diesel generators for power. Table 1 shows the power consumption of the main islands that are not connected to the main grid in the northern province of Sri Lanka.

ISSN 2961 - 5410 (Online) |https://doi.org/10.54389/HJWD9157

Table 1: Main islands in the northern province of Sri Lanka that are not connected to the main grid

Island name	**Nagadeepa**	**Delft**	**Analaitivu**
Current Power Source	Diesel generator	Diesel generator	Diesel generator
Population	3545	4583	1832
No. of Houses	1070	1400	574
Daily Power Consumption	3020kWh	2920kWh	1157kWh
Peak time Power Demand	360A	300A	200A
Generator Capacity	250kVA	250kVA	100kVA
	380kVA	250kVA	100kVA
		330kVA	250kVA

These islands are far from the mainland, so it is expensive to establish undersea cables, and it is hard to build high-voltage overhead distribution lines through deep water. Based on daily power usage and peak time demand, Analaitivu island was chosen to deploy the proposed wind-solar hybrid energy system. Ceylon Electricity Board now powers 574 houses on the island using two 100kVA diesel generators and one 250kVA diesel generator. The island of Analaitivu, which is about 25 kilometers west of the city of Jaffna, is off the coast of the Jaffna peninsula as shown in figure 1. The island, which had a colonial name of Rotterdam, is 4.82 square kilometers in size. (Wikipedia contributors, 2020).

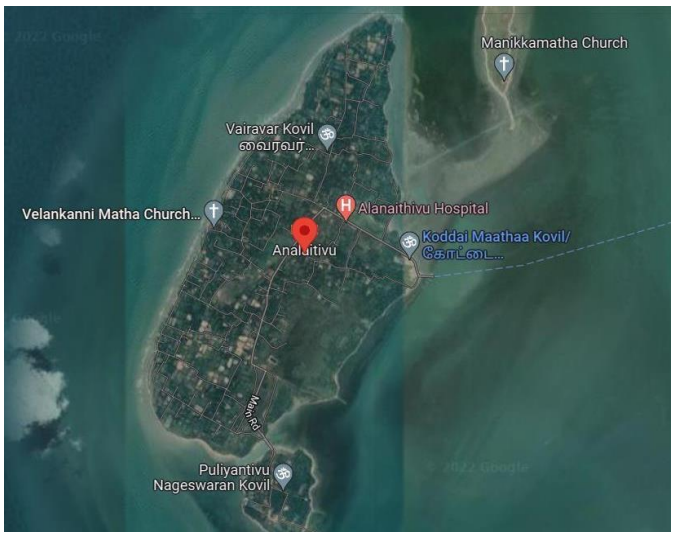

Figure 1: The geographical location of Analaitivu Island

By combining wind and solar energy to create a hybrid power system, the energy demand of the island can be fulfilled. A hybrid power plant needs to be built and optimized to generate electricity at competitive pricing because of the sizable investment cost. Every day, 1157 kWh of power is consumed by the households of Analitivu Island. The monthly usage of the 574 houses ranges from 30000 to 45000 kWh (based on a detailed survey).Each customer has an energy meter attached to their household, and meter readings are taken on a regular basis. However, CEB's operational expenditures for the current diesel power plant are significantly high. The power plant's outdated diesel generators are inefficient leading to diesel wastage since they are never completely loaded. To construct a power system tailored to the island of Analaitivu, precisely forecast of its power requirement is imperative. It should be noted, however, that only 574 individuals are now connected to the system, and the existing electricity supply is only accessible for six and a half hours daily. To ensure efficient and cost-effective use of renewable energy resources, an optimal sizing approach is required. The optimal size approach

can assist in ensuring the lowest investment while making maximum use of the system component, allowing the hybrid system to operate at its best in terms of investment and system power reliability.

2.2 Weather data analysis

Fluctuating solar radiation and wind speed parameters have a significant impact on energy generation in renewable energy systems. Figure 2 and Figure 3 show the Monthly average wind speed data and the solar irradiance pattern of Analaitivu island according to the NASA surface meteorology and solar energy database. (Stackhouse, n.d.)

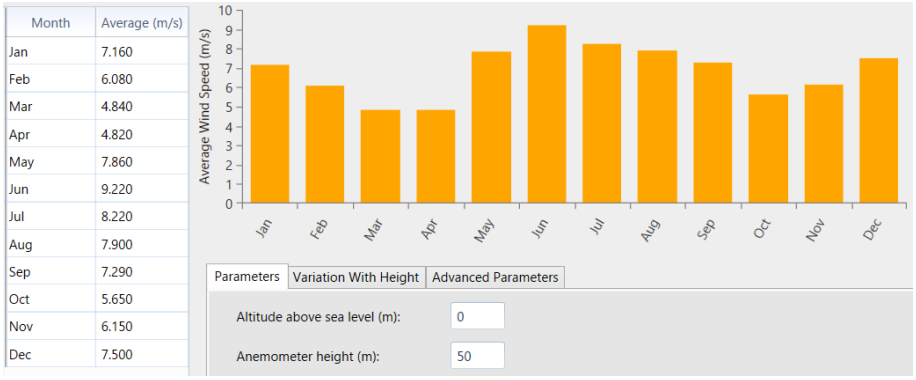

Figure 2: Monthly average wind speed data of Analaitivu island.

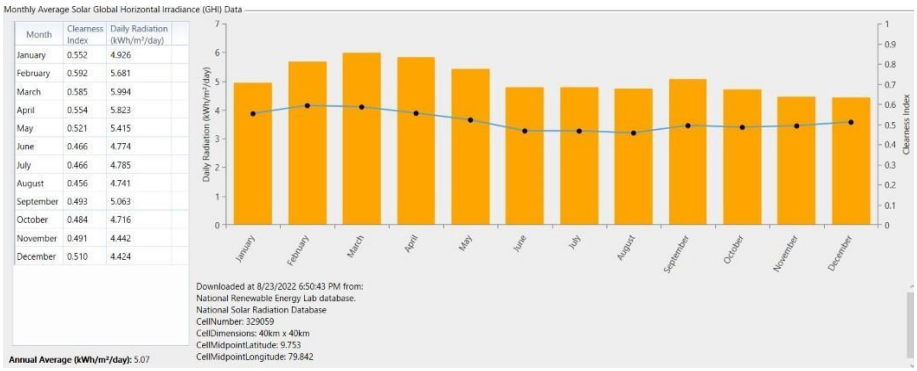

Figure 3: Monthly average solar irradiance pattern of Analaitivu island

The weather on the island is generally similar to the weather in Sri Lanka's northern region. This region mostly experiences rain from October through December. During this season, over 70% of the yearly rainfall occurs. Jaffna peninsula and the islands get notably different yearly rainfall, with 1365mm in Jaffna. 28 °C in December to 33 °C in June being the typical temperatures in the region. (Portal, n.d.). Monthly average temperature data are shown in figure 4.

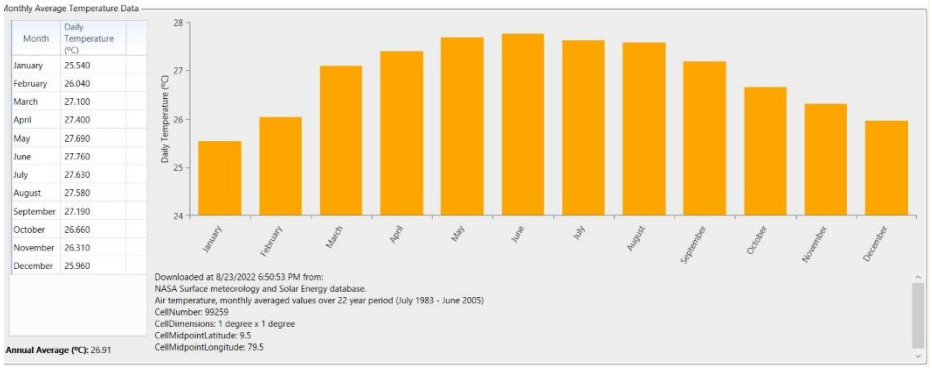

Figure 4: Monthly average temperature data of Analaitivu island

ISSN 2961 - 5410 (Online) |

2.3 Homer optimization

The Hybrid Optimization Model for Electric Renewables (HOMER) is the most commonly used sizing tool created by the National Renewable Energy Laboratory (NREL). This application has been used widely in recent renewable energy system case studies and includes a strong user interface with a full system analysis. HOMER allows users to model PV/wind hybrid systems and conduct sizing and optimization by running the simulation repeatedly and comparing various system setups and component sizes. The electricity produced by renewables, PV and WT, battery charging and discharging, and the computation of the overall net present cost are all based on approximate formulae. After receiving resource data, load data, and power-generating equipment data, as well as the equipment capabilities to be considered, Homer executes a continuous calculation process and ranks the best combinations in priority order based on the discounted lifespan cost. The program offers a selection of locations, and"Analaitivu Island" was selected by providing geographical coordinates. The selected area is located at 09.66912° and 079.776172° geographical coordinates. The data about the site's GHI and temperatures related to the location can be obtained from the resource libraries of Homer software. It is loaded to the database automatically. HOMER software uses imported data to create an approximation of the daily load consumption. Based on the typical electricity usage, the daily load curve is shown in figure 5.

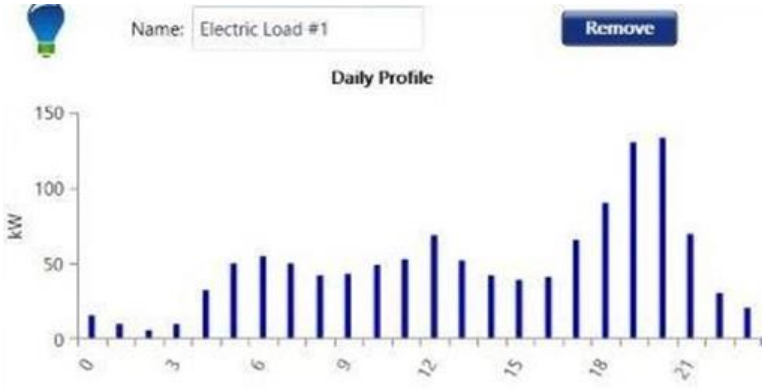

Figure 5: The daily load profile of electricity consumption on Analaitivu island

The daily electrical load curve, which is created to depict the power load as a function of time, is crucial in short-term load forecasting. The plot shows sharp increases in morning, noon, and night, which is noteworthy. Peak demand, which occurs between 6.30 a.m., 12.30 p.m., and 8.30 p.m., is the most critical aspect that must be addressed. The average daily load curve for Sri Lanka has had a clear trend over time, with the load progressively increasing annually.

Table 2: Monthly average electricity consumption on Analaitivu island

Month	**Energy delivery (kWh)**
January	1165.84
February	1123.75
March	1126.97
April	1330.45
May	1020.84
June	1156.97
July	1200.57
August	1157.83
September	1035.67
October	1250.67
November	1160.58
December	1153.96
Average	**1157.008**

Components from HOMER's inventory are available with a set of customizable pricing and capacities. PV cells, wind turbines, batteries, and inverters are the primary components used in this project. Component size, cost, and capacity are further required inputs; however, numerous inputs here enable quantity/capacity optimization. Following a technical review of the components, PV cells, wind generators, and battery cells were selected for installation.

3 SYSTEM DESIGN

3.1 Solar/ Photovoltaic panels

In Homer software, there are several options available when choosing PV panels. The PV catalog lists all the brands available. An estimation of the cost concerning capacity was given by Jinko Eagle PERC60 300W, an electricity provider recognized by Sri Lanka's Sustainable Energy Authority. Sizing optimization was made possible by the addition of multiple capacity options. One of the main factors to consider is the expected lifetime, and according to the Sri Lanka Sustainable Energy Authority, a PV cell is predicted to last 25 years while still performing at an optimal level. Additionally, HOMER sets the panel type to flat, which denotes a zero-degree angle. (ENF Ltd, n.d.).

3.2 Wind turbine

Wind turbine generators are utilized to partially replace the electrical energy produced from solar energy by utilizing the island's significant wind resource. In other words, the solar demand is fairly decreased by retrofitting a wind turbine generator. Although the initial cost of a wind turbine generator is high, the operational cost is extremely low, making the usage of multiple wind turbine generators uneconomical. It was decided to employ two ASW HC wind turbine generators with a capacity of 3.3kW after taking the limitation and the initial investment requirement. into account. (AWS HC Wind Turbines, n.d.)

3.3 Battery bank system

Ion edition LPF 2100Ah Lithium-ion batteries with 100kWh of energy storage each were selected for peak hours. This battery was selected because it has a lifespan of fifteen years and has an initial cost of Rs 710700.00 and Rs 710700.00 replacement cost. The nominal battery capacity is 2100Ah (Homer energy, n.d.). The beginning and minimum states of charge, lifespan, and throughput of this battery are all programmable, but its price is fixed. To fit the battery within the project's concept, the lifetime was set to 15 years.

4 CIRCUIT DIAGRAM

Homer software analyzes the necessary equipment, its sizes, and its usage patterns, and preliminary technical design of the power plant needs to be done to address the precise problems associated with the project's execution. The power flows and fundamental connections between the power plant's components are shown in the schematic design in figure 6.

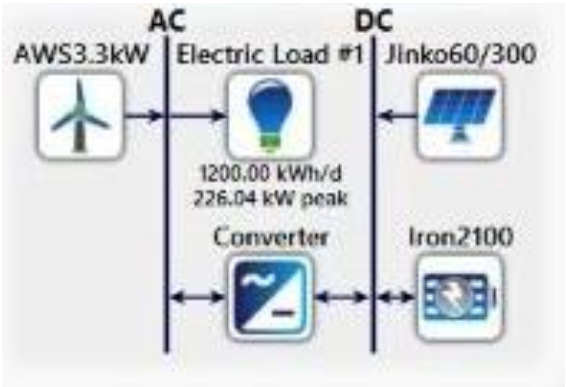

ISSN 2961 - 5410 (Online) |

Figure 6: Schematic design of the system

5 SPECIFICATIONS OF THE PROJECT

Correct equipment size is established after conducting a pre-feasibility study using weather data and the maximum capacity of the system. The dependability and efficiency of an integrated power system are significantly influenced by its unit size. There are several approaches that may be applied to find the most dependable and affordable option. One approach is to use computer modeling and optimization software with inputs for hourly solar radiation, wind speed, and instantaneous efficiency. To discover the optimum solution, another approach uses optimization techniques based on a search methodology. Each use case for a renewable energy system has a unique set of software needs. A pre-feasibility tool is necessary for implementing a renewable energy system since salespeople, promoters, consultants, and planners determine whether a renewable energy system makes sense for a particular application, taking into account both the energy delivered and lifetime cost comparisons of stand-alone systems. Software that calculates the appropriate size for each of the system's numerous components and offers details on system dependability is necessary for designers and installers of renewable energy systems.

The purpose of tool sizing is to specifically lower the life-cycle cost of the system. The end user asks for software that can simulate a renewable energy system's performance under various load and weather scenarios, as well as the capability to contrast predicted outcomes with actual data in order to identify any renewable energy system defects. The inputs supplied to Homer and the assumptions made in giving these inputs have a direct impact on the outputs produced by Homer. As a result, all the technical and economic inputs provided to Homer were either confirmed by obtaining relevant data from the equipment suppliers or were based on logical engineering judgments taking into account the project's background. Figure 7 presents the most reliable technological possibilities according to Net Present Cost (NPC), as determined by Homer software.

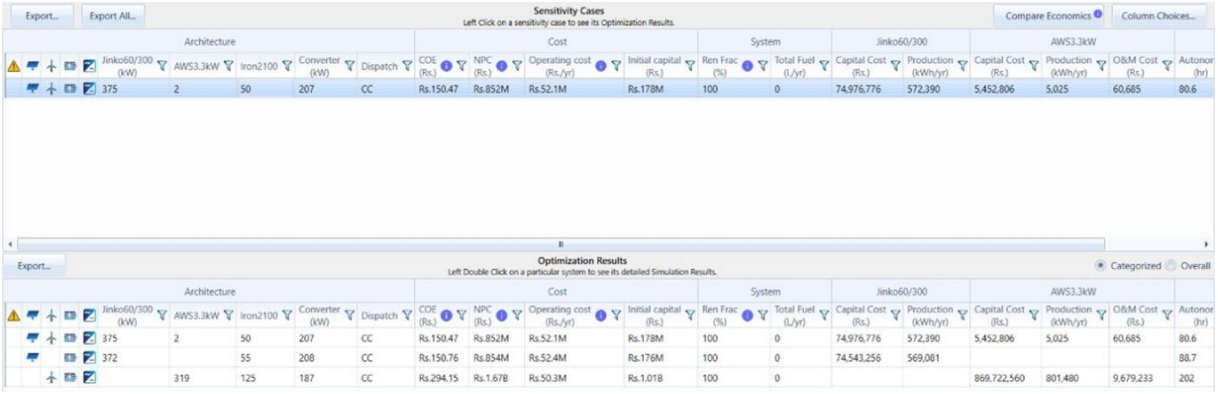

Figure 7: Technology options ranked according to net present cost (NPC)

The winning configuration, as shown in figure 7, is a 375 kW PV system with two 3.3 kW wind generators. As a result, the average power consumption is 1157kWh, hence the plant is designed for 1200kWh. The optimum configuration divided it to have 375 kWh from solar and 6.6 kWh from wind energy. The configuration with a full solar PV system comes in second on the list and is close behind it regarding the reliability of the wind solar hybrid system. As shown in figure 8, the configuration only consists of the wind turbine and can be neglected due to its high NPC value of Rs. 1.67B.

Jinko60/300 (kW)	AWS3.3kW	Iron2100	Converter (kW)	Dispatch	COE (Rs.)	NPC (Rs.)	Operating cost (Rs./yr)	Initial capital (Rs.)
375	2	50	207	CC	Rs.150.47	Rs.852M	Rs.52.1M	Rs.178M
372		55	208	CC	Rs.150.76	Rs.854M	Rs.52.4M	Rs.176M
	319	125	187	CC	Rs.294.15	Rs.1.67B	Rs.50.3M	Rs.1.01B

Figure 8: Cost estimates for the selected power plant configuration

In order to assess the outcome and whether important parameters have deviated from the anticipated values, HOMER is utilized for the sensitivity analysis. Multiple values are entered to do the sensitivity analysis, and then all the variables are optimized. There may be a variation in the outcome once each variable has been optimized, highlighting the influence of the sensitive values. Key characteristics include factors like wind speed and solar hours.

The wind turbine prices considered in the current research are based on those provided by reputable providers in industrialized nations. Accessing affordable wind equipment in the near future appears very likely because of the technological advancements being made in the wind turbine sector in countries like China and India. Therefore, a sensitivity analysis was performed to investigate the effect of component pricing on the successful configuration. This system has a high penetration rate and adaptability to handle any unexpected increases in demand.

6 TECHNO-ECONOMIC ANALYSIS

It is not sufficient to design and select the best configuration for an off-grid solar PV system since the performance of the wind-solar hybrid energy system is also greatly influenced by several financial and performance factors. The following metrics are computed in HOMER software to assess whether building a hybrid system is economically feasible.

6.1 Cost analysis

As is common in any cost-benefit analysis, the objective of the economic analysis is to evaluate the project's economic advantages in comparison to its associated expenses. A financial measurement serves as the benchmark for evaluating costs and benefits. The project's effects are assessed as much as possible in terms of market prices for goods and services. In other words, shadow pricing reflects an effort to shed light on what a good or service costs the economy as a whole.

Table 3 : Cost analysis for the solar PV system

Solar System Capacity - DC (kWp)	**375**	
Panel	**T1 Panel**	
Inverter	**Huawei**	
Exchange Rate	**1US$ = Rs.360**	
	US$	Rs
Total Price including additional	325362	117130320
Features Price per kW	867.632	312347.52
Panels (790)	126400	45504000
Inverters	45084	16230240
Mechanical Structure	18600	6696000
Cables (DC, AC, Earthing)	70800	25488000
Civil & Underground Work	10600	3816000
AC Combiner Box	13600	4896000
Related Insurances	2400	864000
Supplier VAT (@ 15%)	5800	2088000
Others	23000	8280000
Basic System Price	**316284**	**113862240**
Additional Features can be provided at the following prices		
Ladders	1050	378000
Meter Cubicle	2389	860040
Water Line	2250	810000
Inverter Structure	3389	1220040
Additional Features Price	**9078**	**3268080**

ISSN 2961 - 5410 (Online) |

Table 4 : Cost analysis for the wind energy system

Wind System Capacity - DC (kWp)		**6.6**
Generator	**ASW HC 3.3kW**	
Exchange Rate	**1US$ = Rs.360**	
	US$	**Rs**
Total Price including additional	52860	19029600
Features Price per kW	8009.090909	2883272.727
ASW 3.3KW Wind Turbines x 2	50000	18000000
-Blades		
-Hub		
-Mechanical Structure		
-Bearings		
-Rotor		
-AC Combiner Box		
Cables (DC, AC, Earthing)	560	201600
Civil & Underground Work	600	216000
Basic System Price	**51160**	**18417600**
Additional Features can be provided at the following prices		
Ladders	1700	612000
Additional Features Price	**1700**	**612000**

Table 5: Cost analysis for the battery bank system

Battery Bank Capacity - DC	**5050 kWh**	
Battery Capacity (Ah)		**2100 Ah**
Exchange Rate	**1US$ = Rs 360.00**	
	US$	**Rs**
Total Price including additional	101250.0	36450000.00
features Price per kWh	20.04950495	7217.821782
Battery (50 Units)	98708.3	35535000.00
Mechanical Structure (Rack)	708.3	255000.00
Cables (DC, AC, Earthing)	375.0	135000.00
Civil and Battery bank room Work	763.9	275000.00
Related Insurances	138.9	50000.00
Others	555.6	200000
Basic System Price	**101250.0**	**36450000.00**

6.2 BOQ analysis

The Bill Of Quantities also referred to as a "BOQ" is a document that lists the measured values of the work items that are described by the drawings and specifications. This document is created by the cost consultant, who is typically a quantity surveyor.

Table 6: BOQ analysis for the solar PV system

Item	**Description**	**Quantity**
Solar PV Panels	JA/Jinko 475W	790
Inverters	Huawei 100kW with 5 years warranty	3
	Online Monitoring	1
Structure	Aluminum Railing Bars	310
	T Clamp Set	1,400
	Angle Clamp Set	520
	Serrated Angle Bracket	1,500
	Connector Clamp	300
Bus Bar	AC Combiner Box - Venora/EMP	1
Wiring	DC Cables (6mm^2)	Multiple
	AC Cables	Multiple
	Grounding Cables	Multiple
Cable Trays	DC Cable Trays	Multiple
	AC Cable Trays	Multiple
Price includes	Design and Engineering Support for the solar system	
	Installation	
	Additional Features as given	
	Testing and Commissioning	
	Transport and Labour	
	Traveling and Accommodation	

Table 7: BOQ analysis for the wind energy system

Item	**Description**	**Quantity**
Generator	ASW HC 3.3kW	2
Structure	Aluminum Railing Bars	310
	T Clamp Set	1,400
	Angle Clamp Set	520
	Serrated Angle Bracket	1,500
	Connector Clamp	300
Bus Bar	AC Combiner Box - Venora/EMP	1
Wiring	DC Cables (6mm^2)	Multiple
	AC Cables	Multiple
	Grounding Cables	Multiple
Cable Trays	DC Cable Trays	Multiple
	AC Cable Trays	Multiple
Price includes	Design and Engineering Support for the Wind system	
	Installation	

ISSN 2961 - 5410 (Online) |

	Additional Features as given
	Testing and Commissioning
	Transport and Labour
	Traveling and Accommodation

Table 8: BOQ analysis for the battery bank system

Item	**Description**	**Quantity**
Battery	Iron edition LPF 2100Ah	50
Structure	Aluminum Railing Bars	300
	T Clamp Set	
	Angle Clamp Set	
	Serrated Angle Bracket	150
	Connector Clamp	450
Bus Bar	AC Combiner Box - Venora/EMP	2
Wiring	DC Cables (6mm^2)	Multiple
	AC Cables	Multiple
	Grounding Cables	Multiple
Cable Trays	DC Cable Trays	Multiple
	AC Cable Trays	Multiple
Price includes	Design and Engineering Support for the Battery system	
	Installation	
	Additional Features as given	
	Testing and Commissioning	
	Transport and Labour	
	Traveling and Accommodation	

6.3 Component brand analysis

When designing the wind-solar hybrid energy system, a brand analysis is performed to determine the most efficient and cost-effective components.

Table 9: Brand analysis for the solar PV system

Description		**Supplier**	**Country of Origin**	**Applicable Warranty Period**
Panels (W)	475Wp Mono	Jinko/JA	China	12 Years - Product Warranty
Inverters (kW)	100kW	Huawei	China	5 Years
Mounting Structure	Structure and Accessories	Lanka Aluminum/ Swisstek	Sri Lanka	10 Years
LV Panel	Combiner Box	EMP/Venora	Sri Lanka	1 Year
Cables	DC Cables (6mm)	Phelps Dodge or Equivalent	Taiwan	1 Year
	AC Cables	Kelani / Sierra or Equivalent	Sri Lanka / India	1 Year
	Earth Cables		Sri Lanka / India	1 Year

Table 10: Brand analysis for the wind energy system

Description		**Supplier**	**Country of Origin**	**Applicable Warranty Period**
Generator	ASW HC 3.3kW	AWS	Australia	5 Years - Product Warranty
Fan Structure	Iron	Melwa	Sri Lanka	25 Years Warranty
Cables	DC Cables (6mm)	Phelps Dodge or Equivalent	Taiwan	1 Year
	AC Cables	Kelani / Sierra or Equivalent	Sri Lanka / India	1 Year
	Earth Cables		Sri Lanka / India	1 Year

Table 11: Brand analysis for the battery bank system

Description		**Supplier**	**Country of Origin**	**Applicable Warranty Period**
Batteries (Ah)	2100Ah,48V	Iron edition LFP	China	10 Years - Product Warranty
Mechanical Structure		Lanka Aluminum / Swisstek	Sri Lanka	10 Years
LV Panel	Combiner Box	EMP/Venora	Sri Lanka	1 Year
Cables	DC Cables (6mm)	Phelps Dodge or Equivalent	Taiwan	1 Year
	AC Cables	Kelani / Sierra or Equivalent	Sri Lanka / India	1 Year
	Earth Cables		Sri Lanka / India	1 Year

6.4 Net present value

An approach for calculating interest is called net present cost, or NPC. Various investment alternatives are adjusted to the year the initial investment cost was made using a specified interest rate. An investment is profitable if the NPC of the future payout exceeds the cost of the initial investment. If the optimization is done correctly, we can calculate the NPC using the HOMER software. The comparison of the NPC values can be seen in Figure 8.

6.5 Payback period

The payback method calculates how long takes to recover the initial investment cost from the invested money. Profitable investments are those where the repayment period is less than the estimated payback period. (SoFi, 2021)

Total price in the implementation of the solar system
= Rs. 117130320.00 (US$ 325362)
Total price in the implementation of the wind system
= Rs. 19029600.00 (US$ 52800)
Total price in the implementation of the battery system
= Rs. 36450000.00 (US$ 101250)
Total project implementation cost
= Rs. (117130320 + 19029600 + 36450000)
= Rs. 172609920.00 (US$ 479,472)
Daily Power generation = 1157kWh
Annual Power consumption = 1157kWh x 365
= 422305kWhYr
Buying Price offering for 1kWh by the government =Rs.34.00

ISSN 2961 - 5410 (Online) |

Return capital for one year = 422305kWhYr x Rs. 34
= Rs. 14358370.00 (US$ 39884.36)
Payback period = Total project implementation cost / Return capital for one year
= 172609920 / 14358370
= 12.022 Years

According to the payback method analysis, it takes 12 years to pay back the initial investment cost.

7 ENVIRONMENTAL IMPACTS

According to table 12, carbon emissions released by the 3 diesel generators are the highest. By designing the proposed wind-solar hybrid system, it uses a green approach to reduce carbon emissions. (Akyuz, 2012). The proposed renewable energy hybrid system is mainly environmentally beneficial, with no carbon emissions.

Table 12: Comparison of emissions between diesel generator power systems and wind-solar power systems

Description	**3 diesel generator-based power systems (100kVA,100kVA,250kVA)**	**Off-grid Wind Solar Hybrid System**
Pollutant	**Emissions (kg/yr)**	**Emissions (kg/yr)**
Carbon Dioxide	1417.284	0
Carbon Monoxide	3496.5	0
Unburned Hydrocarbons	387.45	0
Particulate Matter	263.7	0
Sulfur Dioxide	2844	0
Nitrogen Oxides	31216.5	0

8 CONCLUSION

Investigating whether it would be economically advantageous to build a solar and wind hybrid system on Analaitivu island was one of the objectives of this research. By contrasting the net present value (NPV) and system efficiency, optimization was carried out. Despite the system's economic advantages, the significant investment cost had to be considered as Sri Lanka is a lower-middle-income country, and the investment may not be financially viable for the typical household.

Sri Lanka must move its energy production as part of its efforts to reduce greenhouse gas emissions. In contrast to the energy mix acquired from the grid, solar and wind energy are both sustainable energy sources. A hybrid system is advantageous from a sustainable standpoint since it produces no net carbon emissions and helps the world achieve its sustainable development targets. Therefore, constructing a solar and wind hybrid system is advantageous from an economic and environmental standpoint, leading to a suitable optimization matching the objectives and limitations of the study.

REFERENCES

Akyuz, E. (2012). Researchgate.net. https://www.researchgate.net/publication/264441082_A_case_study_of_hybrid_wind-solar_power_system_for_reduction_of_CO2_emissions

AWS HC Wind Turbines. (n.d.). Aus Wind and Solar. Retrieved December 29, 2022, from https://www.australianwindandsolar.com/aws-wind-turbine-packages

ENF Ltd. (n.d.). ENF Ltd. Enfsolar.com. Retrieved December 29, 2022, from https://www.enfsolar.com/pv/panel-datasheet/crystalline/33723

Homer energy. (n.d.). Homerenergy.com. Retrieved December 29, 2022, from https://www.homerenergy.com/products/pro/docs/latest/storage.html

Portal, C. K. (n.d.). Sri Lanka. Worldbank.org. Retrieved December 29, 2022, from https://climateknowledgeportal.worldbank.org/country/sri-lanka/climate-data-historical

SoFi. (2021, June 25). payback period: Formula. SoFi. https://www.sofi.com/learn/content/how-to-calculate-the-payback-period/

Stackhouse, P. (n.d.). Nasa power. Nasa.gov. Retrieved December 29, 2022, from https://power.larc.nasa.gov/

Wikipedia contributors. (2020, December 10). Analaitivu. Wikipedia, The Free Encyclopedia. https://en.wikipedia.org/w/index.php?title=Analaitivu&oldid=993498547

ISSN 2961 - 5410 (Online) |

Machine Learning-Based Indoor Localization System with Human-Computer Interaction System

Anjana Jayasundara
Department of Electrical and Electronic Engineering, University of Curtin, Australia
Sri Lanka Institute of Information Technology, Sri Lanka
anjras2@gmail.com

Lakmini Malasinghe
Department of Electrical and Electronic Engineering, Sri Lanka Institute of Information Technology
New Kandy Road, Malabe, 10115, Sri Lanka
lakmini.m@sliit.lk

ABSTRACT

Understanding the indoor whereabouts of individuals and objects is important, especially for those who fall within the 71% of visually impaired individuals with a school education, students in 450 special education units and many other areas and aspects in Sri Lanka. Researchers have declared that, there isn't any particularly good localization system, and the performance should be evaluated considering the approach and application. The most well-known indoor positioning (IP) technologies that have been historically deployed are Bluetooth, Wi-Fi, RFID (radio frequency identification), IR (Infrared), and UV (ultraviolet) whereas received signal strength (RSSI), fingerprinting, and triangulation methods have been used as common IP techniques. The combination of both IP technologies and techniques creates an IP system, and the integration of machine learning and IoT with the structured system essentially delivers an accurate and more advanced system.

This paper contains a detailed, analytical review of a developed indoor positioning system derived from the existing indoor localization techniques, localization technologies, localization systems, algorithms, and performance matrixes. This also provides a comprehensive comparison between numerous existing systems to justify the proposed solution. This project has been developed to achieve better accuracy through low-cost deployment as an effective system to fill the gap in the scarcity of positioning systems in the world. This paper presents a descriptive introduction and problem definition, a critical discussion of results, machine learning models, benefits of the project, and future works. As later justified, ESP32 microcontroller and BLE beacons are utilized with RSSI fingerprinting method to develop this IP system and, as a part of the project, two data visualization methods have been introduced here using NodeRED dashboard and LC display. Overall, this project was developed with an effective combination of RSSI fingerprinting, IoT protocols, machine learning, and data interpretation methods.

KEYWORDS: *Indoor positioning, RSSI, Fingerprinting, Machine Learning, MQTT, ESP32, BLE beacons, NodeRED*

1 INTRODUCTION

Starting from the pre-hostoric times to the present modern era, localization was one of the key pieces of information that has been important according to past records. In the past, people used maps and compasses to find their way around outdoor environments. In the modern world, GLOBAL Navigation Satellite Systems (GNSS) such as Global positioning system (GPS) are considered a reliable technology for outdoor positioning. But with regard to indoor premises, GPS kind of technologies are highly unreliable as satellite signals are hindered by the presence of walls, roofs, and other stationary obstacles and here is where the importance of Indoor Localization Systems (ILS) is vital.

It is crucial to know someone's location in an indoor environment, especially when a person enters an unknown building. Unfamiliar indoor environments can often cause difficulties like getting lost, mostly for children, disabled people, and elderly individuals. This scenario mostly happens in

ISSN 2961 - 5410 (Online) | https://doi.org/10.54389/WPDK5680

indoor places such as hospitals, libraries, conference centers, shopping malls, and underground stations. This can result in various challenging situations starting from delaying daily tasks to prolonging immediate medical attention or the life and death situations in an emergency. In terms of industrial usability, warehouse managers and store managers regularly need to locate certain goods to prepare for transport. It can be complicated in large warehouses as they can be crowded, many transactions taking place, and the initial positions of the previously stored goods can be changed intentionally or unintentionally when managing the space. In such a context, the question is whether it is possible to track the position of those objects without extensive human involvement? The answer to all these problems is an indoor positioning system that can localize any user or object within a certain indoor environment and provide the location details for a responsible third party and to the user. Other than that, numerous applications require IPS techniques such as for military purposes, healthcare, biomedical, agriculture, industrial applications, etc. Indoor localization is important when it comes to rescuing missions of children or disabled persons and even for objects so that rescuers could directly approach them without any delay.

There are several objectives to be fulfilled by the completion of this project. Firstly, it intends to demonstrate the redundancy of explicit computation of other IP methods such as triangulation by highlighting the easy deployment of every technology and technique used in this project. Secondly, it introduces NodeRED for IPSs. Thirdly, it also introduces an effective alternative for mobile phone based IPSs. Most importantly this project encourages/promotes low-energy devices such as BLE beacons and ESP32 for the IPSs and advocates promising technologies and protocols such as IoT and machine learning.

The performance and novelty of an IPS can be assessed using simple performance metrics. The areas specified there can be listed as accuracy, responsiveness, coverage, adaptiveness, scalability, cost, and complexity, and the energy consumption, latency, precision, and robustness (*How accurate are indoor positioning systems? - Senion | Smart Office Solution*, n.d.; Pascacio et al., 2021). Therefore, the suggested approach will present a highly accurate IPS with high responsiveness, low cost and also an easily deployable, energy saving, robust system compared to the existing systems. This will be a novelty as there is no record of successfully implemented IPS in the local context. In Sri Lanka, there are 1.42 million visually impaired or blind people which intensifies the importance of low-cost, precise IPS within the local context. Students are not allowed to bring smartphones to school hence no mobile-based IPS in Sri Lankan schools. Consequently, in the case of an emergency within school premises, it can be challenging to proceed with evacuation, especially for students with disabilities and vision imparities. In that case, those students need an alternative to a phone based IPS and this suggested novel IPS can cater to that requirement without violating school policies. Since this is not a phone-based application any elderly or children who do not have the literacy to use a mobile phone will also benefited. As a novel feature, this project introduces the NodeRED dashboard to IPS that provides the ability for any authorized external party to access the user location.

2 LITERATURE REVIEW

2.1 IPS based on localization technologies

Based on better coverage and user experience, indoor localization technologies can be varied such as WIFI, radio beacons, or RFID (Obreja et al., 2020a). Among all of them, Bluetooth low-energy (BLE) beacons are the best option due to their better accuracy and lower energy consumption. Bluetooth IDs can be used to locate the Bluetooth tags, similar to, each BLE beacon established in a certain indoor environment. Due to the characteristic procedure of detecting the position, Bluetooth-based IPS can have a minor latency and some extra power consumption which has been contained in the BLE (Farid et al., 2013), (*BLE Advertising Primer | Argenox*, n.d.) with the additional benefits of being inexpensive, smaller in size and running on battery power for a longer period. BLE protocols reduce battery consumption when sending advertisement messages or data messages with short duration through the distinctive communication established via each 2MHz ranged 40 channels (Faragher et al., 2015a). Moreover, BLE can be integrated with various positioning techniques following RSSI, fingerprinting, and triangulation.

ISSN 2961 - 5410 (Online) |

Wi-Fi-based IP systems have become very popular due to their integrated availability and accessibility through many mobile devices and their capability of running localization with adequate accuracy (Faragher et al., 2015a). As same as Bluetooth or BLE, fingerprinting techniques can be integrated with Wi-Fi technology for improved localization accuracy. As for some disadvantages, time consumption for SSID scanning, fluctuations in signal strength over time and the appearance of tangible objects, and signal interferences with intertwining frequencies such as 2.4 GHz can be confronted (Farid et al., 2013).

Radio-frequency identification, also known as RFID, can be identified as another sophisticated technology in facilitating the prospect of indoor localization. RFID's capability of catering to the requirements of different applications is relatively high and typically used in people or object detection, automobile assembly, supply chain, and warehouse management.

2.2 IPS based on localization techniques - RSSI fingerprinting

Received Signal Strength Indicator (RSSI) is the key information that is being widely used in the positioning domain which is used to calculate or determine the distance between receiving end and the transmitting end using Radio frequency (RF) signals(Chatzimichail et al., 2021). As a major drawback, RSSI information can fluctuate due to the influence of multipath, reflection and the gain of the antenna used which leads it to an error-prone behavior when it is functioning individually. To eliminate this, fingerprinting can be utilized as a fusion with RSSI.

The fingerprinting approach creates an offline location database with respect to the RSSI measurements collected from the BLE or Access point by separating the particular indoor environment into grids. In the online phase, real-time RSSI measurements gathered will be compared with the offline fingerprinting database to predict the position of the receiver. In this positioning, it is neither necessary to know the position of Wifi or BLE beacons nor to transfer the RSSI measurements faraway in order to avoid environmental hindrances (Chatzimichail et al., 2021; A. Zhang et al., 2015). Then the machine learning models such as KNN, Support Vector Machine (SVM), and Deep Neural Networks (DNN) can be deployed to calculate the position through the closest distance between offline and online points(Hu et al., 2019; Soro et al., 2019; S. Zhang et al., 2019). This RSSI-based fingerprinting method has been used by (Obreja et al., 2020b), (Faragher et al., 2015b), (Chatzimichail et al., 2021), (A. Zhang et al., 2015) with various approaches and algorithms which will be discussed in the next section of the literature review. Nevertheless, some issues can occur in self-positioning, granularity, reliability, and accuracy which are comparatively considered as minor issues in RSSI fingerprinting (Prasithsangaree et al., 2002). (Bahl et al., 2000; *Enhancements to the RADAR User Location and Tracking System*, n.d.; Smailagic et al., 2002; Youssef, 2002) addresses some issues in the accuracy of fingerprinting method with regard to the database size, robustness, and hardware deployment. RSSI-based triangulation methods are significantly complex and hence will not be discussed in this paper.

2.3 Indoor localization systems

2.3.1 IPS based on bluetooth/BLE RSSI fingerprinting

Because of the above-mentioned advantages, BLE based RSSI fingerprinting method for Indoor Positioning Systems have become more widespread across the globe. Short-duration advertisement messages are important not only for favorable power consumption and also for the fact that advertisements are necessary to establish any type of communication irrespective of the application. Motivating Bluetooth low energy over Wi-Fi for fingerprinting-based localization is due to the multiple reasons engaged with the typical characteristics of data transaction in BLE and Wi-Fi.

Although both Wi-Fi and BLE dominate in the same RF (Radio Frequency) bands, there are some trivial but technically crucial differences which lead to substantial effects on overall performance of the application (Farid et al., 2013)

- Wi-Fi takes a few seconds to scan the SSID (Service Set Identifier) and delays due to the buffering which leads to a lower localization update rate. It can also cause confusion in fingerprinting especially when the user is moving.
- Increased network traffic because of the Wi-Fi active scan and reduced Wi-Fi throughput.

- Second-party Wi-Fi fingerprinting will be restricted in some mobile platforms.

BLE fingerprinting with beacons that have high transmission and advertising frequency such as 50Hz have been utilized for improved localization. In this instance, testing was done using an iPhone and map construction was done using the data set gathered at the experiment. Most importantly (Faragher et al., 2015a) is emphasizing the criticality of considering the particular algorithm to use for fingerprinting, and the interdependent parameters that come with the BLE beacons such as beacon density, orientation, power transmission, mobility, and geometry.

In (Jain et al., 2021), proposed RSSI-based fingerprinting and an improved fingerprinting data augmentation technique as a novel approach to the IPSs which have a lesser number of anchor nodes. Fingerprinting data augmentation technique is utilized to produce an augmented result based on the RSS values gathered at each grid point. On the other hand, Obreja and vulpe have developed an RSSI fingerprinting localization system with the minimum number of beacons, as in only 6 beacons over 110 m^2, adopting the K-NN algorithm. Data collection was done by Samsung Galaxy S6 and a Samsung Galaxy A6 plus phones and Euclidean distance was calculated by employing 130 RSSI vectors that have been gathered at the test phase. (Obreja et al., 2020a)

2.3.2 IPS based on Wi-Fi-based RSSI fingerprinting

Due to the extensive availability and easy access, Wifi can be considered an ideal nominee for localization, and it is basically the most popular technique worldwide. An ample amount of research has been done in this context and can find some of them in (S. Zhang et al., 2019), (Chabbar et al., 2017), (Jiang et al., 2012; Salamah et al., 2016), (Xue et al., 2020).

The typical IPS using Wifi-based RSSI fingerprinting was developed in (Chabbar et al., 2017) and 21.97 m by 10.84 m experimental testbed with 3 wifi access points. Fingerprinting was done here by collecting fingerprints for 1 minute in all directions over an area of 1 square meter around the reference point and capturing the RSSI fingerprint for every reference point. Then the database was generated by storing the average of the fingerprints using clustering techniques. Yifei Jiang et al. have introduced ARIEL, a fully automatic localization system based on room fingerprinting. This system is mobile phone-based and capable of recognizing the rooms easily. This approach recorded a very satisfying accuracy of 95% with a lesser number of clusters.

3 METHODOLOGY

Considering all the technologies and techniques, and their advantages and disadvantages, how well they are contributing to the performance matrix of the IPS, the final specifications for the suggested system are determined. Subsequent to careful comparison among technologies and techniques bellow specifications were filtered out.

- BLE > Bluetooth > Wi-Fi > Zigbee, UWB, Infrared
- RSSI+Fingerprinting > Triangulation >Trilateration

3.1 MQTT as a communication protocol

The problem with HTTP as the protocol of data transferring is that it adds a large number of small data blocks as nonapplication data, overheading the protocol. As a solution, MQ Telemetry Transport (MQTT) is introduced as a highly efficient communication protocol of an IoT-based application which also minimizes the overhead. This also reduces the complexity and traffic flow of the network that HTTP has, due to the address-based routing by replacing it with a name-based routing. Apart from that, MQTT has lower latency, Law bandwidth usage, and lightweight, and high throughput which makes it the better candidate for an IPS. The diagram below shows how the data transfer happens in an MQTT protocol.

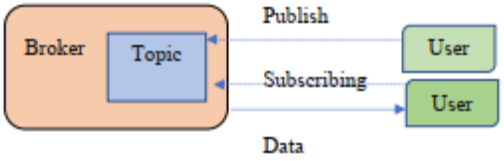

Figure 1: MQTT mechanism

ISSN 2961 - 5410 (Online) |

3.2 Data interpretation through NodeRED

A publicly accessible common dashboard to visualize the user location was developed. For data visualization, it was suggested to use the NodeRED platform which has advanced tools and capabilities to work with servers and MQTT protocol. NodeRed is an open-source flow-based visual programming tool as shown below in figure 2 which has the capability to wire hardware devices, online services and Apps together. Most importantly, NodeRed is capable of creating attractive and informative interfaces for IoT-based applications.

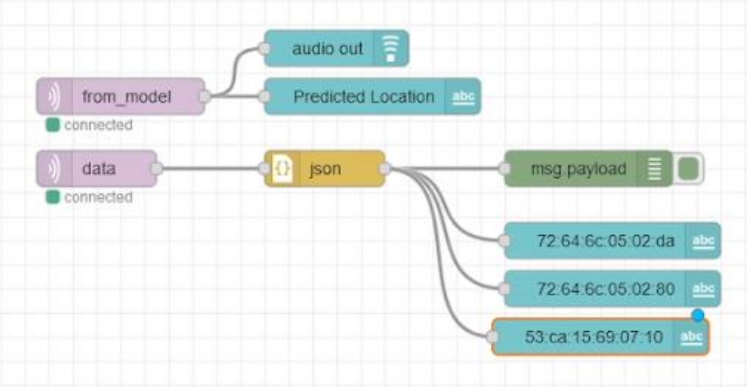

Figure 2: NodeRED flow for result visualization

3.3 Project Implementation

ESP 32 device is used as the BLE beacon receiver and data transmitting device in this project. As shown in figure 3, data collection for the location estimation is done by using an ESP32 device which is a general-purpose development board with integrated WIFI and BLE capabilities. ESP 32 would act as the MQTT client mentioned above, in order to collect and publish the data. It is also responsible for acting as the BLE scanner and gathering the RSSI values from the beacons.

During the data-acquiring phase, which is the offline phase of the fingerprinting method, the received signals will be collected by the ESP 32 and transmitted to the MQTT server. To do that, ESP 32 consists of inbuilt WIFI capability, and the device will push the data, which is formatted in JSON format, periodically to the MQTT broker through WIFI by connecting to a WIFI hotspot. In technical terms, ESP 32 acts as a client and publishes the data to an MQTT topic in an MQTT broker, simultaneously using the personal computer as another client, the published data can be saved in a local machine by subscribing to the same MQTT topic where ESP 32 published the data. In order to generate a sizable dataset this process needed to be continued for a sufficient period. Locally saved generated data then can be pre-processed before training them by analyzing the values, columns, etc. Then removing the anomalies depending on the functionality of BLE beacons and by looking at the dataset. Next, the data set is ready to train by algorithms and different models such as K-Nearest Neighbors, SVM, Random Forest, and CATBoost classifier. Based on the results, each algorithm will be assessed according to a performance matrix considering the accuracy of each model and the time taken to predict. The properly generated output will then be compared with the real-time dataset of the online phase of the fingerprinting approach. Machine learning scripts can be run on a cloud if it is feasible to get access to a cloud platform for a better training experience. If not, it is also possible to run it on local machines. Finally, the results will be displayed as mentioned in the data interpretation part above.

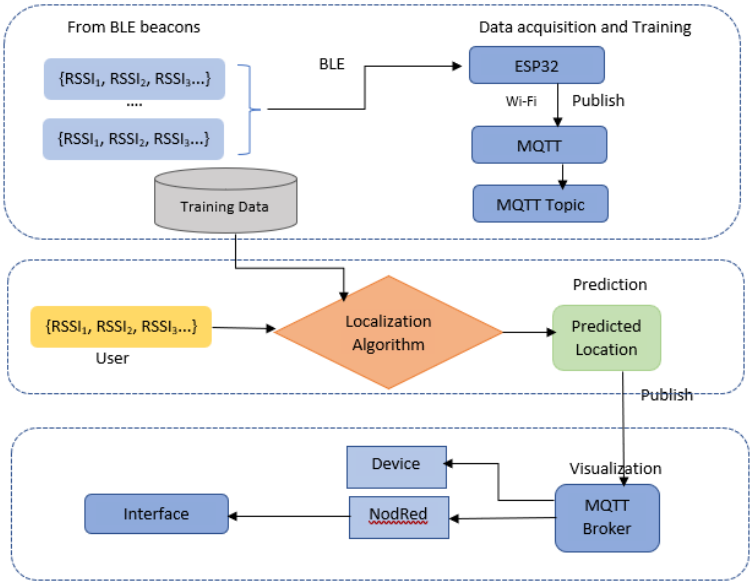

Figure 3: Project Architecture

4 RESULTS AND DISCUSSION

After the offline phase is done and all the gathered data has been trained, the online phase starts. During the online phase, the user with the ESP32 device will go to each room that was used to gather the data from. Ideally, all the predictions received from the final ML model for each room should be the same as the actual room IDs. The same room ID should be displayed on the LCD display connected with the second ESP32 and the NodeRED dashboard.

4.1 Results for 2 BLE beacons and 1 mobile phone-based beacon

While keeping the two BLE beacons fixed, a phone-based beacon was configured every 15 minutes and continued to get data. Once the data is saved in the offline phase, the CSV file should be updated with the new BLE address of the utilized mobile phones. A mobile application called “Beacon Simulator” was used for this task to identify the changes in BLE addresses of mobile phones.

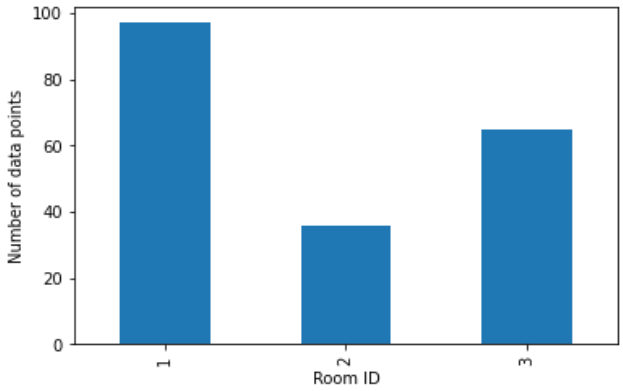

Figure 4: Distribution of gathered

Typically, the mean of data instances should be equal. But due to connection problems, different time intervals of collecting data, and after removing some anomalies, some data must be removed. Due to that reason, a lesser number of data instances was remained for room 2.
Then the model will be trained from the training dataset and the accuracy of predictions will be taken from the test dataset.

ISSN 2961 - 5410 (Online) |

Accuracy, precision, recall, and F1 scores of each model were calculated for Random Forest, KNN, SVM linear, SVM rbf, and CAT booster. Machine learning (ML) models were selected after studying the literature review and considering the amount of data to handle. As identified, KNN and SVM are the simplest algorithms to be used but they reportedly have comparatively poor performance. But since the application is simple and has historically been used in such IPSs it was decided to use this IPS too.

As the random forest is considered to be a model with high accuracy and the ability of multi-dimensional data handling, it was considered to be an appropriate choice for the application. Although the mechanism is relatively complex, random forests are less likely to get overfitted than the other high-level algorithms. CATboost classifier has the same advantages as the random forest but it is more prone to be overfitted than the random forest. The suggested application with a specific amount of data will be insufficient for an algorithm like neural networks. So even though the model is efficient, it is highly likely to get overfit especially when the dataset is too small. The results of deployed supervised classification models are as follows.

In machine learning, accuracy gives an idea about the number of times that the model provided correct predictions whereas precision refers to how well the model performs to predict a specific category of data. Accuracy and precision are both equally important factors as precision demonstrates the consistency of the accuracy. Recall is the ability to identify all data in one class of the classification model. The F1 score is a combined result of both precision and recall so it would make the decision-making process much easier based on the received results.

	Model	Accuracy	Precision	Recall	F1 Score
0	Random Forest	1.0	1.000000	1.0	1.000000
1	CATBoost	1.0	1.000000	1.0	1.000000
2	KNN	0.9	0.925000	0.9	0.902256
3	SVM-Linear	0.9	0.907143	0.9	0.900607
4	SVM-Rbf	0.9	0.925000	0.9	0.902256

Figure 5: Results from ML algorithms

As can be seen in the figure, random forest and CATboost give the highest accuracy, precision, and F1 score which make those the best models for the application. Since all the testing factors give the same positive result for both random forest and CATboss there should be another way to choose the best model out of these two. Accordingly, the time taken to train the model and inference time was calculated. Inference time is basically the time taken to make predictions. The tabulated results for all the models are as follows.

	Model	Time taken for training(s)	Inferencing time for sample(us)
0	Random Forest	0.117279	427.055359
1	CATBoost	0.539056	64.957142
2	KNN	0.002096	108.122826
3	SVM-Linear	0.068508	15.866756
4	SVM-Rbf	0.002878	68.938732

Figure 6: Training and inferencing time

So, it is obvious that the random forest takes the least time to train the model among the highest accuracy models. But in terms of inferencing time, the CATboost model shows more potential to be the best candidate for the final model. When predicting locations, the most important factor is real-time performance. Therefore, the final model should essentially be the model with the highest accuracy and lowest inferencing time. But as discussed above, above, CATboost classifier can easily be overfitted

with a small number of data entries. Subsequently, it was decided to use random forest classifier as the final machine learning model to deploy in this IPS after considering all the factors.
The reliability of the selected classifier random forest can be further assessed by generating the classification report. The classification report provides a brief summary of accuracy, precision, recall, and f1-score in terms of class or room. That can be used to gauge how well the model has performed in each class.

**********Classification Report of Highest Acc. Model*********

	precision	recall	f1-score	support
1	1.00	1.00	1.00	10
2	1.00	1.00	1.00	4
3	1.00	1.00	1.00	6
accuracy			1.00	20
macro avg	1.00	1.00	1.00	20
weighted avg	1.00	1.00	1.00	20

Figure 7: Classification Report

Precision 1.0 means no false positives predicted for any room and recall 1.0 means no false negative predicted for any room. An F1 score of 1.0 gives the idea that a model has an ideal performance while the Macro avg is the Average of the precision, recall, and F1 between rooms or classes. Accordingly, it is evident that the random forest classifier is the best model for the suggested system.

If one carefully evaluates the received accuracies which are nearly ideal, considering the amount of data collected, it is natural to question whether the models are overfitted. To verify this,a simple algorithm called k-fold cross-validation can be carried out to check if the model is overfitted or underfitted. K folds cross-validation splits the dataset into k subsets and trains it k times on various training sets and gets the predictions for k times to the different test sets (*How to Check if a Classification Model is Overfitted using scikit-learn | by Angelica Lo Duca | Towards Data Science*, n.d.). At that point, it offers a graph with the number of folds against the mean absolute error and if the difference between train and test sets is larger, it is overfitted.

Therefore, in order to ensure the model is properly trained, k folds cross-validation is done for both random forest classifiers. The received graph is as follows. As it is properly manifested in the figure given below, the difference between the train and test is only around 0.01. Accordingly, it can be considered that the model is not overfitted although it provides 100% accuracy. Thus, it can be assumed that the reason for getting higher accuracies is the scarcity of data entries.

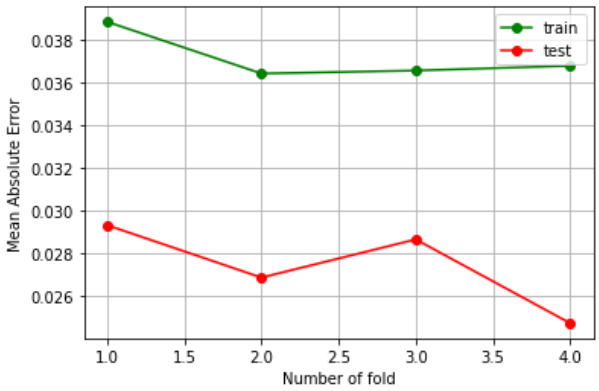

Figure 8: K fold cross validation for random forest classifier

For testing purposes, the 4 BLE beacons were also tried to evaluate the difference between accuracies. For that 2 BLE beacons with 2 mobile phones-based, BLE beacons were utilized.

ISSN 2961 - 5410 (Online) |

Nevertheless, as previously mentioned, only the offline phase and model training phase was carried out due to the extreme complications of mobile phone BLE beacons. The results of the trained models are attached below.

4.2 Results for 2 BLE beacons and 2 mobile phone-based beacon

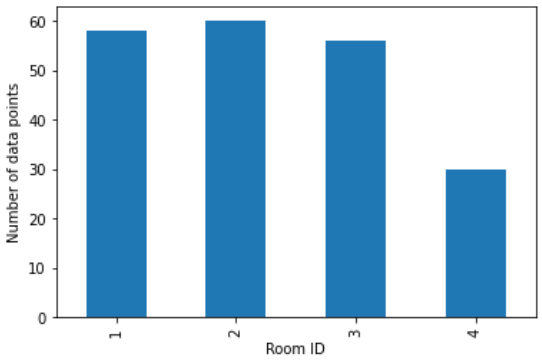

Figure 9: Gathered data from 4 BLE beacons

Due to the same reasons mentioned above, room 4 has a lesser number of data while the other 3 rooms have an approximately equal number of data entries.

	Model	Accuracy	Precision	Recall	F1 Score
0	Random Forest	0.952381	0.959184	0.952381	0.952048
1	CATBoost	0.952381	0.959184	0.952381	0.952048
2	KNN	0.761905	0.769048	0.761905	0.761905
3	SVM-Linear	0.904762	0.904762	0.904762	0.904762
4	SVM-Rbf	0.666667	0.692857	0.666667	0.671284

Figure 10: Results from ML algorithms

As it can be seen, the accuracies, precisions, recall, and f1 scores have different value sets than in the previous case. However, the random forest and CATboost classifiers have better accuracy than the other models. As shown in figure 11 below. Random forest is reportedly taking less time to train the model and inferencing time is almost the same in both models. Therefore, the random forest classifier can be considered the superior algorithm for this application.

	Model	Time taken for training(s)	Inferencing time for sample(us)
0	Random Forest	0.165611	583.239964
1	CATBoost	0.741564	511.498678
2	KNN	0.002351	170.594170
3	SVM-Linear	0.009870	29.404958
4	SVM-Rbf	0.003033	32.561166

Figure 11: Training and inferencing time

Due to those differences, classification reports also calculate diverse value sets for accuracy, precision, and recall. Same as before, to ensure the reliability of the model, k folds cross-validation was carried out and the results were as follows in figure 12.

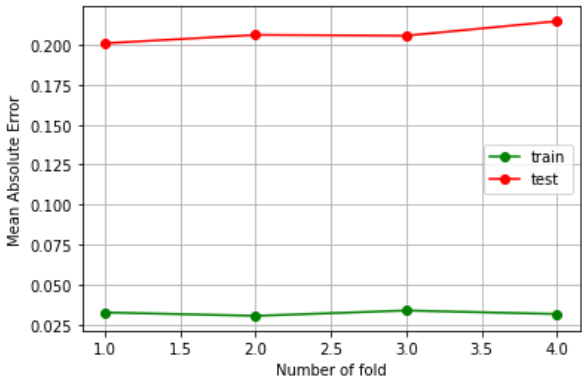

Figure 12: K fold cross validation for random forest

The difference between the train and test set is comparatively larger having nearly a 0.17 difference. This can be taken as a characteristic of overfitting the data. Consequently, it can be determined that the models are doing predictions with more accuracy because of the overfitting effect. The reason for overfitting here can be the smaller number of data instances, anomalies that occurred at the data gathering phase, and the high complexity of the model for the application. Overfitted models can result in wrong predictions for new datasets and failure in fitting the additional data.

4.3 Nodered results

The final NodeRED UI dashboard shows in the following figure 13.

Figure 13: NodeRED Dashboard

Additionally, the narrating option has been added to the dashboard so the predicted room number will be audible and visible at the same time.

4.4 Handheld device result

The final implementation of the prototype of the handheld device is in figure 14 below.

Figure 14: Result visualization on the handheld device

5 CONCLUSION

As expected, the supposed results were obtained with higher accuracy. Random forest classifier was identified as the best machine learning model for the suggested project considering the numerous factors that were proved and justified above. The performance matrix will be fully satisfied from this proposed project which can bring many benefits to the customers.

The quality of an IPS depends on the accuracy of the system which is the most mandatory requirement of any system. This proposed system has demonstrated high accuracy which is 100% for small-scale datasets. Even the KNN and SVM classifiers achieved 90% accuracies which guarantees the sufficient accuracy of the proposed system. Coverage and responsiveness correspondingly define the boundary that an IPS is capable of functioning and the time is taken to update the position of the user when the user is on the move. As documented before, the inference time of the final algorithm was in the microsecond range which emphasized the high responsiveness of the system. Regardless of the external hindrances that might affect the IPS, it managed to give an accurate localization with lesser calibrations which is called adaptiveness. This system is highly adaptive due to the proper utilization of machine learning models. Higher the archived level of aforementioned factors, the higher the quality of the system is. Power consumption is significantly reduced from this system by using the Bluetooth low energy beacons with ESP32 device. Apart from the cost of the infrastructure and technical support, the complexity of the algorithm, and scalability of the system are also thoroughly examined and satisfied by this particular approach which creates the novelty of this solution other than the technology stack used to develop this IPS.

The results obtained from the test runs carried out could be improved by utilizing only the proper BLE beacons rather than mobile phones. Using mobile phones as BLE beacons is considerably challenging as explained before and prone to add more anomalies to the dataset. Therefore, eliminating alternative hardware and adhering to the ideal hardware will result in a quality dataset and improved accuracy on the larger scale of this system. Employing deep learning techniques to pre-process the large dataset and remove anomalies will also generate a perfect dataset with enhanced accuracy. Further, the filters like Kaliman filter can be used to finetune the output of the system. New BLE beacons with an equal degree of battery and ESP32 devices with similar time intervals will also be helpful to improve the proposed system.

This localization system has the possibility to extend, to cater to the indoor navigation facility. Subsequently, this IPS can be updated to indoor localization and navigation system which can accommodate another crucial aspect of the location-based system. It will not be necessary to change the infrastructure and hardware in the process of updating this IPS, because all the components that have been used in this system can be directly used for an indoor navigation system as well.

As mentioned above, this system can be updated and tested with deep learning and filtering mechanisms and has the potential to be embedded into an indoor navigation system to further update the approach. Additionally, if a narrating option could be included in the handheld device, that will be useful to vision impaired individuals.

REFERENCES

Bahl, P., & Padmanabhan, V. N. (2000). RADAR: An in-building RF-based user location and tracking system. *Proceedings - IEEE INFOCOM*, *2*, 775–784. doi: 10.1109/INFCOM.2000.832252*BLE Advertising Primer | Argenox*. (n.d.). Retrieved from https://www.argenox.com/library/bluetooth-low-energy/ble-advertising-primer/

Chabbar, H., & Chami, M. (2017). Indoor localization using Wi-Fi method based on Fingerprinting Technique. *2017 International Conference on Wireless Technologies, Embedded and Intelligent Systems, WITS 2017*. doi: 10.1109/WITS.2017.7934613

Chatzimichail, A., Tsanousa, A., Meditskos, G., Vrochidis, S., & Kompatsiaris, I. (2021). RSSI Fingerprinting Techniques for Indoor Localization Datasets. *Advances in Intelligent Systems and Computing*, *1192 AISC*, 468–479. doi: 10.1007/978-3-030-49932-7_45

Enhancements to the RADAR User Location and Tracking System. (n.d.). Retrieved from https://www.researchgate.net/publication/2645073_Enhancements_to_the_RADAR_User_Location_and_Tracking_System

Faragher, R., & Harle, R. (2015a). Location fingerprinting with bluetooth low energy beacons. *IEEE Journal on Selected Areas in Communications*, *33*(11), 2418–2428. doi: 10.1109/JSAC.2015.2430281

Faragher, R., & Harle, R. (2015b). Location fingerprinting with bluetooth low energy beacons. *IEEE Journal on Selected Areas in Communications*, *33*(11), 2418–2428. doi: 10.1109/JSAC.2015.2430281

Farid, Z., Nordin, R., & Ismail, M. (2013). Recent advances in wireless indoor localization techniques and system. *Journal of Computer Networks and Communications*, *2013*. doi: 10.1155/2013/185138

How accurate are indoor positioning systems? - Senion | Smart Office Solution. (n.d.). Retrieved from https://senion.com/insights/accurate-indoor-positioning-systems/#:~:text=A%20common%20solution%20to%20improve,last%20couple%20of%20position%20updates.

How to Check if a Classification Model is Overfitted using scikit-learn | by Angelica Lo Duca | Towards Data Science. (n.d.). Retrieved from https://towardsdatascience.com/how-to-check-if-a-classification-model-is-overfitted-using-scikit-learn-148b6b19af8b

Hu, J., Liu, D., Yan, Z., & Liu, H. (2019). Experimental Analysis on Weight K-Nearest Neighbor Indoor Fingerprint Positioning. *IEEE Internet of Things Journal*, *6*(1), 891–897. doi: 10.1109/JIOT.2018.2864607

Jain, C., Sashank, G. V. S., Venkateswaran, N., & Markkandan, S. (2021). Low-cost BLE based Indoor Localization using RSSI Fingerprinting and Machine Learning. *2021 International Conference on Wireless Communications, Signal Processing and Networking, WiSPNET 2021*, 363–367. doi: 10.1109/WISPNET51692.2021.9419388

Jiang, Y., Pan, X., Li, K., Lv, Q., Dick, R. P., Hannigan, M., & Shang, L. (2012). *ARIEL: Automatic Wi-Fi based Room Fingerprinting for Indoor Localization*.

Obreja, S. G., & Vulpe, A. (2020a). Evaluation of an Indoor Localization Solution Based on Bluetooth Low Energy Beacons. *2020 13th International Conference on Communications, COMM 2020 - Proceedings*, 227–231. doi: 10.1109/COMM48946.2020.9141987

Obreja, S. G., & Vulpe, A. (2020b). Evaluation of an Indoor Localization Solution Based on Bluetooth Low Energy Beacons. *2020 13th International Conference on Communications, COMM 2020 - Proceedings*, 227–231. doi: 10.1109/COMM48946.2020.9141987

Pascacio, P., Casteleyn, S., Torres-Sospedra, J., Lohan, E. S., & Nurmi, J. (2021). *Collaborative Indoor Positioning Systems: A Systematic Review*. doi: 10.3390/s21031002

Prasithsangaree, P., Krishnamurthy, P., & Chrysanthis, P. K. (2002). On indoor position location with wireless lans. *IEEE International Symposium on Personal, Indoor and Mobile Radio Communications, PIMRC*, *2*, 720–724. doi: 10.1109/PIMRC.2002.1047316

Salamah, A. H., Tamazin, M., Sharkas, M. A., & Khedr, M. (2016). An enhanced WiFi indoor localization System based on machine learning. *2016 International Conference on Indoor Positioning and Indoor Navigation, IPIN 2016*. doi: 10.1109/IPIN.2016.7743586

Smailagic, A., & Kogan, D. (2002). Location sensing and privacy in a context-aware computing environment. *IEEE Wireless Communications*, *9*(5), 10–17. doi: 10.1109/MWC.2002.1043849

Soro, B., & Lee, C. (2019). Performance Comparison of Indoor Fingerprinting Techniques Based on Artificial Neural Network. *IEEE Region 10 Annual International Conference, Proceedings/TENCON*, *2018-October*, 56–61. doi: 10.1109/TENCON.2018.8650230

Xue, J., Liu, J., Sheng, M., Shi, Y., & Li, J. (2020). A WiFi fingerprint based high-adaptability indoor localization via machine learning. *China Communications*, *17*(7), 247–259. doi: 10.23919/J.CC.2020.07.018

Youssef. (2002). *AAProbabilisticcClustering-BaseddIndoorrLocationnDeterminationnSystemm*.

Zhang, A., Yuan, Y., Wu, Q., Zhu, S., & Deng, J. (2015). Wireless Localization Based on RSSI Fingerprint Feature Vector: *Http://Dx.Doi.Org/10.1155/2015/528747*, *2015*. doi: 10.1155/2015/528747

Zhang, S., Guo, J., Luo, N., Wang, L., Wang, W., & Wen, K. (2019). Improving Wi-Fi Fingerprint Positioning with a Pose Recognition-Assisted SVM Algorithm. *Remote Sensing 2019, Vol. 11, Page 652*, *11*(6), 652. doi: 10.3390/RS11060652

ISSN 2961 - 5410 (Online) |

Comparative Lifecycle Analysis of Sri Lankan Non-Conventional Roofing Materials

W. A. Nipun Fernando
Department of Civil Engineering, Sri Lanka Institute of Information Technology
New Kandy Road, Malabe, 10115, Sri Lanka
akilanipun1998@gmail.com

Shiromi Karunaratne
Department of Civil Engineering, Sri Lanka Institute of Information Technology
New Kandy Road, Malabe, 10115, Sri Lanka
shiromi.k@sliit.lk

ABSTRACT

Building materials, especially roofing products, play a major role as they are essential for any building construction. Knowledge of the environmental performance of building materials is vital when building life cycle assessment. However, only a few studies have been conducted in Sri Lanka in this regard. The present study focuses on the environmental life cycle assessment of two different non-conventional roofing materials used in Sri Lanka. Acrylonitrile Styrene Acrylate roofing sheets and Calicut-type clay roofing tiles have been selected for the study. In order to measure and calculate environmental impacts of both types of roofing materials, field data was collected quantitatively and noted as per ISO14040 and ISO14044. Using the Cradle-to-Gate LCA technique and OpenLCA software, the environmental impacts as midpoint and endpoint categories were evaluated. As the main output of the study, environmental performance of these two roofing materials were compared, the hotspots of the manufacturing process and the causes were also identified. . Accordingly, the global warming potential of Acrylonitrile Styrene Acrylate roofing sheets and Calicut-type clay roofing tiles is 13.5 kgs of CO_2 eq. and 8.95 kgs of CO_2 eq. respectively. Further, comparison of the endpoint categories showed the resource depletion was most impactful, indicating 0.814012 points and0.65305 points, respectively for the two roofing material types. Further, kiln firing was identified as the environmental hotspot contributing most to the endpoint and midpoint impact categories for clay roofing tiles, while mixing materials by hot mixer was the hotspot for Acrylonitrile Styrene Acrylate roofing sheets. In addition, the overall results demonstrated how the production process of clay tile influences more than the Acrylonitrile Styrene Acrylate roofing sheet on both the midpoint as well as the endpoint impact categories.

KEYWORDS: *Acrylonitrile Styrene Acrylate, Calicut tiles, Cradle-to-Gate, End-pint impacts, Mid-point impacts*

1 INTRODUCTION

Many resources are used for construction activities worldwide. It is evident that there are environmental impacts associated with each stage of construction. Among the building materials, roofing materials play a major role as they are used in all types of building projects. From the point of extraction of raw materials till manufacturing, roofing materials have different environmental impacts. Further, environmental performance data plays a vital role in building life cycle assessment as well. In order to understand the environmental performance of building materials, it is important to analyze their life cycle through a standard LCA methodology. This will allow the hotspot identification through the production process to reduce the environmental impacts.

According to previous studies carried out locally [1,2], there are only a few LCA based research carried out on roofing materials. Clay rooftiles, Asbestos roofing sheets were considered for LCA locally and Carlisle Sure-Flex PVC Membranes [3], White SPPR PVC roofing membranes [4] were some of the internationally considered roofing materials for LCA. Moreover, cradle-to-grave LCA

ISSN 2961 - 5410 (Online) | https://doi.org/10.54389/BJBJ5248

Analyses covering the entire lifecycle of roofing materials are rare. Therefore, the objective of the present study is to conduct a process based LCA analysis for the most popular non-conventional roofing materials in Sri Lanka to identify the environmental/hotspots and compare the different manufacturing processes.

2 MATERIALS AND METHODOLOGY

2.1 Selection of roofing materials

The selection of roofing materials was done based on two criterion: the most used and the preferred roofing materials in Sri Lanka.

2.1.1 Selection criteria 01

The first selection criteria for roofing material selection focused on the usage of roofing materials in Sri Lanka. Table 1 shows the number of housing units in Sri Lanka with different roofing materials (Department of Census and Statics of the population and housing stock). According to Table 1 the most used roofing material type for house construction is clay roofing tiles [5].

Table 1: Roofing materials used in housing units (Department of Census and Statics data)

Roofing material	**Number of housing units**
Clay tiles	2,479,226
Asbestos	1,800,07
Concrete	213,587
Zink Aluminum sheet	49,433
Metal sheet	544,211
Cadjan/ Palmyrah/ Straw	109,62
Other	11,583

2.1.2 Selection criteria 02

As the second selection criterion for roofing material for the study, the preference for roofing material for house construction of individuals was assessed. An online survey was carried out using over 190 Google forms. The survey had 03 multiple choice questions, assessing the provinces of the participants, the roofing material they prefer, email, and the name of the participants. For the validation of the responses, the email of each participant was required and only one response from a single email was considered. Below are the results obtained from the online survey.

ISSN 2961 - 5410 (Online) |

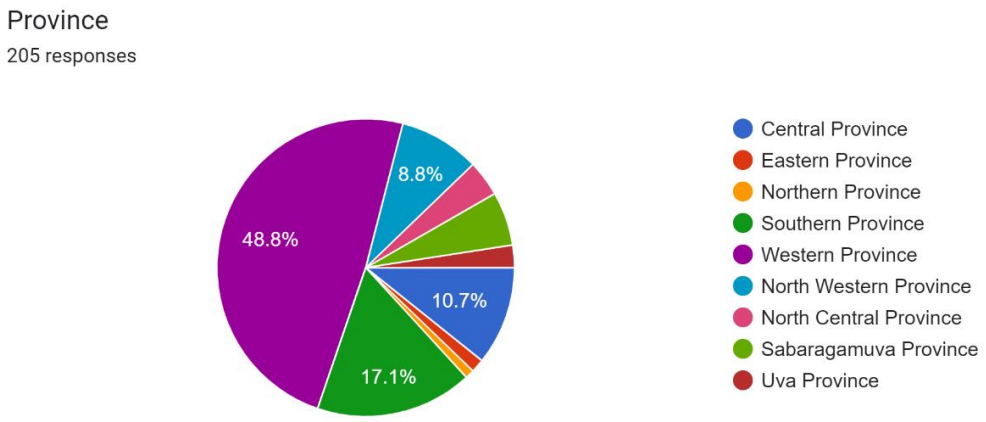

Figure 1: Geographic distribution of the participants the of online survey

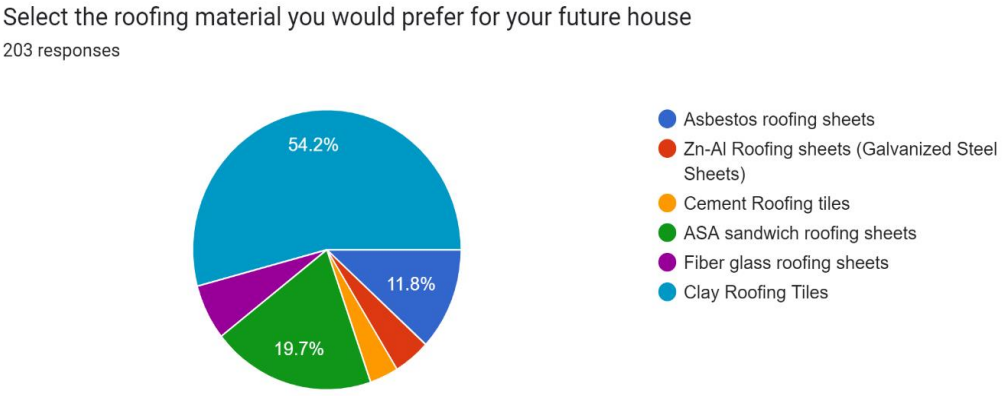

Figure 2: Different types of roofing material preferences of the participants

From the obtained results it can be seen that the highest percentage of participants preferred clay roofing tiles and as the second highest percentage ASA Sandwich roofing sheet type was preferred.

2.2 Defining the goal and scope

The study's main goals were to evaluate the environmental performance of two non-conventional roofing materials in the manufacturing processes. The scope of this study was established using ISO 14040 Section 5.2 (2016) as a guide. The goal of this study was to apply the "Cradle to Gate" approach of life cycle assessment.

2.2.1 Functional unit

The analysis was conducted for a functional unit of roofing materials needed to cover $1m^2$ of roof surface [1].

2.3 Life Cycle inventory analysis

Utilizing the ISO-recommended methods of data collection, the inventory analysis was completed. Data gathering was disrupted by the iterative nature of the inventory analysis.

2.3.1 Product system for clay roofing tiles

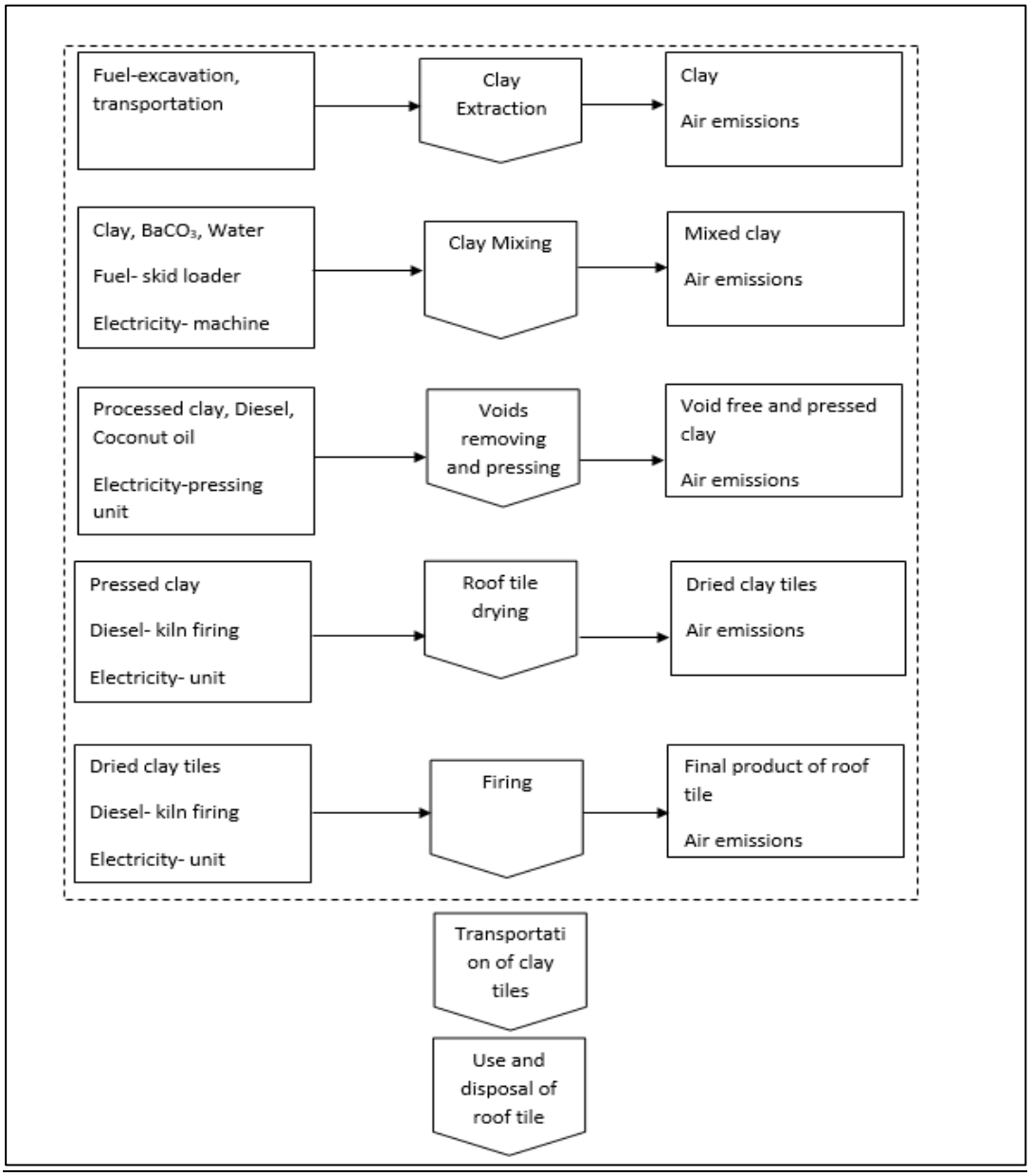

Figure 3: Identification of system boundary of clay tile manufacturing

Data was gathered in line with ISO 14040 section 5.3.2, 2006.,. During the Cradle-to-Gate phase of Clay roofing tiles, data-gathering sheets were created to address input materials and energies, and outputs.

2.3.2 Product system for ASA roofing sheets

Data was gathered in line with ISO 14040 section 5.3.2, 2006. During the Cradle-to-Gate phase of ASA roofing sheets, data-gathering sheets were created to address input materials and energies, and outputs.

ISSN 2961 - 5410 (Online) |

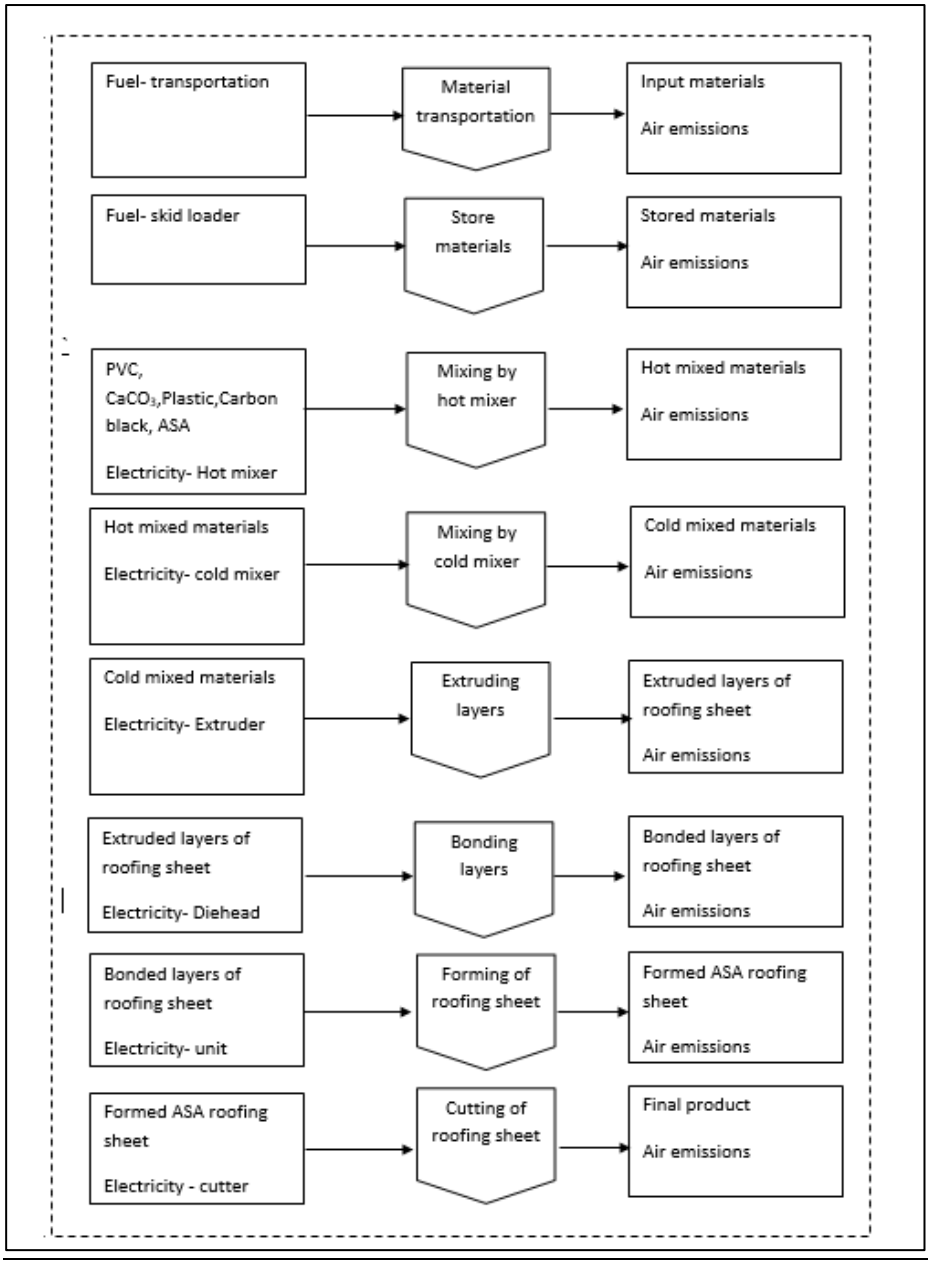

Figure 4: Identification of system boundary of ASA roofing sheet manufacturing

2.4. Impact assessment

The production of clay roof tiles and ASA roofing sheets was modeled using Open LCA software after the completion of the life cycle inventory data. The Ecoinvent database was used for the analysis. The Life Cycle Impact Assessment was conducted utilizing the two standard methodologies: ReCIPe midpoint and endpoint impact categories [1].

2.5 Limitations

The study was carried out only considering the 'Cradle to Gate' analysis of LCA for both roofing materials. Due to the unavailability of the overseas transportation analogy of Openlca software, the material transportation of ASA roofing sheet transportation from overseas was not considered.

3 RESULTS

3.1 Analysis of ReCIPe midpoint (H)

The 18 impact categories were compared for both roofing materials, as presented in Figure 5. Results were generated by considering the entire production process of two roofing materials**.**

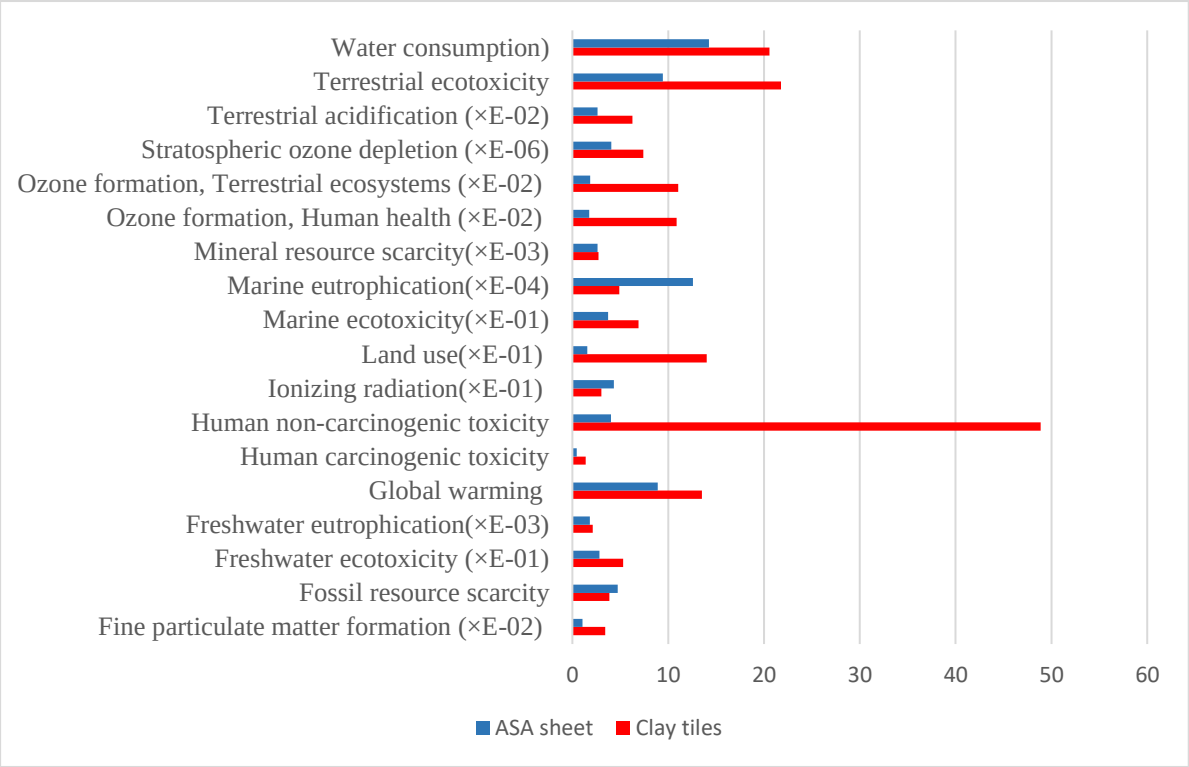

Figure 5: Comparison of Midpoint Impact Categories between the two roofing materials

Clay roofing tiles have the highest impact on Human non-carcinogenic toxicity, Terrestrial ecotoxicity and Water consumption impact categories while the ASA roofing materials have the highest impact on Water consumption, Terrestrial ecotoxicity and Global warming categories. Clay roofing tiles and ASA roofing sheets had a contribution of 13.51 kg CO_2-Eq and 8.90 kg CO_2-Eq contribution of total global warming potential considering all manufacturing stages, respectively. It can be seen that clay roofing tiles have more impact on the global warming potential category than ASA sheets. According to Figure 5, it can be seen that the human non-carcinogenic toxicity midpoint impact category of the Clay roofing tile has increased drastically in comparison to the ASA roofing sheet production. This is due to the usage of $BaCO_3$ in the production of clay roofing tiles because $BaCO_3$ is toxic to human health [6]. Referring to Figure 5, it can be seen that the fossil fuel scarcity of ASA roofing sheet is higher than clay roofing tile. This should be mainly due to the higher electricity consumption of the manufacturing process of ASA roofing sheets as 52% of the total electricity generation of Sri Lanka is from fossil fuel burning [7]. Referring to Figure 5, it can be seen that the Stratospheric Ozone depletion of the clay roofing tile is higher than the ASA roofing sheet. For the clay tile, it was 7.41E-10 kg CFC-11-Eq and for the ASA sheet, it was 4.06E-06 kg CFC-11-Eq per Fuand mixing materials by hot mixer was the hotspot phase of ASA sheet.

A past study conducted in Sri Lanka also had relatively similar results in global warming, acidification, eutrophication, and ozone depletion categories [1,2] and the FU for the study was the same but the hotspot analysis and LCIA methodology and software used were different from this study. For the comparison, a similar study done for clay roofing tiles, in Malaysian context had, 17 kg CO_2-Eq, 0.000462 kg N-Eq, 0.0695 kg SO_2-Eq, 4.82E-10 kg CFC-11-Eq for Global Warming, Marine eutrophication, Acidification, Ozone Depletion midpoint impact categories respectively [8]. As a percentage there was 6%-34% difference with the past study. Similar results can be seen in this study as well.

ISSN 2961 - 5410 (Online) |

There are no past studies in the Sri Lankan context assessing the life cycle analysis of ASA roofing sheets using any kind of LCA software. However, globally some studies have researched the life cycle analysis of PVC roofing material. For ASA roofing sheet production, PVC has the highest contribution of input materials. Therefore, it is convenient to make a comparison between those studies and this study in the same significant impact categories. Also, the functional units of those studies were the same, and the 'Cradle to Gate' methodology had been used. Carlisle Sure-Flex PVC Membranes(2.32mm) [3], White SPPR PVC roofing membrane (1.21mm) [4] were the materials considered for comparison and for Global Warming(8.8, 5.2 kg CO_2-Eq), Marine eutrophication(0.146, 0.076 kg N-Eq), Acidification(0.052, 0.029 kg SO_2-Eq), Ozone Depletion(1.4E-06, 5.5E-07 kg CFC-11-Eq) midpoint impact categories were the results obtained for those materials respectively. It can be seen that the difference with ASA roofing sheet's results for Global warming midpoint impact category was at 1.1% and 41% for Carlisle Sure-Flex PVC Membranes and White SPPR PVC roofing membrane respectively.

3.2 Identification of hotspot base on midpoint impact categories

Referring to Figure 6, it can be observed that the hotspot is the firing phase of clay tile production for all the impact categories. According to past studies [1], the chamber firing phase produces the most greenhouse gas emissions, whereas this study also shows that the kiln firing of the clay tile production produces the most environmental emissions.

3.2.1 Hotspot analysis for clay roofing tiles

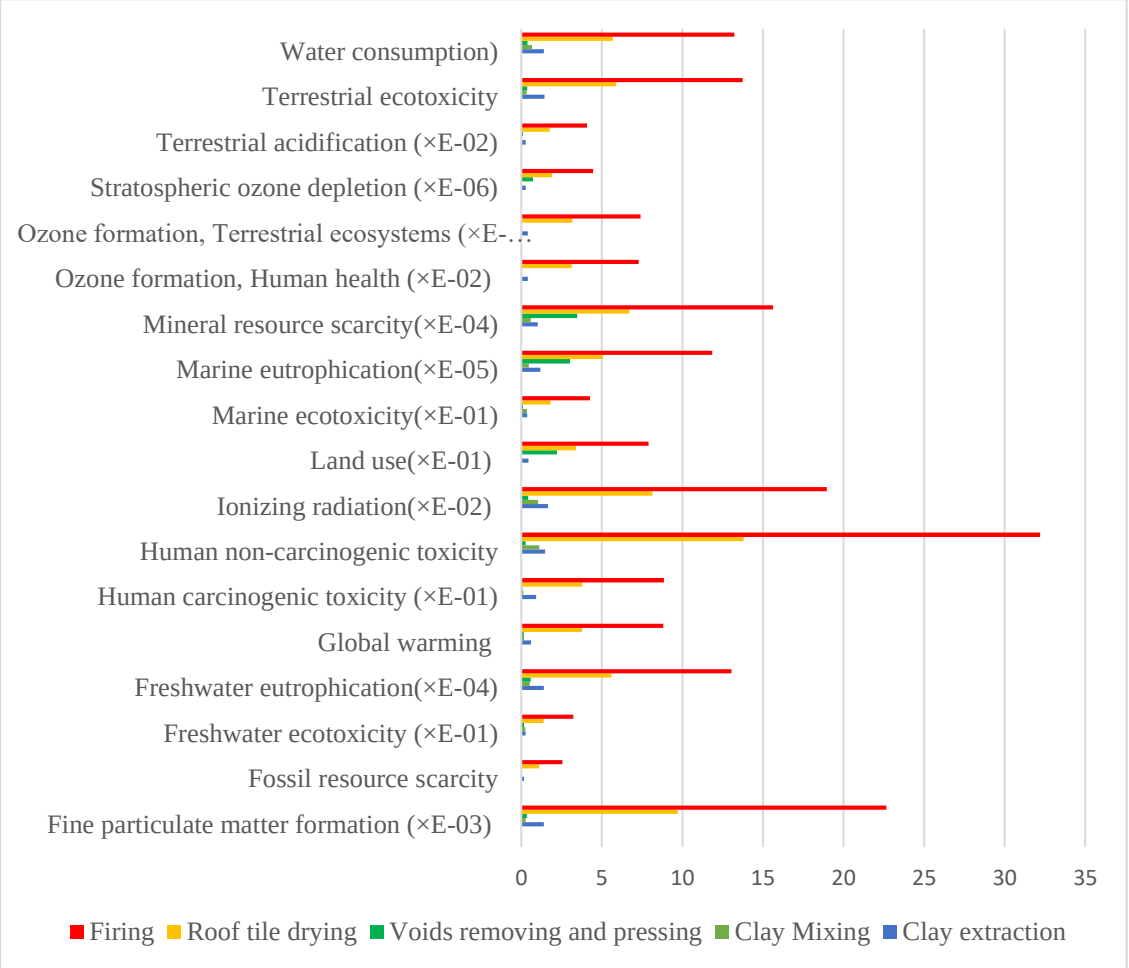

Figure 6: Hotspot analysis for Clay roofing tiles

3.2.2 Hotspot analysis for ASA roofing sheets

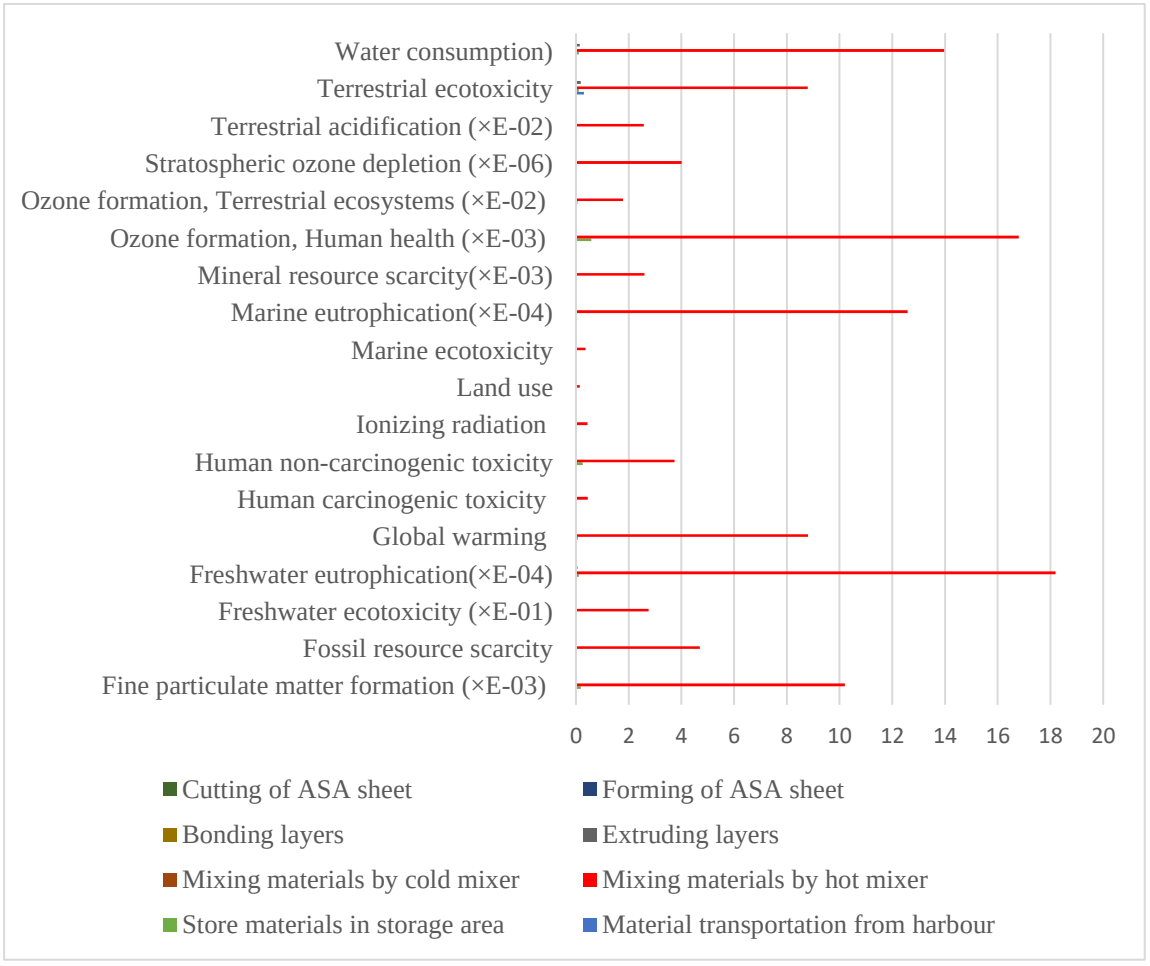

Figure 7: Hotspot analysis for ASA roofing sheets

Referring to Figure 7, it can be observed that the hotspot is the mixing materials by the hot mixer phase of ASA roofing sheet production.

3.3 Analysis of Recipe Endpoint (H, A)

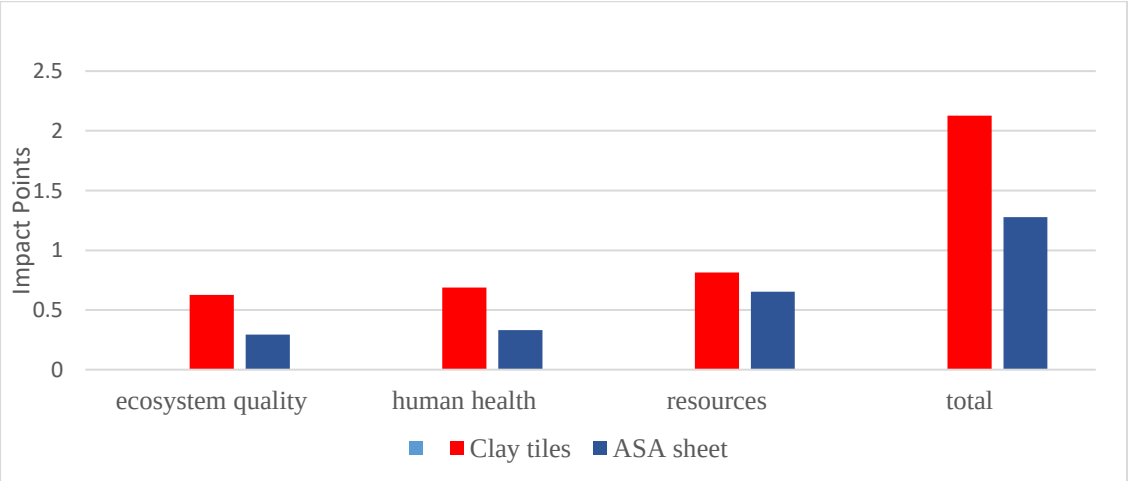

Figure 8: Comparison of endpoint categories for roofing materials

ISSN 2961 - 5410 (Online) |

According to Figure 8, clay tiles have resulted in 0.624781, 0.68797971 and 0.814012 impact points with respect to ecosystem equality, human health and resources. From all three endpoint categories, clay tiles have more impact on the environment than ASA sheets and also from total endpoint impacts, clay tiles have 2.1268 Impact points while ASA sheet has only 1.2761 Impact points. As a percentage, clay tiles have 39% more impact than ASA sheets indicating better sustainability performance.
A past study for LCA of Asbestos roofing sheets, conducted locally had results, for total endpoints as 2.95 Impact points [2]. Also, another past study for LCA of Calicut-Type clay tiles conducted locally had results, for total endpoint as 0.41 Impact points [1] while a study conducted in the Brazilian context showed the total endpoint resulting in 2.06 impact points [9]. It can be noted that this study also has approximately similar results for total endpoints compared to the Brazilian context than the locally conducted study for Calicut-type roofing tiles.

4 CONCLUSION

The main goal of this study was to compare two different non-conventional roofing materials to determine how much impact each one had on the environment. The effect on the endpoint categories was discovered after acquiring the quantitative impacts of the production of clay roof tiles and ASA roofing sheets using two modern manufacturing procedures. The clay roofing tile and ASA roofing sheet were examined based on the stated system boundary, Cradle to Gate life cycle of the product. Five important midpoint impact categories were evaluated across the complete manufacturing process in both factories. The production process of clay roofing manufacturing process produces, human-non-carcinogenic toxicity of 48.87209 kg 1.4-DCB, global warming of 13.50554 CO2 eq, fossil resource scarcity of 3.876369 kg oil eq, stratospheric Ozone depletion of 7.41E-06kg CFC-11-Eq, Terrestrial acidification of 0.062769 kg SO2-Eq while ASA roofing sheets produce, human-non-carcinogenic toxicity of 4.043057 kg 1.4-DCB, global warming of 8.902324 CO2 eq, fossil resource scarcity of 4.730785 kg oil eq, stratospheric Ozone depletion of 4.06E-06 kg CFC-11-Eq, Terrestrial acidification of 0.026102kg SO2. When assessing the results obtained from 'OpenLca' software from both midpoint and endpoint impact categories, it is evident that the most impactful roofing material production procedure belongs to clay roof tile production.
This is mainly due to the kiln firing process of the manufacturing procedure, and it can be identified as the environmental hotspot of the process. Also, mixing materials using a hot mixer was identified as the hotspot phase of ASA roofing sheet manufacturing procedure and this is due to the high material consumption of that phase compared with the entire procedure and high electricity consumption. When considering the evaluated endpoint environmental impacts of both roofing materials, it can be seen that the impacts on the ecosystem, human health, and resources, the clay roofing tile manufacturing process has acquired higher points than the ASA roofing sheet production process. Nevertheless, considering the impacts on resources, both roofing materials have shown approximately the same results. In conclusion, the results depict that the manufacturing process of clay roofing tiles impacts more in both midpoint and endpoint impact categories according to the ReCIPe method. This is mainly due to the identified hotspot phase, kiln firing of the manufacturing process and the high amount of diesel burning. This could be reduced by introducing alternative methods for the firing process.

REFERENCES

Kulatunga, A. K., Peiris, R. L., & Kamalakkannan, S. (2020). Evaluation of Environment Sustainability of Clay Roof Tiles Manufacturing Practices in Sri Lanka using LCA Technique. *Engineer: Journal of the Institution of Engineers, Sri Lanka*, *53*(4), https://doi.org/10.4038/engineer.v53i4.7425

Kuruppuarachchi, K. A. B. N., & Ihalawatta, K. (2014). *Life Cycle Assessment of two different Clay Roofing Tiles*

Carlislesyntec.com. https://www.carlislesyntec.com/en/Document-Viewer/pvc membrane-environmental-product-declaration-epd/6177d225-0e89-b8bb-4b59-a380c83e6b93

An Environmental Product Declaration. (n.d.). Retrieved November 12, 2022, from https://vinylroofs.org/wp-content/uploads/2020/04/CFFA-EPD_FINAL_210220201.pdf.

Department of Census and Statistics. (2020). *Department of Census and Statistics-Sri Lanka*. Statistics.gov.lk. http://www.statistics.gov.lk/

Barium poisoning: an uncommon cause of severe hypokalemia. (n.d.). *Taylor & Francis*. https://www.tandfonline.com/doi/full/10.1080/24734306.2019.1691340

100% Electricity Generation through Renewable Energy by 2050 – Assessment of Sri Lanka's Power Sector – A Joint Report by UNDP and ADB - Bio Energy Association of Sri Lanka. (n.d.). https://www.bioenergysrilanka.lk/100-electricity-generation-through-renewable-energy-by-2050-assessment-of-sri-lankas-power-sector-a-joint-report-by-undp-and-adb/

Ahmad, M. N., & E.Jaafar, E. N. Shuhada. (2017). Comparative life cycle assessment (LCA) of clay versus concrete roofing tiles production in Malaysia. *Journal of Industrial Technology*, *25*(1), 29–41. https://doi.org/10.21908/jit.3

Souza, D. M. de, Lafontaine, M., Charron-Doucet, F., Bengoa, X., Chappert, B., Duarte, F., & Lima, L. (2015). Comparative Life Cycle Assessment of ceramic versus concrete roof tiles in the Brazilian context. *Journal of Cleaner Production*, *89*, 165–173. https://doi.org/10.1016/j.jclepro.2014.11.029

ISSN 2961 - 5410 (Online) |

Contact Position Estimation in the Event of Simultaneous Multiple Contacts in Vision-based Tactile Sensors

Senarath W. A. T. N, Fernando S. A. W
Department of Mechanical Engineering, Sri Lanka Institute of Information technology
New Kandy Road, Malabe, 10115, Sri Lanka

Rajakaruna R. M. T.P
Department of Mechanical Engineering, Sri Lanka Institute of Information Technology
New Kandy Road, Malabe, 10115, Sri Lanka
thilini.ra@sliit.lk

ABSTRACT

Tactile sensors are used to detect physical contact or pressure. They provide feedback about the physical environment and allow more natural and intuitive interaction with machines. Tactile sensors have many applications in the fields of agriculture, space exploration, health and automotive. Capacitive, resistive, as well as vision (optical) based tactile sensors have been proposed in the literature. This paper proposes a novel approach to solving the problem of estimating the contact locations in the event of simultaneous multiple contacts in vision-based tactile sensors. The relationship between the contact force and the resulting physical deformation of the sensor material of a large-scale tactile sensor was studied with the aid of a custom-built hardware unit. Hardware architecture consists of a custom-designed flat rectangular sensor surface coupled with a mono-vision camera to capture the surface deformation. This method can capture detailed information on the resulting deformation for multiple simultaneous contacts. A software -based deformation estimation algorithm is proposed, where the grid array of marker positions was estimated with a tracking algorithm, an estimation algorithm, and a graphical representation algorithm. Moreover, separate analyses have been carried out to find the best suitable method to observe the deformation of the sensor material. In this study, the approach that was taken to find the contact position and deformation, produced results with an accuracy of more than 97%. Consequently, these results show that this method outperforms existing state-of-the-art techniques in terms of accuracy in the detection of the contact position.

KEYWORDS: *Vision-based tactile sensors, Surface deformation, marker-based localization, Contact point estimation*

1 INTRODUCTION

Human body contains many organs that help humans work, learn and adapt to given environments and applications. Skin is one of the most extensive and complicated organs in the human body responsible for sensations like touch, temperature, and pressure. These sensations help humans to work smoothly and flawlessly. The application of tactile sensors in the fields of agriculture, space exploration and automotive are the use of robotic grippers for plucking harvest, texture, and material hardness monitoring of soil via remote space rovers and touch controls in human machine interfaces.(Wan et al., 2017). In the health care field of application, tactile sensors are mainly used for breath monitoring, wound healing, and pulse monitoring applications. Moreover, tactile sensors are used for voice monitoring and knee motion monitoring applications as well (Liu et al., 2020). Tactile sensors provide additional information during a robot's movements, like gripping and touching. This information is helpful because objects have different physical properties for surface hardness and surface textures. Therefore, they need to be handled at different pressure levels. Therefore, the tactile sensor can help provide that additional information. Figure 1 shows the difference between human tactile and artificial tactile sensations.

ISSN 2961 - 5410 (Online) | https://doi.org/10.54389/HHZM8357

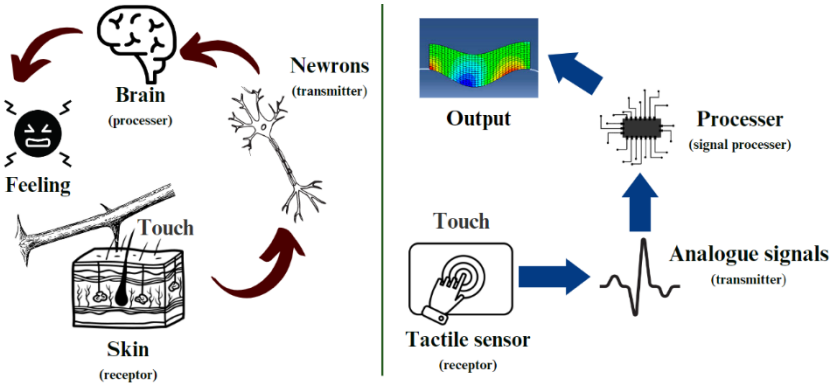

Figure 1: Human tactile sensation and artificial tactile sensation

Tactile sensors can detect deformation when they come into contact with an object, and a suitable technique is used to convert the resulting physical deformation of the contact to an electrical signal. Then these data or the signals are fed into a computer or a microcontroller to carry out the preprocessing and extraction of data. Thereafter, data features like resistance, capacitance, or pixel coordinates, are subjected to a mathematical model to obtain the necessary contact information like coordinates of the contact and the depth of the contact. Currently, vision-based tactile sensors can be seen in industry. Nevertheless, the availability of commercial vision-based tactile sensors is low due to the high cost.

There are mainly three types of tactile sensors based on the working principle: capacitive, resistive, or vision (optical) based tactile sensors. The basic principle behind the capacitive sensors is that the distance between the two plates decreases when there is a force on the sensor. As a result, capacitance changes, and the capacitance level is calibrated to represent a given pressure value. In resistive type tactile sensors, instead of dielectric material, there is a resistive material. When there is a force on the sensor distance between the two terminals decreases, the resistivity of the sensor changes accordingly. However, these sensors are difficult to implement on a large scale in complex geometries. Moreover, capacitive and resistive type sensor surfaces are vulnerable to damage; this is mainly because they come into direct contact with the surface; in vision-based tactile sensors, the electrical components are at a significant distance from the surface, as a result when an excessive force is applied, it is more prone to damage than vision-based tactile sensors. As a result, vision-based tactile sensors can be used in such scenarios.

Vision-based tactile sensor systems can be developed by tracking the movement of maker points. When a force is applied to the soft material of the sensor surface, deformation of the soft material can be seen. Then, using vision-based algorithms, the deformation is estimated with the aid of close-range high-resolution camera capture. Each method has its advantages and disadvantages. The light conductive membrane method can measure contact position and force on soft material; the reflective membrane method can measure the surface texture of the contact object and position, and the marker displacement method can be used to measure contact position shear and torque on the soft material (Van Duong & Ho, 2021a). In this study, a low-cost large-scale vision-based tactile sensor is to be developed to express and enhance the true versatility and potential of the tactile sensation. Thus, this study on vision-based large-scale tactile sensors is mainly focused on the marker displacement approach. The main reason behind this approach is that surface geometry can be changed as required and also depending on material availability. Therefore, at the end of this study, a low-cost large-scale tactile sensor can be introduced to improve the applications of tactile sensors and the sustainability of engineering environments.

In brief, this paper will explore the specific area of engineering related to vision-based tactile sensors, with a focus on a novel approach to solve the problem of estimating the contact locations in the event of simultaneous multiple contacts. The paper will also provide a detailed analysis of the current state of research in this field, as well as new perceptions and impacts. Subsequently, results obtained from the research will be analyzed and discussed. Finally, by examining these important matters, this research aims to make a significant contribution to the field of engineering and provide

ISSN 2961 - 5410 (Online) |

valuable insights for researchers and engineers to further research on how tactile sensors significantly impact the development of robotics and other applications.

2 LITERATURE

Recent studies have explored various approaches to develop vision-based tactile sensors. Depending on the way deformation is observed and the purpose of the tactile sensor, mainly three types of approaches can be observed in all the past approaches. One method is the reflective membrane approach, which was used by Elliott Donlon et al. in their compact version of the GelSight sensor. By using a semi-specular gel coating on the sensor surface, they obtained the surface texture of the grasping surface as output (Donlon et al., 2018). Another approach, taken by Xinghao Zhu et al., involves using a deformable elastomer as the sensor surface and a Generative Neural Network (GNN) model to reconstruct the deformation of the contact. The ground truth data was generated in a simulation environment using the Finite Element Method (FEM) (Zhu et al., 2022). Gomes et al. used the light conductive method and a 2D convolution neural network (CNN) to obtain the heat map of the deformation, which enabled them to find the contact position on the sensor surface (Gomes et al., 2020). Duong Van Lac et al. used the Inverse Finite Element Method (IFEM) to estimate both the deformation and force on the sensor surface, with the marker tracking method used to observe the deformation (Van Duong & Ho, 2021b). Vijay Kakani et al. also used the marker tracking approach to observe the deformation of the sensor surface, but their main focus was to estimate the contact force (Kakani et al., 2021). According to the above recent studies, many approaches have been taken to observe the deformation and estimate the deformation.

3 METHODS

3.1 Sensor surface design

The design of the sensor surface is one of the critical steps of this study, mainly because the material properties and dimensions of the sensor surface will directly affect the robustness and sensitivity of the sensor surface. Therefore, throughout the sensor surface design process, some design selections and analyses were carried out to ensure the sensitivity, durability, and effectiveness of the sensor surface for this study. Some of the main steps that were taken during this phase were technique selection, design selection, and dimension selection.

In the technique selection step, a suitable method was selected to observe the deformation of the sensor surface. During this design section, factors like the effectiveness of the method and the complexity of the design were mainly considered. The light conductive method is an effective method to observe the contact position, but it is a slightly complex approach when compared with the refractive membrane method. The refractive membrane method is more effective when compared with the marker displacement method, but the complexity is greater than the marker displacement method. Although the effectiveness of the marker displacement method is less than the reflective membrane method, it can be further improved by increasing the density of marker points and emerging the marker points away from the sensor surface. Thus, the marker displacement method is a useful method to observe the deformation of the sensor surface effectively.

In the design selection step, several physical factors related to the sensor surface and fabricating methods were discussed. The main aim of this selection is to find the best suitable material, shape, dimensions, and manufacturing process for the sensor surface. The material will determine the robustness and sensitivity of the sensor surface. The manufacturing process will determine the surface finish and the uniformity of the sensor surface. Thus, it is necessary to consider both the material and manufacturing process of the sensor surface at once. When considering those factors, 3D printing using Thermoplastic Polyurethanes (TPU) is the most suitable option for manufacturing the sensor surface; a flexible material that can be used as a filament in 3D printing. The shape of the sensor surface will determine its practicality of the sensor surface. The convex surface can be used in grippers, and cylindrical surfaces can be used in robotic arms. In this study, a flat rectangular surface has been selected to demonstrate the working principle of the sensor surface.

The physical design of the sensor surface mainly depends on specific design parameters. These parameters will have a direct relationship with the accuracy and sensitivity and the manufacturing complexity of the design. The main design parameters are the number of marker points on the sensor surface, the marker point radius, and the thickness of the sensor surface. Since marker points can describe the deformation of the sensor surface, increasing marker point density in a unit area will increase the resolution of the observed deformation. This will increase the accuracy of the contact point estimation. However, some limitations are observed when increasing the marker point density. For example, excessively increasing the marker point density will negatively affect the detection of marker points under complex deformations. Therefore, to measure the deformation effectively, it is necessary to determine the most suitable marker point density. The marker point area will also affect the detection of marker points. When the area of the marker points increases, it will have a lesser possibility of disappearing from the camera view. Furthermore, the height of the marker points will improve the sensitivity of the sensor surface, but excessively increasing the height of marker points will cluster the marker points under minor forces. The thickness of the sensor material has a significant impact on the sensitivity of the sensor surface. Thus, the amount of deformation for a given force depends on the thickness of the sensor surface. Figure 2 shows a simulation carried out in the Solidworks 2019 environment to find the most suitable material and the thickness of the material for the sensor surface. (*Downloads | Support | SOLIDWORKS*, n.d.)

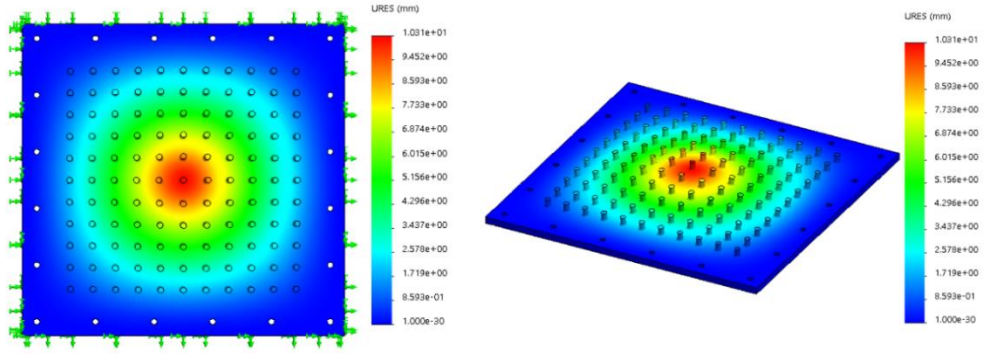

(a) (b)

Figure 2: Deformation simulation of the sensor material; (a)- Front view, (b)- Isometric view

Table 1: Simulation and material parameters

	Parameter	**Value / Description**
Material (Rubber)	Elastic Modulus	0.01 N/mm^2
	Poisson's Ratio	0.45
	Mass Density	960 kg/m^3
	Tensile Strength	20 N/mm^2
Simulation	Mesh density	medium
	Mesh parameters	Standard mesh
	Boundaries	Fixed boundaries

According to the above simulation, the maximum deformation experienced on the sensor surface due to a force of 10N on a $1cm^2$ surface on the sensor is 1.01cm. The thickness of the sensor surface is 3mm. The maximum angle of deformation of the sensor surface with the horizontal is necessary to determine the parameters such as minimum marker point radius, marker point height, and the minimum distance between the marker points. A mathematical representation can be modeled to develop a relationship between those factors, as shown in Figure 3.

ISSN 2961 - 5410 (Online) |

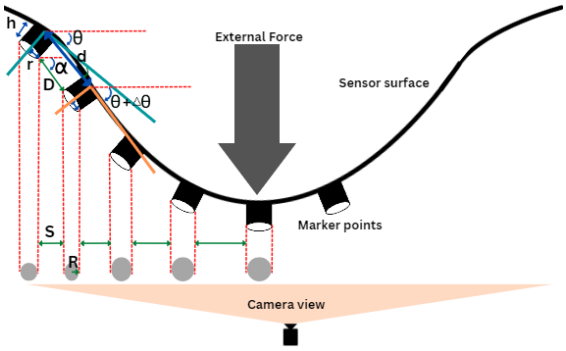

Figure 3: Schematic view of the dimensions of the sensor

$$S = d(\cos(\theta + \Delta\theta)) + h\sin\theta - r\cos\theta - h\cos(\theta + \Delta\theta) - r\,(\cos(\theta + \Delta\theta)) \quad (1)$$

In equation (1), the θ stands for the angle made by the base of the marker point with horizontal, r stands for the radius of the marker point, h stands for the height of the marker point, the horizontal distance between two marker points when deformed is shown by the s and d represents the initial distance between the two marker points. Solving the above-modeled equation, solutions to some design parameters like the appropriate radius of the marker point, the height of the marker point number of marker points, and the thickness of the sensor surface. By considering those factors, the following design is modeled using solid works as shown below in Figure 4.

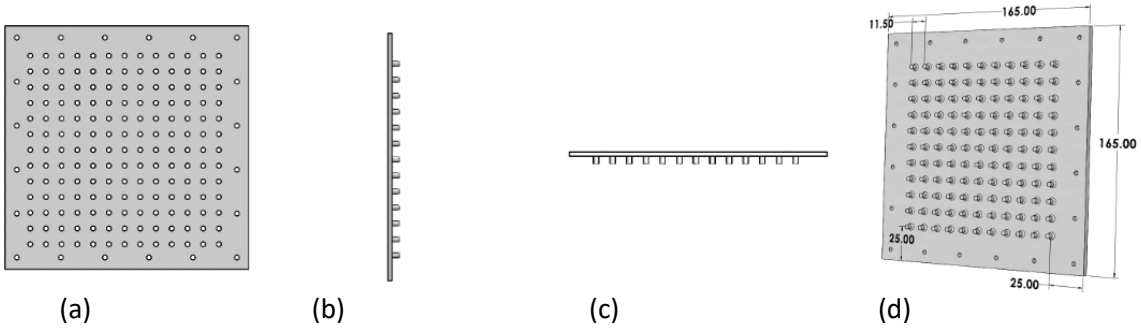

Figure 4: Large scale 3D design of the sensor surface; (a)- Top view of the sensor, (b)- Bottom view, (c)- Side view, (d)- Isometric view with dimensions

3.2 Prototype setup design

The setup consists of components like the outer casing, light source, and camera. Although the main purpose of the casing is to mount and position the sensor surface at the correct distance, it also acts as insulation from the background light. Inconsistency of illumination in a closed environment may increase the noise in the environment. This can be reduced to some extent by covering the reflective

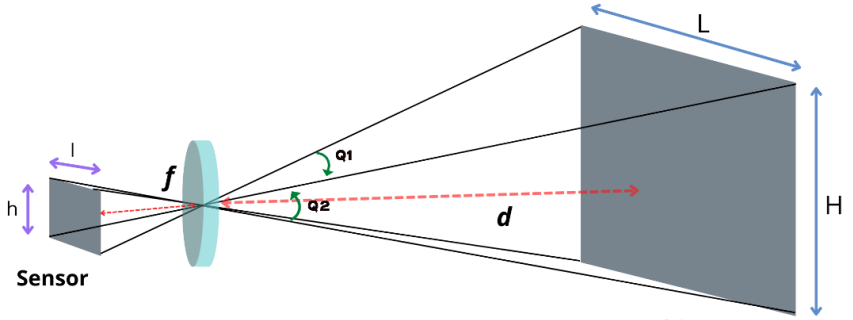

Figure 5: Optical path between object (sensor surface) and camera sensor

surfaces with dark mate material. Consistency and contrast are the two main properties that should be considered when selecting an improved method for insulation. The camera is the main component of the vision system. The supported resolution, frame rate, minimum focus range, and field of view (FOV) are some important parameters that should be considered when designing the vision system. The design of the vision system mainly deals with the estimation of the minimum distance that the sensor surface should be mounted to have a full view of the sensor surface while in the focus range. Sufficient light intensity should be supplied to reduce the noise in the capture frame. Moreover, the light source should be able to disperse the light through the sensor surface uniformly. To derive and model the relationship between the mounting position of the sensor surface from the camera, the optical path of the light rays from the sensor surface should be examined. Figure 5 shows the optical path of the light rays from the sensor surface falling on the sensor surface.

Mainly two factors should be used to determine the minimum distance between the camera and the sensor surface. The camera should be able to view the area of interest, and the distance between the sensor and the surface should be greater than the minimum focusing distance. The required relationship can be modeled considering basic geometric relationships. The equation below shows the relationship between the distance between the lens of the camera with the field of view. In the equations below, the vertical field of view (VFOV) of the camera is represented by *Q2*, while the horizontal field (HFOV) of view is represented by *Q1*. The distance between the camera lens and the sensor surface is generally represented as *d*. During these calculations, the VFOV and the HFOV should be separately counted as two components. Then the distance obtained for *d1* and *d2* will be compared, and the greater value will be selected as *d*. The value obtained for *d* should be compared with the minimum focus range (*F*) distance. To obtain a clear view of the sensor surface, it is necessary to have a *d* value greater than the minimum focus distance of the camera.

$$tan\left(\frac{\mathrm{Q2}}{2}\right) = \frac{(H/2)}{\mathrm{d2}} \quad (2)$$

$$tan\left(\frac{Q1}{2}\right) = \frac{(H/2)}{d1} \quad (3)$$

$$d < F \quad (4)$$

The focus range of the camera is from 10cm to infinity, and the HFOV and VFOV of the camera are obtained directly from camera specifications. According to the above calculations, the distance camera from the sensor surface is obtained as 11.63cm. Since this value is large than the focus range, it can be taken as the minimum distance from the sensor to the camera. Figure 6 shows the finalized design of the casing.

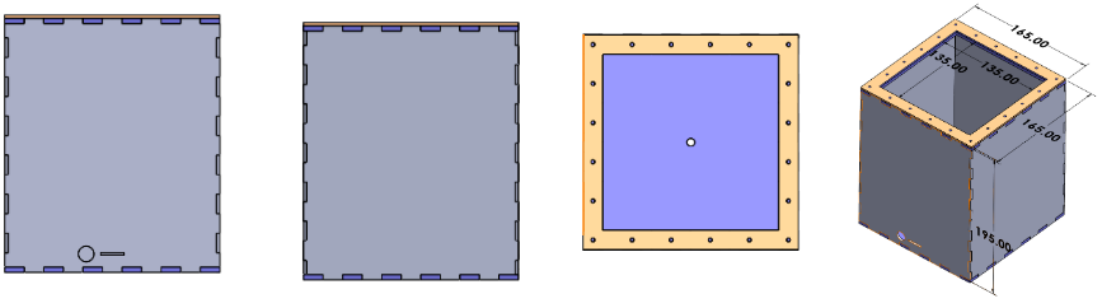

(a) (b) (c) (d)

ISSN 2961 - 5410 (Online) |

Figure 6: 3D design of the sensor casing; (a)- Top view of the casing, (b)- Bottom view, (c)- Side view, (d)- Isometric view with dimensions

3.3 Contact position estimation

Estimation of contact position is carried out using the object tracking algorithm. The tracking algorithm observes the movement of marker points in each consecutive frame. The tracking algorithm is based on pixel-wise calculations. Hence, the distortion caused by the camera should be corrected before applying the image processing operations. Radial distortion and tangential distortion are the main distortion types that may happen due to the fisheye effect of the camera. This can be corrected using the camera calibration algorithm. During camera calibration, the chessboard pattern is viewed from different angles, and several frames are saved. Then using these sample photos, calibration parameters like *k1, k2, p1, p2, and k3* and the new camera matrix were obtained. Eqs. (5) - (6) shows a relationship modeled for radial distortion and Eqs. (7) - (8) shows a mathematical relationship modeled for tangential distortion. The distance between the distortion center and the distorted image point is represented by *r*. The focal length is represented by f_x,f_y, and the optical center is expressed as c_x and c_y. This calibration was performed using OpenCV library functions.

$$X_{\text{Radial distorted}} = x(1 + k_1 r^2 + k_2 r^4 + k_3 r^6) \quad (5)$$

$$Y_{\text{Radial distorted}} = y(1 + k_1 r^2 + k_2 r^4 + k_3 r^6) \quad (6)$$

$$Y_{\text{Tangential distorted}} = x + (2p_1 xy + p_2(r^4 + 2x^2)) \quad (7)$$

$$Y_{\text{Tangential distorted}} = y + (2p_2 xy + p_1(r^4 + 2y^2)) \quad (8)$$

$$Camera\ matrix = \begin{bmatrix} f_x & 0 & c_x \\ 0 & f_y & c_y \\ 0 & 0 & 1 \end{bmatrix} \quad (9)$$

To carry out image tracking algorithms, the frame is treated as an image, and basic image processing techniques are applied. First, the image is cropped and aligned, and the necessary area of interest is selected. This is done to reduce unnecessary pixel computations that are out of the area of interest. This will reduce memory usage and lowers the computational delay. Furthermore, it will be easy to work with one channel and reduce memory usage. This grayscale conversion can be carried out by treating the image as an array. Then the grayscale cropped frames obtained after the above operations were passed through a series of image operations to distinguish marker points from the background. Then a thresholding algorithm is used to separate grey levels as binary black and white. Therefore, white markers will appear as white dots, and the background will appear as black. The exact margin of the threshold level for the separation of each marker from the rest of the background is obtained using the trial-and-error method**.** A certain level of noise will be visible as white patches in the frame. These patches can be treated using morphological operations like open and closing operations. In this scenario, the main objective is to eliminate small white patches. Thus, an opening morphological operation is conducted to remove the unnecessary noise in the image while keeping the area of markers as it is. The strength of the opening operation is dependent on the kernel size, and it has to be selected using a trial-and-error method. This can be implemented by passing the kernel array throughout the image array. The kernel operation will not be applied to the outermost pixel layer due to boundary conditions. This will erode the image size by (n-1) pixels if the kernel is (n*n) kernel. This can be overcome by using padding before the morphological operation.

After these basic image operations, marker points are visible and distinguished from the background. Thus, to detect the marker points, a contour detection algorithm must be used; this will

detect the edges of the object where an intensity gradient happens. These objects will then be appended to an array for further reference. Then using, image operations the area of each closed contour is measured, and if the area is greater than a certain value, it will be considered as a marker point. Then the midpoint of each contour is taken to two variables to denote the x and y coordinates in the image plane. These x and y coordinates of each marker point are joined to have a tuple. Then at the end of each frame, these tuples are appended to form a list. Thereafter, using a conditional statement, length of the list is checked at the beginning of each frame to make sure all the marker points are available. Subsequently, the IDs are given to every marker point to examine them individually. This is mainly carried out to track each marker point throughout the frames. This is implemented by using a counter variable, and when each marker point is detected, the count value will increase. Furthermore, the array is updated to append the ID number of the marker with its coordinates. The ID number is based on the pixel coordinates of the marker points. Thus, the ID obtained by marker points is not in a cartesian order. This will make it difficult to track and do further operations because each time the camera is switched on, the same marker point will get a different ID number. Thus, this will mislead the algorithm and give wrong and invalid results. This can be resolved by implementing an algorithm that organizes the coordinates of the marker points according to the X and Y coordinates and gives the same ID each time when the camera is switched on. Then using the above function, the previously saved marker array will be sorted using the abovementioned function. This will append ID numbers to the marker points according to the coordinates. This can be implemented using nested “if conditions” and a comparison function inside a key function. The comparison function can accept two arguments and compare two arguments to return a value. Then to implement the tracking algorithm, the distance moved by the marker points in each successive frame is measured. If the distance moved by a marker point has changed by more than a certain number of pixels in the successive frame, it will have a new ID number. If not it will have the same ID number. The maximum or the optimum distance moved by a pixel between successive frames is measured using the trial-and-error method. To implement the above algorithm, it is necessary to save the coordinates of the markers at the end of the first frame. To do this first, an empty list should be made to save the coordinates of the first frame, and a variable should be defined to count the number of frames. Then using an if condition, the coordinates of the first frame should be copied to the empty list. Then at each other frame, this list can be referred to by calling the list name with the required ID number. Figure 7 shows some sample outputs at each step.

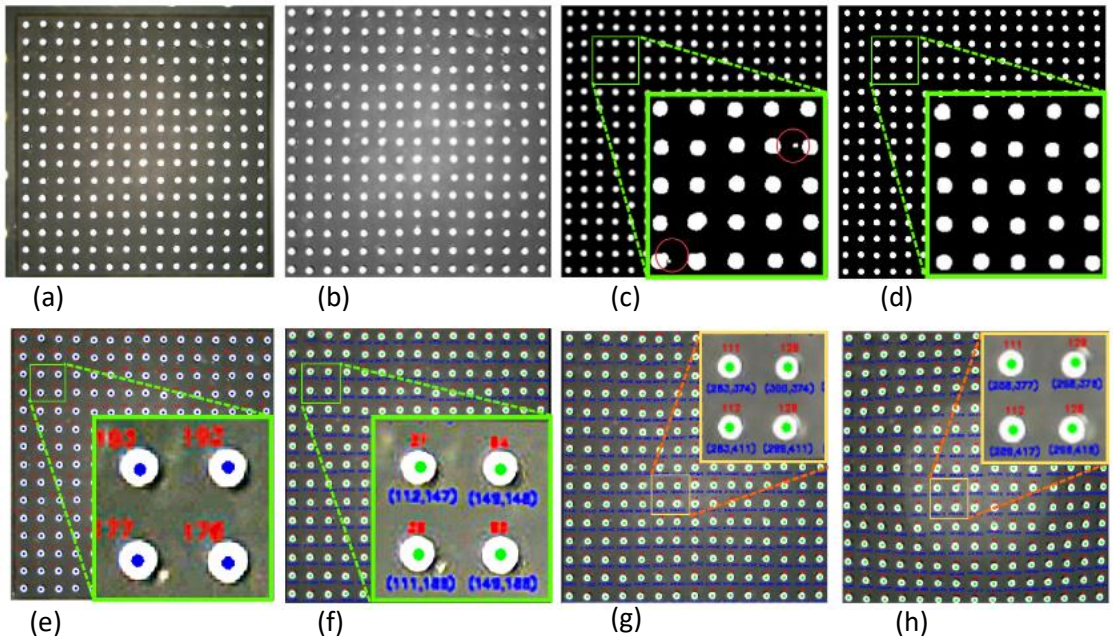

Figure 7: Tracking algorithm implementation; (a)- raw camera image, (b)- gray scale image, (c)- Binary thresholding image, (d)- After morphological operation applied, (e)- Applying ID numbering, (f)- ID sorting applied, (g)- Initial marker IDs, (h)- Marker IDs when deformed.

ISSN 2961 - 5410 (Online) |

Depth estimations mainly differ from each other according to the type of vision that has been used; in a stereo vision system, depth can be obtained from the perspective vision. The process of using a stereo camera to determine depth involves using triangulation and stereo-matching techniques. Calibration and rectification are important to ensure that the problem can be modeled on a 2D plane called the epipolar plane (*Depth Estimation: Basics and Intuition | by Daryl Tan | Towards Data Science*, n.d.). Mono camera depth estimation can be performed using two main methods. Estimation of depth using a pre-trained AI model will be an effective method in the open world. This method cannot be used in this scenario due to the poor accuracy of the results. Thus, to measure the depth using a mono camera, a varying physical factor is selected. The intensity of illumination change in the marker points due to deformation can be taken as a physical factor to measure the depth. To accurately measure the depth, it is required to have a constant light source with fixed intensity. This is a challenging process in this prototype design due to the fluctuations in intensity. Consequently, in this case, the surface perimeter is selected as the physical parameter that changes with time.

Depth estimation using object perimeter involves using the dimensions of an object, which is the distance around the object, to estimate the object's depth or distance from the viewer. This method is a highly effective method for estimating the depth using a mono camera. Figure 8 shows the basic principle behind this method. The letter *m* denotes the distance moved by the object, the letter *a* denotes the image height, and the letter *b* denotes the final perimeter of the object.

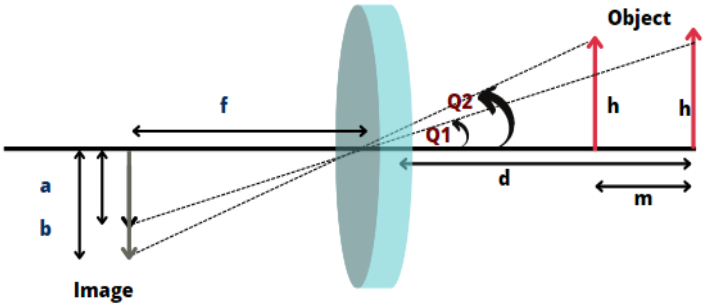

Figure 8: Optical path of image formation on the sensor

Eq (11), shows the modeled relationship between the initial perimeter of the object, the final perimeter of the object, and the distance moved by the object.

$$m = d * (1 - \frac{a}{b}) \quad (11)$$

It is proved that the apparent perimeter of the object increases with the depth and in some scenarios, due to the deformation of the sensor surface. The apparent perimeter of some markers decreases with increasing depth. Thus, this becomes a contradiction to the original concept that was going to be implemented. In order to overcome this issue, instead of taking the perimeter of the markers directly, the perimeter bounded by the corner of four adjacent markers was taken to compare. In this way, the perimeter bounded by the corner markers increases with depth.

.

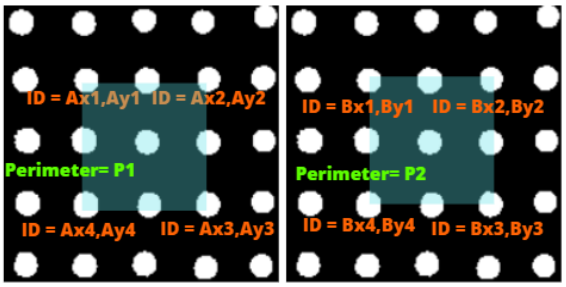

(a) (b)

Figure 9: Deformation vs Perimeter; (a)- Perimeter before deformation, (b)- Perimeter after deformation

To carry out this approach, it is necessary to have the initial coordinates of the markers as well as the current coordinates of the markers. When a point is considered, the algorithm will get the ID number of the markers at the four corner coordinates, then it calculates the area of the markers and compares it with the area of the current marker adjacent coordinates. The above algorithm can be mathematically expressed as follows Eq (12) shows the perimeter of the object before the deformation, while Eq (13) shows the perimeter after the deformation.

$$AP = (Ay1 - Ay4) + (Ax2 - Ax1) + (Ay2 - Ay1) + (Ax3 - Ax4) \quad (12)$$

$$BP = (By1 - By4) + (Bx2 - Bx1) + (By2 - By1) + (Bx3 - Bx4) \quad (13)$$

It can be observed that due to the method that has been implemented to find the depth of the marker points, it is unable to find the *z* coordinates of the marker points at the edge of the image. This can be commonly referred to as erosion of the image, which can be treated using a padding process. In this process, a template that is larger than the frame is merged into the template as shown in Figure 10.

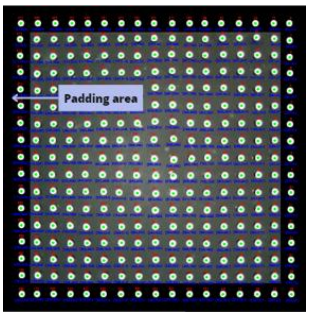

Figure 10: Padded Image

ISSN 2961 - 5410 (Online) |

From the above algorithms, it was able to get the 3D coordinates of the marker points. Then these marker points were plotted in a 3D space to visualize the deformation happening on the sensor surface. Inverse distance weighting (IDW) can be used to resolve this matter. To implement the IDW, the first number of iterations and the search radius should be defined. Then an arbitrary coordinate plane should be made according to the number of iteration values. Then using the coordinates in the area defined by the radius, more coordinates are generated using interpolation. Figure 11 given below shows the general interpolation sample data point. Table 2 shows the sample calculation for the IDW method.

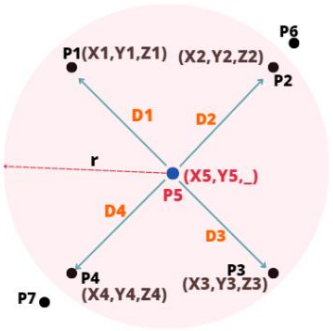

Figure 11: Sample demonstration for point generated from IDW method.

Table 2: Generalized sample calculation

Search radius (r)	Points	Parameter	Distance (d)	1/d	Weight (w)	Value (Z)
r = R	P1	Z1	D1	1/D1	(1/D1) /(1/Dt)	W1*D1
	P2	Z2	D2	1/D2	(1/D4) /(1/Dt)	W1*D2
	P3	Z3	D3	1/D3	(1/D3) /(1/Dt)	W1*D3
	P4	Z4	D4	1/D4	(1/D5) /(1/Dt)	W1*D4
	SUM			∑1/Dt	∑(1/D) /(1/Dt)	∑W*D

4 RESULTS AND DISCUSSION

The proposed contact position algorithm was tested on a Python environment, on a laptop computer with an 8th Gen. Intel® Core™ i7 Processor and 16GB RAM. The camera was able to capture 2560x1440 images with a frame rate of 30 FPs. However, due to the computational lag of the approach, the output of the deformation representation significantly reduced the frame rate to less than one FPS; thus, the 3D mapping algorithm was separately executed at the necessary instance to reduce the overall computational delay. The deformation representation is when a single contact force is applied on the sensor surface; the figures given below show the actual deformation, the camera marker points

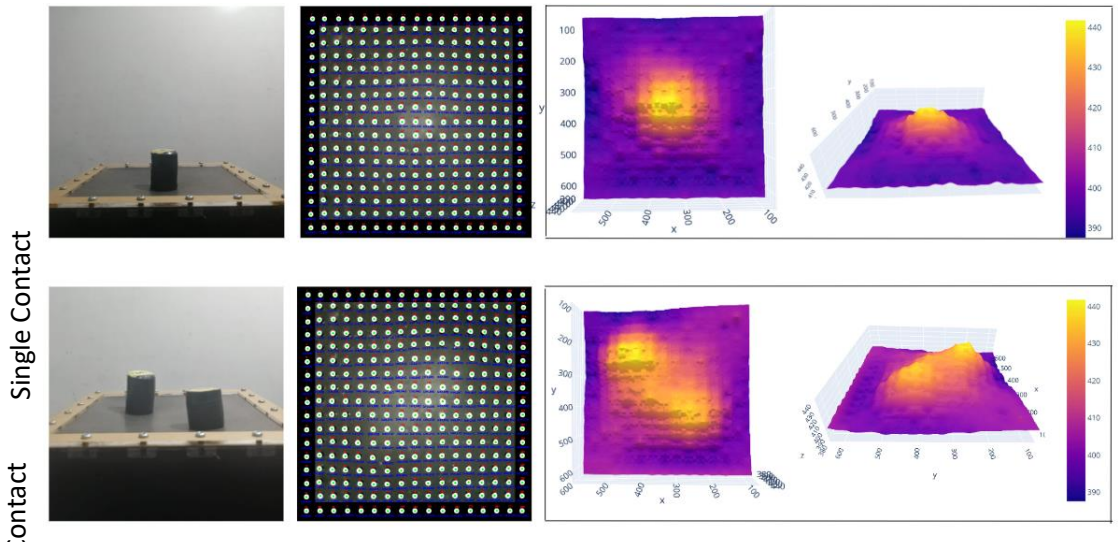

Figure 12: Contact position estimation results; (a)- contact deformation, (b)- Tracking of deformation by algorithm, (c)- graphical representation of the deformation

delocalization, and the virtual graphical representation of the deformation of the sensor surface tracked by the algorithm. When multiple contact forces are applied on the sensor surface, the figures given below (Figure 12) show the actual deformation, the camera marker point delocalization, and the virtual graphical representation deformation of the sensor surface tracked by the algorithm. The deformation given by the algorithm is a 3D representation that can be paned, zoomed and measure deformation at any given point.

Figure 12: Contact position estimation results; (a)- contact deformation, (b)- Tracking of deformation by algorithm, (c)- graphical representation of the deformation

The accuracy of the contact position estimation is measured physically and then compared with the graphical results given by the algorithm. Figure 13 shows the physical approach and the software approach that was used to compare the deformation of the sensor surface. The physical approach shows an effective maximum deformation of the sensor surface as 10.06 mm in the scenario given below, while the simulation deformation shows a 39-pixel value or 10.29mm as the Z coordinate. Thus, this approach was able to yield results with an accuracy of more than 97%. Table 3 shows a comparison and validation of values obtained from the vernier caliper and the developed algorithm.

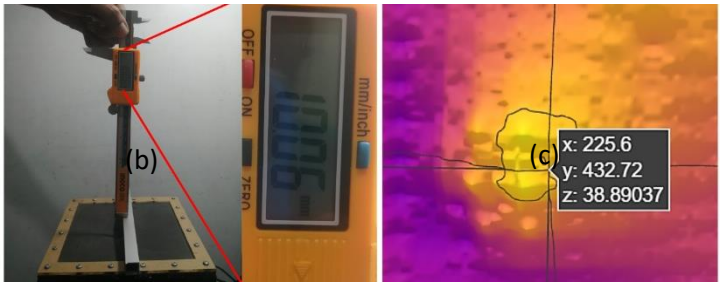

(a) (b)

Figure 13: Accuracy calculation: (a)-Physical depth estimation, (b)-depth estimation using the graphical representation.

Table 3: Results justification and comparison

	X	Y	Z
Measured value (mm)	60	115	10.06
Scale	1 :1		
Software approach (pix)	225.6	432.72	38.89
Software approach (mm)	59.69	114.5	10.289
Accuracy	99.48%	99.56%	97.06%

5 CONCLUSION

Vision-based tactile sensors are a novel approach to artificial tactile sensation. Many approaches have been taken by researchers over the past several years to present new ideas to overcome some challenges with vision-based tactile sensors. This study was also conducted to address some of the existing challenges. The main aim of this study was to implement and design a vision-based tactile sensor that can localize the contact position of the force. The novelty of this study is to design a method to estimate the contact position and the magnitude of multiple simultaneous contacts.

The contact position estimation was carried out by tracking the deformation of the sensor material when a force is applied to it. To track the sensor material deformation, a set of markers was set underside of the sensor surface. Then using a preprocessing image algorithm, these markers were detected. Then a tracking algorithm is used to track the movement of the markers within consecutive frames. Once tracking was implemented, it gave x and y the coordinates of the marker points. To obtain the depth coordinates or the z coordinate, a separate algorithm was set to estimate the depth using the area of the

ISSN 2961 - 5410 (Online) |

marker points. Then these data points were plotted in a 3D space. To increase the density of the points, a linear interpolation algorithm was used. Finally, the 3D plot of deformation is obtained.

The tracking algorithm consists of several image preprocessing steps carried out for many calculations per frame. Thus, the frame rate of the video has been reduced by a considerable amount. The 3D plotting algorithm also requires considerable computational power. Therefore, the plotting process has a substantial amount of delay. The plotting algorithm is not embedded in the main code because it slows down the entire code and lowers the frame rate dramatically. When the contact motion on the surface is high due to computational lag and noise in the image, the program may stop and give errors. These issues can be overcome by increasing the raw computational power or optimizing the code to use parrel computation. In conclusion, it can be stated that, this approach was effective.

REFERENCES

Depth Estimation: Basics and Intuition | by Daryl Tan | Towards Data Science. (n.d.). Retrieved December 17, 2022, from https://towardsdatascience.com/depth-estimation-1-basics-and-intuition-86f2c9538cd1

Donlon, E., Dong, S., Liu, M., Li, J., Adelson, E., & Rodriguez, A. (2018). GelSlim: A High-Resolution, Compact, Robust, and Calibrated Tactile-sensing Finger. *IEEE International Conference on Intelligent Robots and Systems*, 1927–1934. https://doi.org/10.48550/arxiv.1803.00628

Downloads | Support | SOLIDWORKS. (n.d.). Retrieved March 17, 2023, from https://www.solidworks.com/sw/support/downloads.htm

Gomes, D. F., Lin, Z., & Luo, S. (2020). Blocks World of Touch: Exploiting the Advantages of All-Around Finger Sensing in Robot Grasping. *Frontiers in Robotics and AI*, *7*, 127. https://doi.org/10.3389/FROBT.2020.541661/BIBTEX

Kakani, V., Cui, X., Ma, M., & Kim, H. (2021). Vision-Based Tactile Sensor Mechanism for the Estimation of Contact Position and Force Distribution Using Deep Learning. *Sensors 2021, Vol. 21, Page 1920*, *21*(5), 1920. https://doi.org/10.3390/S21051920

Liu, Y., Bao, R., Tao, J., Li, J., Dong, M., & Pan, C. (2020). Recent progress in tactile sensors and their applications in intelligent systems. *Science Bulletin*, *65*(1), 70–88. https://doi.org/10.1016/J.SCIB.2019.10.021

Van Duong, L., & Ho, V. A. (2021a). Large-scale vision-based tactile sensing for robot links: Design, modeling, and evaluation. *IEEE Transactions on Robotics*, *37*(2), 390–403. https://doi.org/10.1109/TRO.2020.3031251

Van Duong, L., & Ho, V. A. (2021b). Large-scale vision-based tactile sensing for robot links: Design, modeling, and evaluation. *IEEE Transactions on Robotics*, *37*(2), 390–403. https://doi.org/10.1109/TRO.2020.3031251

Wan, Y., Wang, Y., & Guo, C. F. (2017). Recent progresses on flexible tactile sensors. *Materials Today Physics*, *1*, 61–73. https://doi.org/10.1016/J.MTPHYS.2017.06.002

Zhu, X., Jain, S., Tomizuka, M., & Van Baar, J. (2022). Learning to Synthesize Volumetric Meshes from Vision-based Tactile Imprints. *Proceedings - IEEE International Conference on Robotics and Automation*, 4833–4839. https://doi.org/10.48550/arxiv.2203.15155

Prediction of Post-Construction Settlement of Road Embankment on Soft Soil Deposits

K. V. D. Vidurapriya
Department of Civil Engineering, Sri Lanka Institute of Information technology
New Kandy Road, Malabe, 10115, Sri Lanka
dinitha.v@outlook.com

G. A. N. Jayaratne
Resource Management Consultants (Pvt) Ltd, Battaramulla, Colombo, Sri Lanka
anupama.jayaratne55@gmail.com

H. S. Thilakasiri
Sri Lanka Institute of Information Technology, New Kandy Road, Malabe, 10115, Sri Lanka
saman.t@sliit.lk

ABSTRACT

Organic soils are often considered problematic soils around the world due to several reasons. Excessive settlement is one of the main concerns when constructing infrastructure on soft grounds with organic soil deposits. Ground improvement is mainly carried out on the sub surfaces that lack the strength and stability to bear the structure to be constructed and undergo large settlement during operation. Different soft-ground treatment methods must be applied based on the soil properties to reduce the expected settlements during construction and operation periods. In this context, it is essential to know the behaviour of the subsurface after the ground improvement process. This study mainly investigates the accuracy of the settlement prediction methods during the post-construction stage of the Colombo-Katunayake Expressway Project in Sri Lanka. Settlement prediction was done for the Defect Liability Period using the hyperbolic method, the Mesri method and the Ladd method. A comparison of the predicted settlement with the measured field settlement was done to assess the accuracy of the settlement prediction methods. The comparison showed that the hyperbolic method was more accurate and convenient for predicting the settlement of the embankment.

KEYWORDS: *Soft ground treatment methods; Preloading; consolidation settlement; Asaoka method; hyperbolic method*

1 INTRODUCTION

Ground improvement is done to strengthen, stabilise, and reduce the post-construction settlement of soft soil deposits. Such ground improvement will minimise the unfavourable settlements in the ground that could lead to the serviceability failure of the structure or, sometimes, ultimate collapse. Fine-grained soils with a particularly high degree of saturation and high organic content, such as peat, could be problematic for both stability and the settlement of embankments (Den Haan and Kruse, 2006; Huat, 2006). For several reasons, the secondary consolidation settlement is often considered more significant than the primary consolidation in organic soils. The time taken to complete primary consolidation is shorter in organic soils, and the soil reaches the end of primary consolidation within a short period from initial loading. However, the secondary consolidation settlement prevails for extended periods, and the magnitude of settlement is also considerably high compared to most inorganic soils (Mesri et al., 1997). Therefore, Preloading and other ground improvement techniques mitigate structural failures during the defect liability period by reducing the magnitude of secondary consolidation settlement. It is crucial to accurately predict the secondary consolidation behaviour during this period to facilitate the initial design process and ensure the embankment's long-term performance. Several methods are used to predict the post-construction settlement of organic soil deposits. In this study, the commonly practised prediction methods such as the hyperbolic method, the Mesri et al. (1997) method

ISSN 2961 - 5410 (Online) | https://doi.org/10.54389/KCZF9855

and the Ladd method (Han, 2015) are used to predict the settlement during the defect liability period and to compare with the measured settlement.

In the Colombo-Katunayake Expressway project, from the chainage K0+000 to K25+800 starting from Colombo, the initial borehole profiles indicate the presence of peat layers throughout the length of the section with a thickness varying from 0.5m to 14.2m. The organic soil is mainly concentrated in the first 8km from the direction of Colombo of the expressway (Hsi et al., 2015). Depending on the thickness of the peat layers and the proposed design, different ground improvement techniques such as; Preloading, Preloading with Prefabricated Vertical Drains (PVD), Crushed Stone Piles, Sand Compaction Piles, and Driven Piles have been used to minimise the settlement of the subsurface. Settlement monitoring was conducted during ground improvement at all sections and some sections for a defect liability period of three years to assess the effectiveness of the soft ground improvement due to the application of the techniques mentioned above. A few such road embankment sections were selected for the present study based on data availability.

2 METHODOLOGY

2.1 Test variables

The study primarily focused on embankment sections using the preloading technique, and the locations selected for the analysis are presented in Table 1.

Table 5: Selected sections for analysis with Preloading

Chainage	The thickness of the peat layer (m)	Depth to peat layer (m)
K3+400	1.4	3.5
K7+800	2.2	5.8
K12+150	12.1	4.4
K13+050	1.4	4
K18+800	1.2	2.8
K19+600	1.9	0.6

Figure 1 presents a typical settlement variation with embankment height for selected K7+800 chainage, consisting of an organic layer of 5.8m thickness.

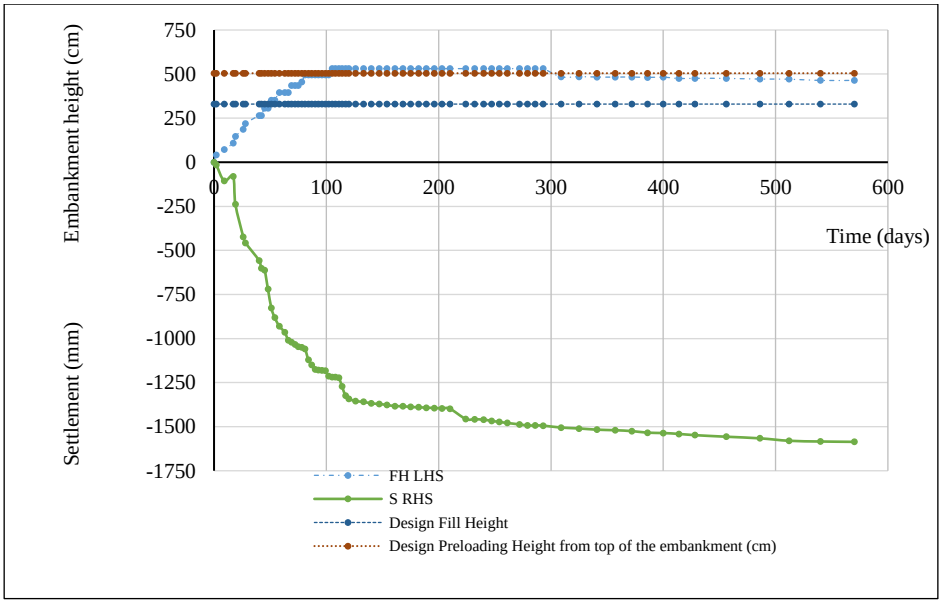

Figure 6: Variation of settlement with embankment height for K7+800

2.2 Applicability of the Asaoka method to field settlement data

Asaoka method is a widely practised settlement prediction method due to its simplicity and ability to determine the end of primary consolidation settlement. (Asaoka, 1978). Asaoka method was applied for the settlement data, where the surcharge loading remained constant, and the end of primary consolidation was obtained. The degree of consolidation attained in the soft soil by the time of removal of the surcharge can be found by determining the end of the primary consolidation settlement.

2.3 Applicability of the hyperbolic method to field settlement data (Tan et al., 1991)

The hyperbolic plot of t/s vs t for the settlement monitoring data during the construction of the embankment was plotted, and the parameters α and β were obtained according to the hyperbolic equation. The settlement was then predicted using the hyperbolic relationship.
The hyperbolic equation in Equation 1 was used to predict settlement at a required time during Preloading.

$$\frac{t}{s} = \alpha + \beta t \qquad (1)$$

Where t is the time of the settlement s is observed, and α and β are constants obtained from the hyperbolic plot of the respective test location.

2.4 Secondary compression based on the Mesri method

Mesri et al. (1997) developed a relationship between C_α'/C_α to determine the secondary compression settlement after surcharge removal. Mesri method can determine the secondary compression index after surcharge removal and the secondary settlement. (Mesri et al., 2001)
Mesri method was applied to determine the secondary settlement after the surcharge removal. C_α'/C_α values cannot be obtained for R values less than 0.2 from the Mesri method, which is an explicit limitation of this method.

Figure 2 presents the Mesri curves, which are used to determine the C_α'/C_α ratio and thereby C_α', the modified secondary compression index.

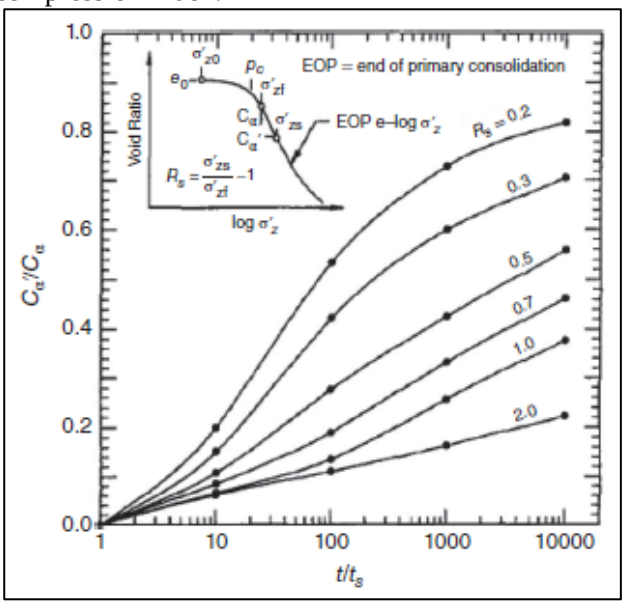

Figure 2: Mesri graphs for C_α'/C_α versus t/t_s (Mesri et al., 1997)

ISSN 2961 - 5410 (Online) |

2.5 Secondary compression based on the Ladd method

Ladd method uses a relationship between the Adjusted Amount of Surcharge (AAOS) and C_α'/C_α to determine the modified secondary compression index (Han, 2015). Figure 3 presents the Ladd graphs, which were used to determine the C_α'/C_α ratio and thereby C_α', the modified secondary compression index. The C_α value for the analysis was obtained from the study done on peaty soil by Ariyarathna et al. (2010), as shown in Equation 2.

$$C_\alpha = 0.033C_C \quad (2)$$

Where C_α is the secondary compression index before surcharge removal, and C_c is the compression index.

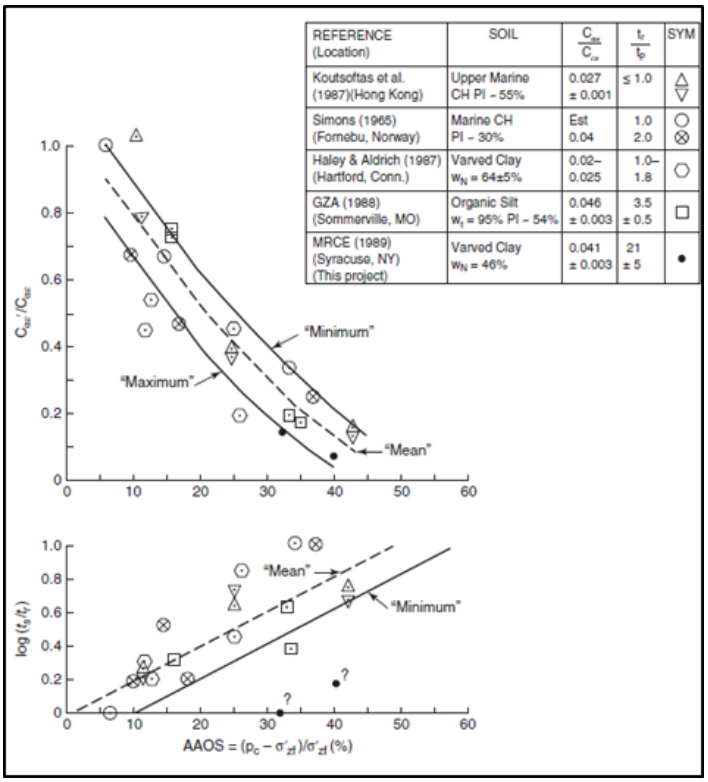

Figure 3: Ladd graphs for C_α'/C_α versus AAOS (Han, 2015)

All the above-stated methods were applied in the determination of the secondary settlement during the construction and service phases.

3 RESULTS

From the application of the Asaoka method on the preloading locations, it was determined that primary consolidation had been completed by the time of removal of the surcharge. The time and settlement data corresponding to the constant embankment load were considered for the Asaoka method application. Figure 4 shows the Asaoka plot for the Left side of the embankment at K12+150 chainage, where k and k-1 are the settlement monitoring data recorded at successive times. The primary settlement obtained by the application of the Asaoka method is presented in Table 2.

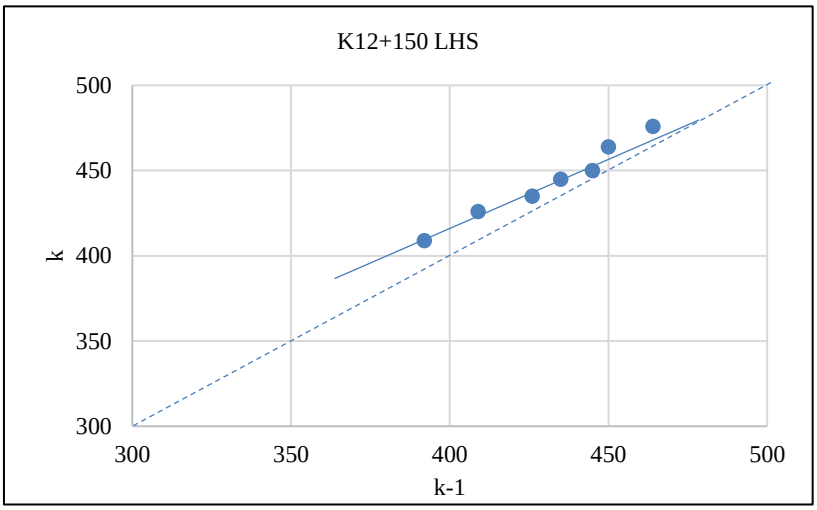

Figure 4: Asaoka plot for K12+150 LHS

Table 2. Primary settlement comparison for preloading locations

Location	Peat layer thickness (m)	Primary settlement (using Asaoka method)		Settlement at the removal of surcharge (mm)		Degree of consolidation achieved (%)	
		LH	RH	LH	RH	LH	RH
K3+ 400	1.4	419	460	423	464	100	100
K7+ 800	2.2	943	1461	978	1494	100	100
K12+ 150	12.1	474	475	484	473	100	99.6
K13+ 050	1.4	407	678	412	686	100	100
K18+ 800	1.2	320	317	312	313	97.5	98.7
K19+ 600	1.9	164	143	162*	140*	98.7	97.9

*Last settlement reading available. No surcharge removal done until the last date of settlement monitoring

The end of primary consolidations was obtained using the Asaoka method, and it was found that the soft soil layer had reached 100% of its primary consolidation by the time of the removal of the surcharge. The hyperbolic plot of *t*/*s* vs *t* for the settlement monitoring data during the embankment construction was plotted. The predicted settlement was then calculated using the hyperbolic equation and plotted against the actual settlement. Figure 5 shows the results of the application of the hyperbolic plot for the K3+400 chainage.

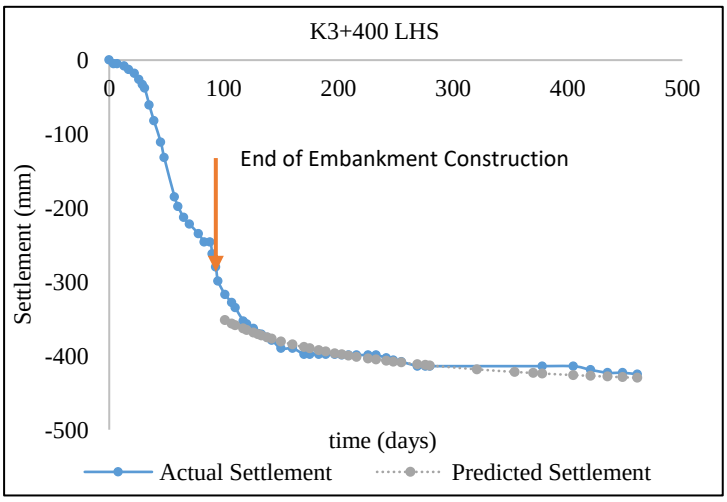

Figure 5: Hyperbolic settlement prediction for K3+400

ISSN 2961 - 5410 (Online) |

According to Figure 5, the actual settlement during the embankment construction stage will closely follow a hyperbolic variation, agreeing with the settlement predicted by the hyperbolic equation. The hyperbolic parameters obtained from the settlement measured during the embankment construction period satisfy the hyperbolic equation; thereby, these parameters will be used to predict settlement in the service period. The secondary consolidation settlement for the service period was also calculated using the Ladd and the Mesri methods after determining the end of primary consolidation. Figures 6, 7 and 8 present the settlement comparisons for chainage K7+800 during the service period obtained using the Mesri, Ladd, and hyperbolic methods.

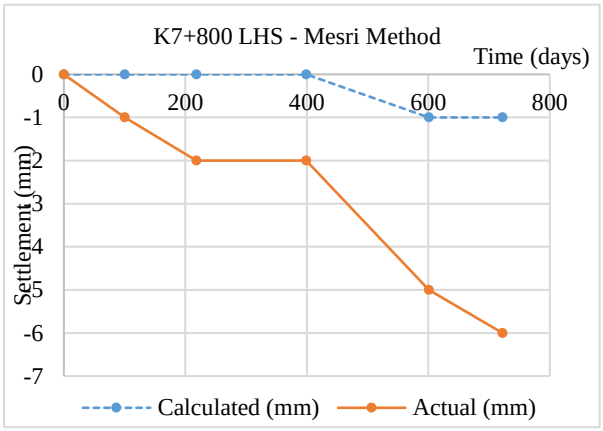

Figure 6: Settlement during DLP using the Mesri method for K7+800 LHS

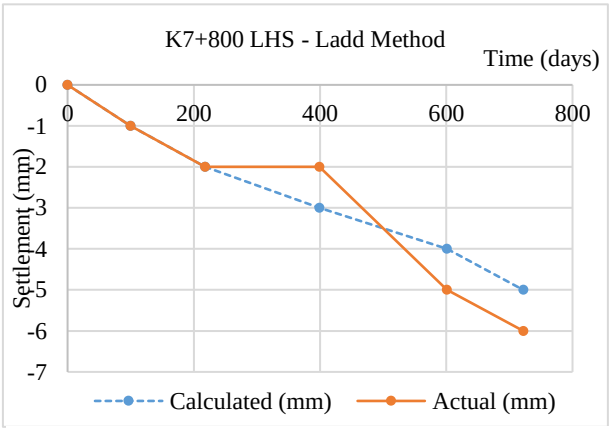

Figure 7: Settlement during DLP using the Ladd method for K7+800 LHS

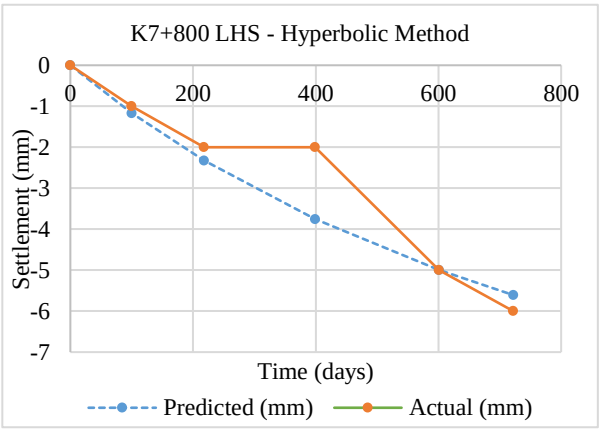

Figure 8: Settlement during DLP using the hyperbolic method for K7+800

4 DISCUSSION

Hyperbolic settlement prediction was more satisfactory for the settlement prediction after the removal of the surcharge load than the other two methods; the Ladd method and the Mesri method. The hyperbolic method was applied to the settlement data for which the constant embankment loading and the hyperbolic equations were obtained. Figure 9 shows the hyperbolic settlement prediction during the embankment construction phase for K12+150 chainage using the hyperbolic parameters obtained during this research. As shown in Figure 9, the variation of the predicted settlement shows similar behaviour to the actual field settlement. Since critical consolidation takes place at the latter stage, at approximately a degree of consolidation of 40% to 90%, the hyperbolic method can be successfully used for settlement prediction during the embankment construction period.

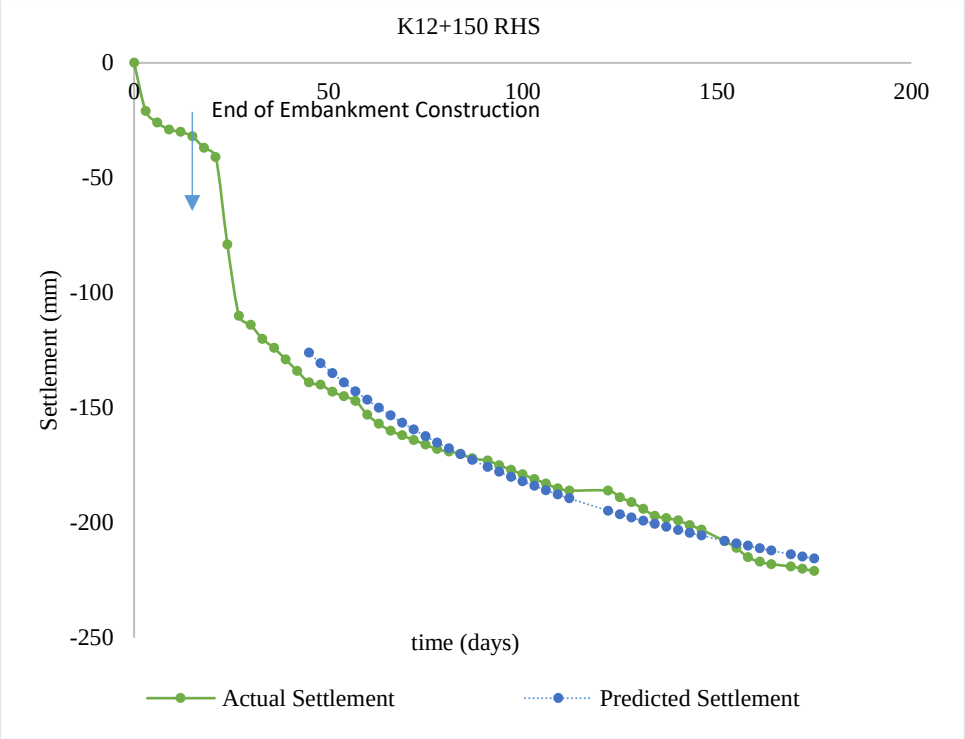

Figure 9: Hyperbolic settlement prediction for K12+150 RHS

Figures 10 to 15 show the settlement comparison for the Defect Liability Period (Service Period) using the three settlement prediction methods where applicable; hyperbolic, Mesri and Ladd methods, against the observed field settlement data for K3+400, K7+800, K12+150, K13+050, K18+800 and K19+600 chainages respectively. Out of these, for chainages K3+400, K18+800 and K19+600, the Mesri method could not be applied as, in the Mesri graphs that are commonly referred to in the industry, the C'_α/C_α variation for R = OCR – 1 values less than 0.2 cannot be found. The lack of C'_α/C_α ratio for soils with lower over-consolidation ratios can be identified as one of the significant limitations of using the Mesri method. Here, t = 0 marks the start of the service period.

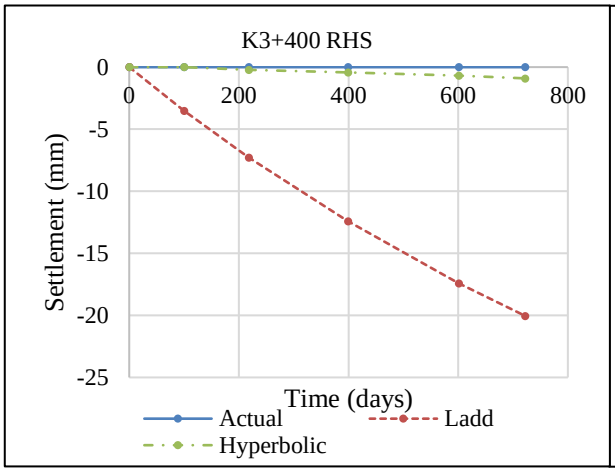

Figure 10: Comparison of Observed settlement values with Predicted settlement values for K3+400

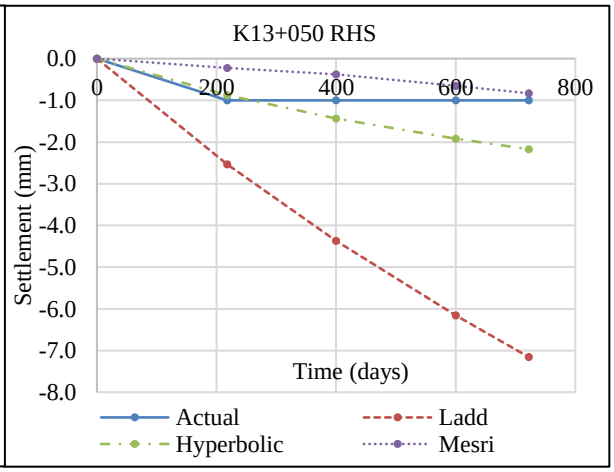

Figure 11: Comparison of Observed settlement values with Predicted settlement values for K13+050

ISSN 2961 - 5410 (Online) |

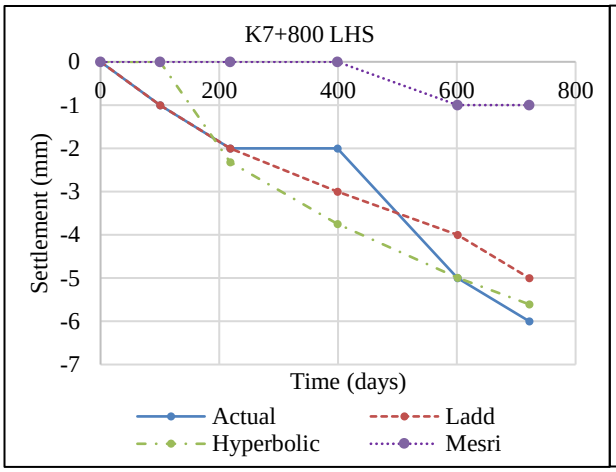

Figure 12: Comparison of Observed settlement values with Predicted settlement values for K7+800

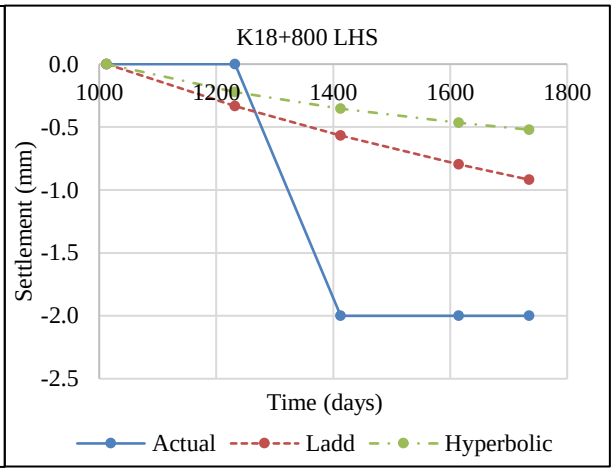

Figure 13: Comparison of Observed settlement values with Predicted settlement values for K18+800

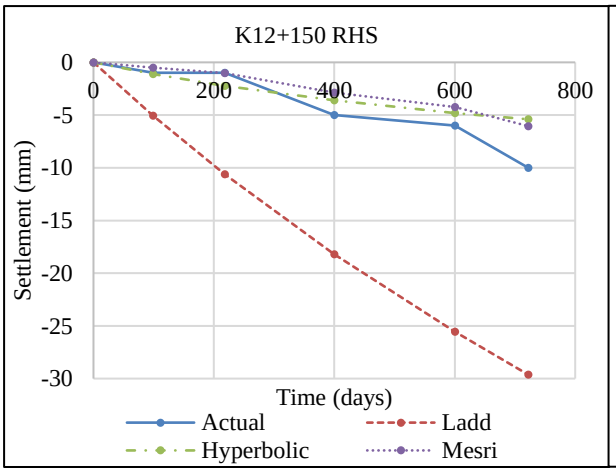

Figure 14: Comparison of Observed settlement values with Predicted settlement values for K12+150

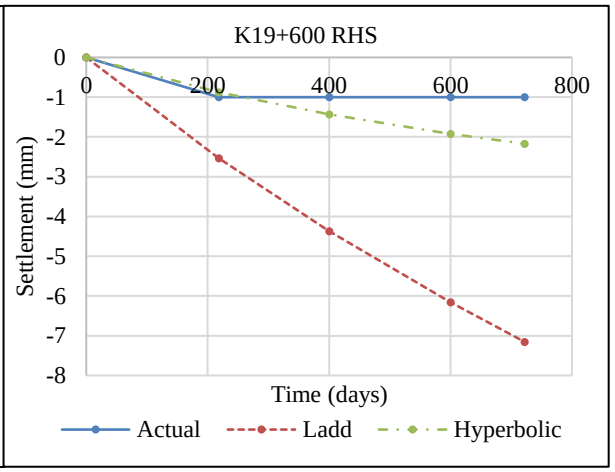

Figure 15: Comparison of Observed settlement values with Predicted settlement values for K19+600

It was discussed earlier in this section that the settlement prediction method based on initial observations could accurately predict the settlement during the preloading stage. Figures 10-15 also show that the most accurate settlement prediction was made using the hyperbolic method, even in the defect liability period. It should also be noted that these hyperbolic predictions were made based on the parameters derived from the settlement monitoring data of the preloading phase. This can be considered an added advantage of the method, as the settlement prediction in the defect liability period does not require additional calculations. In contrast, the Ladd and the Mesri techniques involve a series of calculations to determine the modified coefficient of secondary consolidation after the surcharge removal to predict the settlement.

Mesri method produced the second-best prediction from the settlement comparisons of locations where the method could be applied. Mesri et al. (1997) proposed these curves based on laboratory test results carried out on samples extracted from Middleton peat deposits. According to Hobbs (1986), the properties of organic soils vary drastically from one deposit to another. Though these

curves proposed by Mesri et al. (1997) could accurately predict settlement for organic soils with similar properties to Middleton peat, the same accuracy cannot be expected if used on soil with different properties. Hence, by deriving or utilising C'_α/C_α ratio vs time ratio curves for organic soil deposits that match the soil's properties in consideration, more accurate settlement predictions can be obtained. As Mesri et al. (2001) suggest, the C'_α/C_α ratio varies with the elapsed time. However, in the Ladd method, rather than reporting a C'_α/C_α ratio variation with time, a C'_α/C_α ratio variation with the surcharge load was presented. This can be identified as one of the significant reasons for the considerable divergence between the actual settlement and the settlement predicted using the Ladd method.

5 CONCLUSION

The secondary consolidation settlement of organic soil is considered more important than the primary consolidation settlement for several reasons. Due to this reason, the post-surcharge secondary consolidation settlement of road embankments constructed on soft grounds is considered vital for their long-term performance. This paper compared the results of three post-surcharge secondary consolidation settlement prediction methods widely used in the industry with the measured settlement of the Colombo – Katunayake Expressway embankment sections. After determining the end of primary consolidation from the Asaoka method, all six sections considered in this study showed that the primary consolidation had been completed. The degree of consolidation was nearly 100% when the surcharge was removed. Mesri, Ladd and hyperbolic methods were used to predict the post-surcharge secondary consolidation settlement and later compared with field settlement measurements. The comparison demonstrated that the settlement predicted by the hyperbolic method is the most accurate among the three selected methods. As the hyperbolic method adopts an observational method in predicting the settlement, it eliminates the errors associated with the uncertainty of material properties and behaviours. Moreover, the results suggest that the hyperbolic parameters determined in the embankment construction stage can also be successfully used in predicting post-surcharge secondary consolidation. Therefore, the hyperbolic method facilitates convenient and accurate secondary consolidation settlement prediction during the service period.

REFERENCES

Ariyarathna, P.R.C., Thilakasiri, H.S. and Karunawardane, W.A. (2010) Vacuum consolidation of Sri Lankan peaty soils. Proceedings of the Ann. sessions of Institution of Engineers, Institution of Engineers, Colombo. Asaoka, A., 1978. Observational Procedure of Settlement Prediction. Soils and Foundations, Volume 18, pp. 87-101.

Den Haan, E.J. and Kruse, G.A.M. (2006) Characterisation and engineering properties of Dutch peats. Proceedings of the 2nd Int. Workshop on Characterisation and Engineering Properties of Natural Soils, Singapore. DOI: 10.1201/NOE0415426916.ch13

Han, J. (2015). Principles and Practices of Ground Improvement. 1st ed. New Jersey: John Wiley & Sons Inc.

Hobbs, N.B. (1986) Mire morphology and the properties and behaviour of some British and foreign peats. Quarterly Journal of Engineering Geology 19:7-80. DOI: 10.1144/GSL.QJEG.1986.019.01.02

Hsi, J., Gunasekara, C. and Nguyen, V. (2015) Characteristics of soft peat, organic soils and clay, Colombo-Katunayake Expressway, Sri Lanka. In: Indrarathne B, Chu J (eds), Ground improvement Case Histories, Elsevier, Series 03, Butterworth-Heinemann, 681-722. DOI: 10.1016/S1571-9960(05)80027-8

Huat, B.B.K. (2006) Deformation and shear strength characteristics of some tropical peat and organic soil. Pertanika J. Sci. & Technol. 14(1&2):61-74.

Mesri, G., Stark, T. D., Ajlouni, M. A. and Chen, C. S. (1997). Secondary Compression of Peat with or without surcharging. Journal of Geotechnical and Geoenvironmental Engineering, 123(5), pp. 411-421. DOI: 10.1061/(ASCE)1090-0241(1997)123:5(411)

Mesri, G., Ajlouni, M. A., Feng, T. W. and Lo, D. O. K. (2001). Surcharging of Soft Ground to Reduce Secondary Settlement. In: C. Press, ed. Soft Soil Engineering. Illi-nois: CRC Press, pp. 55 - 65.

Tan, T. S., Inoue, T. and Lee, S. L. (1991). Hyperbolic Method for Consolidation Analysis. Journal of Geotechnical Engineering, 117(11), pp. 1729-1737. DOI: 10.1061/(ASCE)0733-9410(1991)117:11(1723)

ISSN 2961 - 5410 (Online) |

A Spring – Loaded Actuator Developed By DC 3481 Silicone / Polyaniline – Based Dielectric Polymer Film

D.M.N.T. Dissanayake[1], W.D.C.C. Wijerathne[1], S. Shakaf[1], M.A.R.L. Samaraweera[1]*, A.U. Asela[1], A.K.C.P. Premarathna[2]

[1]Department of Science and Technology, Faculty of Applied Sciences,
Uva Wellassa University, Sri Lanka.

[2]School of Engineering, University of Greenwich, United Kingdom

ABSTRACT

Dielectric polymer films play a significant role in soft robotics in actuator development. Silicone and acrylic materials are commonly used for creating dielectric polymer films with superior properties compared to other potential materials such as PVDF and Polyurethane. Published literature reports applying different fillers to enhance the electromechanical response of dielectric polymers. Starting with an already-reported novel dielectric polymer based on polyaniline/DC 3481 silicon, we report the fabrication and characterization of a spring-loaded actuator. Here we developed a simple spring-loaded actuator, and three different designs were used to optimize the actuator design. As per research outcomes, it can be concluded that paper tie-based clamping provides the best configuration for the actuator in terms of high deflection and low tendency to short-circuit. The developed actuator renders the maximum deflection of 4.19 mm at 2 kV voltage, and the actuation time is approximately 115 s. The proposed actuator is superior to many reported actuators in terms of maximum deflection and corresponding voltage. The proposed actuator and the corresponding dielectric polymer thus have potential applications in developing actuators for haptics with comparatively high deflection.

KEYWORDS: *actuators, dielectric polymers, haptic technology, DC 3481 silicon, spring-loaded*

1 INTRODUCTION

Haptic devices produce a sense of touch during human-computer interaction, and they connect users with virtual environments. Today, haptics technology has been widely applied in diverse sectors such as education, cinema, health, etc. As a sub-category of haptics, tactile displays, which are comprised of actuators, deliver cutaneous feedback (Pacchierotti et al., 2015). Here, the actuator stimulates signals to the fingertip as the friction between the fingertip and the tactile display is generated. Dielectric polymer usually increases the tactile display's wearability by reducing the unit's weight significantly, resulting in improved deflection, flexibility, power saving and degrees of freedom of the actuator (Boys et al., 2018). In an actuator setup, the dielectric polymer is mounted between two compliant electrodes where Coulombic attractions occur across the thickness of the polymer film. Compliant electrodes can be made by blending or dispersing conductive fillers (e.g., carbon black powder, graphite powder) in the insulating polymer matrix (Skov & Yu, 2018; Aradhana et al., 2020). The conductivity, simplicity, and flexibility of compliant electrodes significantly influence the performance of actuators in published works (Park et al., 2015; Boys et al., 2018). The activation mechanism of dielectric polymer-based actuators can be described via Maxwell stress and electrostriction force concepts, which outline how the alignment of dipoles and the application of Coulombic forces result in the deformation of the polymer. Moreover, the strain achieved by dielectric polymers depends on both Young's modulus and the dielectric constant.

Several commercially available dielectric polymers, such as silicone, acrylic, PVDF, and polyurethane, are used to make different actuators. Out of these, the acrylic material is difficult to modify because of its irreversible solid phase and thus, recent focus has been on the development of liquid-based dielectric polymers such as polyurethane and silicone. In this regard, silicone shows superior electromechanical properties compared to polyurethane. Furthermore, the dispersion of conductive fillers in dielectric polymers can be identified as a novel technique to enhance the polymer's electromechanical properties. Accordingly, metal fillers, ceramic fillers, carbon fillers, and metal-

ISSN 2961 - 5410 (Online) | https://doi.org/10.54389/TOFN6318

coated fillers are dispersed in the dielectric matrix to increase the dielectric constant (Liu et al., 2012, Paul et al., 2016, Nawaka & Putson, 2020; Aradhana et al., 2020).

As evident in the above discussion, silicone is a robust candidate for making dielectric polymers and it also possesses several useful properties such as low shore hardness or higher softness and the capability of making very thin polymer films. In actuator applications, silicone elastomers usually possess fast response times (around 3 s), higher efficiency, excellent viscoelastic properties, and a wide range of thermal stability than acrylic. Also, silicone dielectrics respond approximately 1000 times faster and exhibit lower mechanical losses and viscosity creep than acrylic materials. The Dow corning (DC 3481) silicone shows a larger electroactive strain out of silicone polymers. Nevertheless, its maximum strain is around 10%, which is a key limitation of using silicone elastomers in actuators (Michel et al., 2010). To address this research gap, a novel dielectric polymer was developed in our previous work by incorporating Polyaniline (PANI) fillers in a silicone matrix (Dissanayake et al., 2021), and the optimum material composition to develop the polymer was discussed. However, as described previously, it is vital to investigate the application of a polymer in an actuator, and therefore, this research work aims to fabricate a simple prototype actuator that is made of the proposed silicone dielectric polymer. In this manuscript, the materials used for dielectric polymer development and then the development strategy of the actuator are briefed initially to provide an overview of the actuator material. The characterization techniques for the polymer and the actuator are detailed next, followed by the outcomes and conclusions of the study.

2 MATERIALS AND METHODOLOGY

2.1 Preparation of the dielectric polymer film

The Dow corning or DC 3481 silicone (Siliconesandmore, Netherlands) and spherical particles (particle size: 3-100 μm) of Polyaniline (Sigma-Aldrich, Germany) were used to prepare the polymer film, while carbon conductive grease (846-80G, M.G. Chemicals, Canada) was employed to make the compliant electrode. DC 3481 and polyaniline (PANI) particles were mixed first according to the ratios in Table 1 and five samples (A-E) were obtained.

Table 6: The Weight Percentage of Polyaniline Particles in Five Samples

Sample	Weight of DC 3481 silicone (g)	Weight of Polyaniline (PANI) (g)	Weight percentage of PANI particles
A	10.00	0.00	0.0
B	10.00	0.05	0.5
C	10.00	0.10	1.0
D	10.00	0.15	1.5
E	10.00	0.20	2.0

During the experimental design as outlined in (Dissanayake et al., 2021), the maximum mixing percentage was limited to 2% (w/w) as larger mixing percentages resulted in poor curing with the hardener (i.e., DC 3481R). The mixed polymer blends were then stirred at 1000 rpm for 6 h, using a magnetic stirrer (Model: VELP SCIENTIFICA). The hardener material (i.e., DC 3481R) was then added according to the ratio DC 3481: hardener = 1:20. The dielectric polymer films with a thickness of 125 μm were then prepared using the Doctor Blade technique on polyvinylchloride (PVC) sheets following the reported works (Boyadzhieva, 2018). The optimum thickness of 125 μm was selected considering the stretchability of the polymer film and the supply voltage range. The dielectric polymer films were removed from respective PVC sheets after 24 h when the crosslinking process was completed. Carbon conductive grease was finally applied on both sides of the polymer film to make them compliant electrodes.

ISSN 2961 - 5410 (Online) |

2.2 Electromechanical Characterization of the Dielectric Polymer Film

A dielectric polymer film is usually characterized by electromechanical measurements: dielectric constant and Young's modulus. In this context, the capacitance of samples A-E were first measured using an LCR meter (Model: Proskit MT-5110) at a test frequency of 800 Hz. The dielectric constant (κ) for each sample was then computed by using the equation $\kappa = C_p \times d \,/ A\mathcal{E}_0$, where A, d, C_p, $\mathcal{E}_0$ are cross-sectional area (m^2), the thickness of the polymer film (m), capacitance (F), and permittivity of free space, respectively. Young's modulus of each sample was calculated at the first 10% elongation of stress vs. strain curves.

2.3 Fabrication of the Actuator

The spring-loaded actuator consisted of a dielectric polymer film that was attached to a plastic ring, two copper strips to connect with the power supply and a sensitive vertical spring that was placed below the polymer film. One end of the spring was fixed to a metal base while a hollow plastic ball (diameter < 5 mm) was loosely kept on the other end. The top surface of the ball was placed in such a way that it slightly made contact with the polymer film. As shown in Figure. 01, three clamping designs were tested to clamp the polymer film to the ring: (a) nut and bolt, (b) paper clips and (c) paper tie.

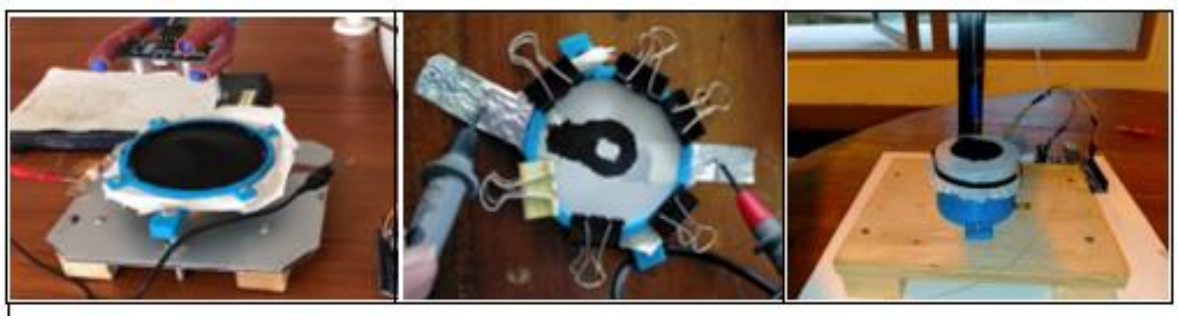

Figure. 01. Designs proposed for the clapping of the dielectric polymer film (from left to right) (a) Design I (nut/bolt) (b) Design II (paper clips) (c) Design III (cable-tie)

In Design I (Figure. 01 (a)), the actuator was stretched and placed between two rings with similar radii (10.0 cm diameter each) and clamped using a nut/bolt system. These rings were fixed to the metal base. Due to the larger radius of the ring, the energy loss was high, and the expansion was insufficient to actuate the mechanism. Furthermore, the clamping using nut/bolt assembly damaged the dielectric film and led to the film's burning due to short-circuiting even at very low voltages. In Design II (Figure 01 (b)), the ring's diameter was reduced to 7.5 cm and clamped using paper clips. This Design reduced the damage to the polymer film to some extent and still faced issues in damaging the polymer film. In Design III, as shown in Figure. 01 (c), one ring with a diameter of 5.0 cm was used and the polymer film was clamped to the ring using a cable tie. This setup was more effective than the previous designs in enabling the actuation and distinct reduction of short-circuiting.

Figure 02 illustrates the optimized actuator based on Design III. Figure 02 (a) and (b) show the stretched dielectric polymer film placed on top of the ball, which was secured using a cable tie. A layer of grease was applied on the outside of the polymer film and, that end of the electrode was extended using a copper strip. The other end of the electrode was extended by connecting the copper strip underneath the dielectric polymer film. The configuration of the spring, ball and polymer film is further elaborated in Figure 02 (c).

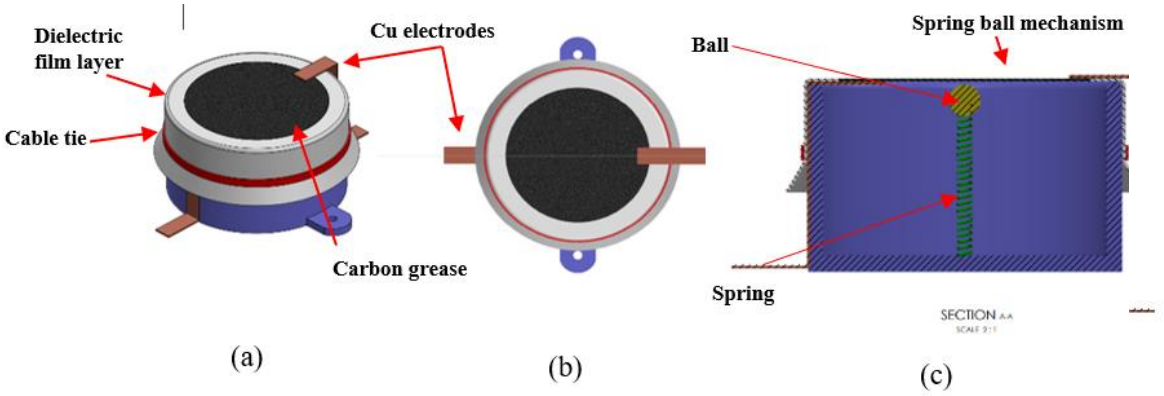

Figure 02: The schematic of the spring-loaded actuator (a) front view (b) top view (c) cross-sectional view

Figure 03 depicts the motion of this spring-loaded actuator during actuation (i.e., when an electric field is applied).

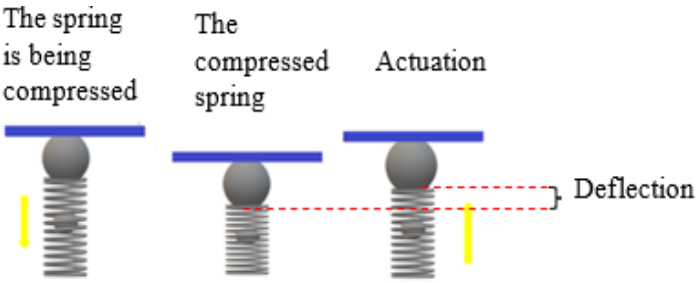

Figure 03: Schematic diagram of the working mechanism of the spring-loaded actuator

When a high voltage (usually in the kV range) is applied across the dielectric polymer film, it expands due to Maxwell stress and electrostriction (Nawaka & Putson, 2020). As a result, the spring is released from the compressed position while moving the polymer film upwards. The difference between the initial and the actuated states was taken as the deflection of the actuator, as shown in Figure. 03. When the potential difference across the polymer film reaches zero, the polymer film returns to its initial state, reducing the expanded area to the initial value. As a result, the spring compresses and the polymer film moves downwards.

2.4 Deflection of the actuator

The overall setup to measure the deflection of the actuator is shown in Figure. 04. Here, a pulsed high-voltage supply was developed by appropriately combining a series of capacitors (100 µF, 450 V) for respective experiments. Here, voltages starting from 0.68 kV were used, and the maximum voltage was recorded when the dielectric polymer film started to burn. A Lidar sensor (type: VL53L0XV2) was used to detect the deflection of the ball, and Arduino Uno was used for data processing. The noise associated with each recording was reduced using a Kalman filter (Boys et al., 2018).

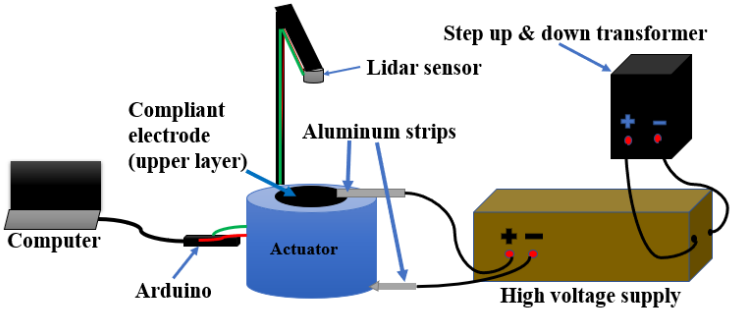

Figure 04: Setup to measure the deflection of the actuator

ISSN 2961 - 5410 (Online) |

3 RESULTS AND DISCUSSION

3.1 Electromechanical Measurements

Figure 05 shows the variation of the dielectric constant (κ) and Young's modulus (Y) with the percentage of PANI added to the polymer film. Accordingly, κ increases with the percentage of PANI and the maximum value for κ (i.e., 1.65) is achieved at 2% of PANI. The published literature using acrylic material reports the same variation of κ with the corresponding binder composition. This phenomenon can be attributed to the orientation of dipoles in the dielectric polymer film (i.e., PANI particles) towards the applied electric field, which increases the net charge while increasing κ (Nawaka & Putson, 2020).

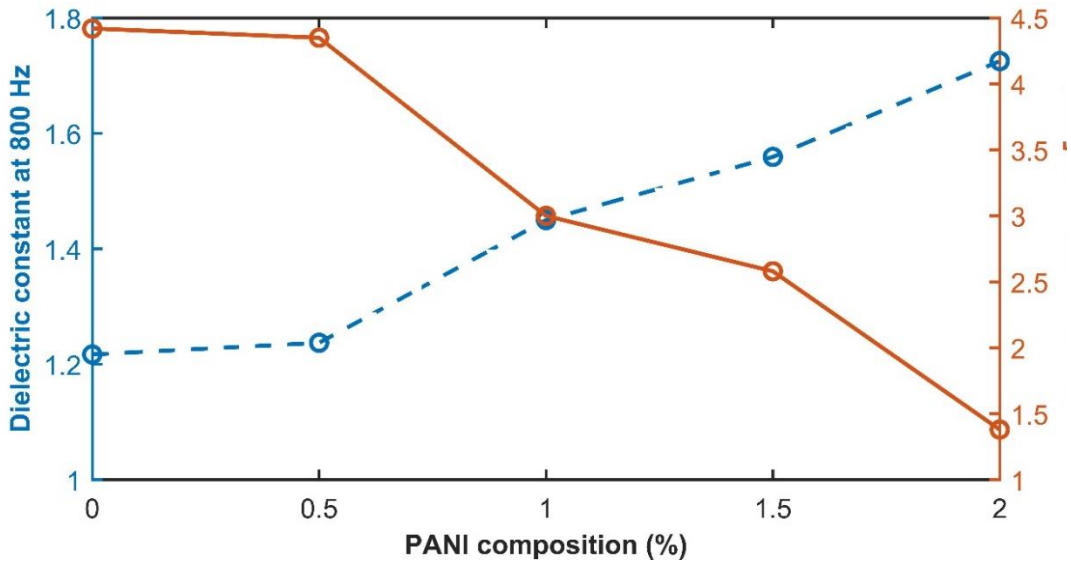

Figure 05: Variation of dielectric constant and Elastic modulus (or Young's modulus) with PANI composition

The above phenomenon can also be used to describe the observed increase of κ, where dipoles are dispersed in the DC 3481 matrix. Compared with published works (Nawaka & Putson, 2020), our results report lower values for κ. One possible reason could be the frequency of the electric field, for which our study was conducted at 800 Hz while the reported work was conducted at 1 Hz. Furthermore, Young's modulus (Y) decreases with the percentage of PANI, and the lowest value was obtained at 2% (w/w) composition. This variation of Young's modulus (Y) also agrees with the reported findings (Nawaka & Putson, 2020). As lower Young's modulus and higher dielectric constant values promote the applicability of dielectric polymer films for haptics, the best composition for the polymer film is identified as 2% (w/w) of PANI.

3.2 Deflection of the Actuator

Figure 06 shows the actuator deflection with time at different voltage values. The experimental voltage-supply setup generated 0.68 kV, 1.36 kV, and 2.0 kV voltage, and the maximum voltage was identified when the polymer film started to burn. For 0.68 kV and 1.38 kV, the actuator deflection is less than 0.5 mm and a significant increase in deflection is not detected throughout the inspected period. However, at 2 kV, the deflection is around 1 mm for the first 95 s and then increases drastically to 4.19 mm within about the next 20 s.

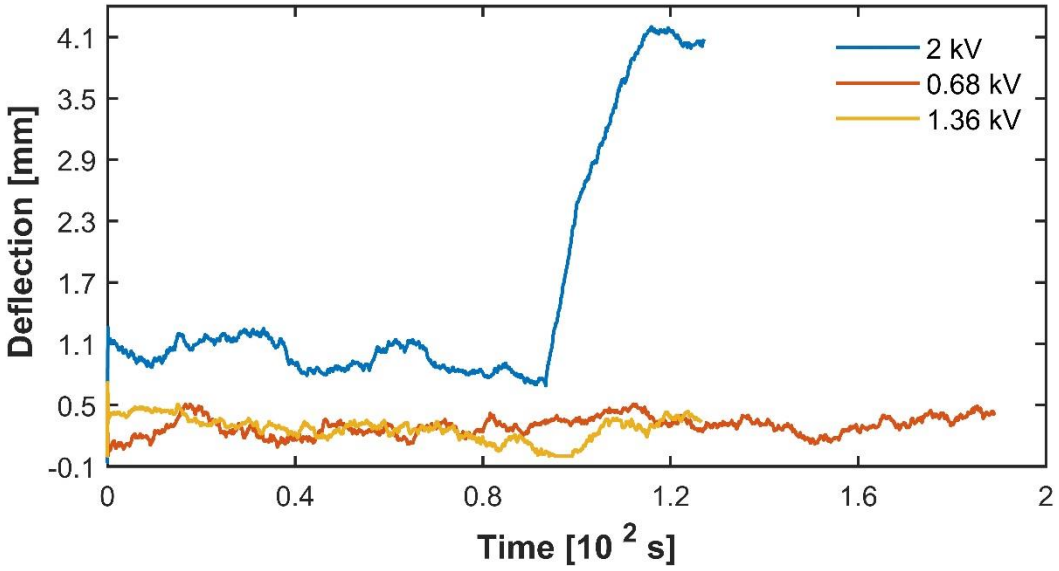

Figure 06: The variation of actuator deflection with time at different voltages

The deflections rendered by several reported actuators made from distinct dielectric polymers are shown in Figure. 07 to further highlight the performance of the developed actuator. Accordingly, most polymers result in actuator displacement in mm scale and the displacement tends to increase with voltage. Furthermore, the highest displacement (i.e., 6.0 mm) is recorded from the actuator made of Terpolymer and 2-(ethylhexyl) phthalate. This actuator requires approximately 1 kV to yield such displacement. On the other hand, the lowest displacements (in µm scale) correspond to actuators made from polyurethane. In this regard, the proposed actuator shows a 4.19 mm displacement at 2 kV. Thus, the actuator displacement of this work is only inferior to dielectric polymers made of Terpolymer and 2-(ethylhexyl) phthalate.

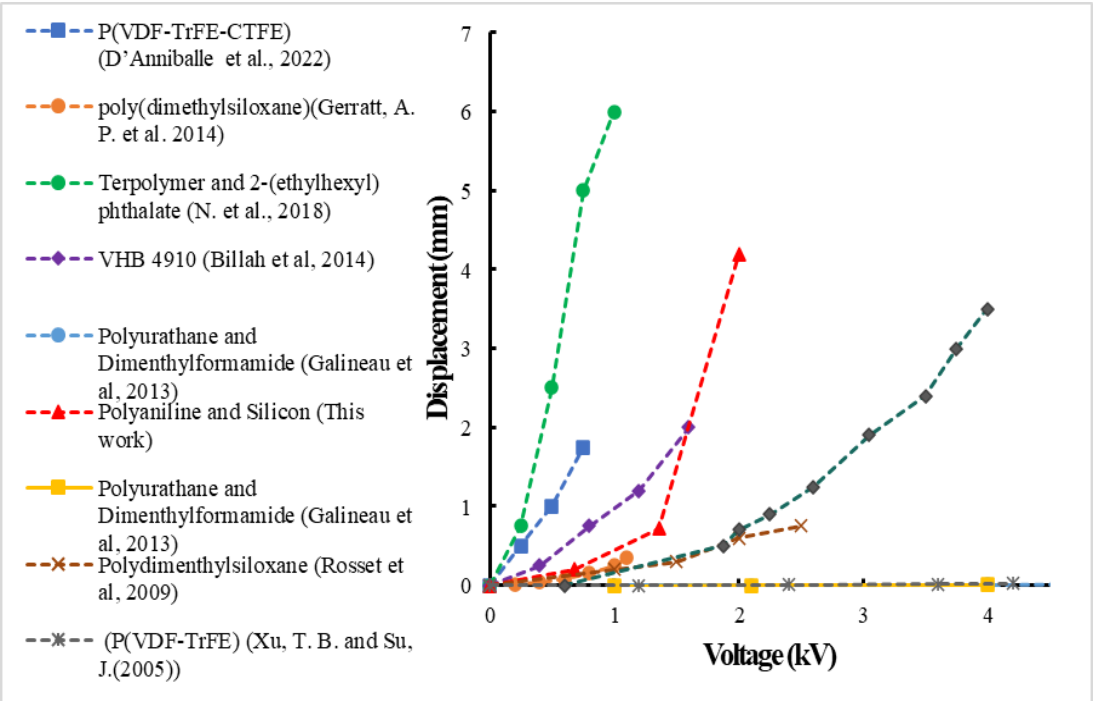

Figure 07: Comparison of deflections generated by different actuators

ISSN 2961 - 5410 (Online) |

4 CONCLUSION

This work investigated the extension of a newly developed dielectric polymer to fabricate a spring-loaded actuator composed of a plastic ring, dielectric polymer film and a spring/ball unit. The following conclusions can be drawn from this study.

1. Cable-tie clamping design for the polymer film and plastic ring works best to develop the actuator.
2. The actuator deflection reaches a maximum of 4.19 mm within 115 s at 2 kV actuation voltage.
3. The deflection of the actuator is superior to most reported actuators.

In future, by using a suitable numerical model, the force and vibratory stimulations of the actuator will be investigated to identify unexplored electromechanical and thermal features of the dielectric polymer. Accomplishing a considerable deflection is also targeted as future work which may be done through fabricating stacked later actuators. Moreover, the introduced actuator could be miniaturized and extended for wearable tactile displays while modifying the insulation technology of the actuator as a safety measure.

REFERENCES

C. Pacchierotti, L. Meli, F. Chinello, M. Malvezzi, and D. Prattichizzo (2015), "Cutaneous haptic feedback to ensure the stability of robotic teleoperation systems," The International Journal of Robotics Research, vol. 34, no. 14, pp. 1773-1787.

V. Khoshkava, J. M. C. Hernandez, and V. Levesque (2020), "Local haptic actuation system," ed: Google Patents.

R. Aradhana, S. Mohanty, and S. K. Nayak (2020), "A review on epoxy-based electrically conductive adhesives," International Journal of Adhesion and Adhesives, vol. 99, pp. 102596.

A. L. Skov and L. Yu (2018), "Optimization techniques for improving the performance of silicone-based dielectric elastomers," Advanced Engineering Materials, 20(5), p. 1700762.

H. Boys, G. Frediani, M. Ghilardi, S. Poslad, J. C. Busfield, and F. Carpi (2018), "Soft wearable non-vibratory tactile displays," in 2018 IEEE International Conference on Soft Robotics (RoboSoft), pp. 270- 275: IEEE

W.-H. Park, T.-H. Yang, Y. Yoo, S. Choi, and S.-Y. Kim (2015), "Flexible and bendable vibrotactile actuator using electroconductive polyurethane," in 2015 IEEE World Haptics Conference (W.H.C.), pp. 165-170: IEEE.

D. M. N. T. Dissanayake, Asela, A.U., Premarathna, A.K.C.P., Tennakoon, G.A.A.I. and Samaraweera, and M.A.R.L. (2021), "Development of a Silicone Dielectric Polymer for Actuator," in 5th International Research Conference of Uva Wellassa University (IRCUWU 2021), Badulla, Sri Lanka, 2021, pp. 307, Uva Wellassa University: Uva Wellassa University.

S. Boyadzhieva, S. C. Fischer, S. Lösch, A. Rutz, E. Arzt, and K. Kruttwig (2018), "Thin film composite silicon elastomers for cell culture and skin applications: manufacturing and characterization," Journal of Visualized Experimentsm , 137, pp. e57573.

K. Nawaka and C. Putson (2020), "Enhanced electric field induced strain in electrostrictive polyurethane composites fibers with polyaniline (emeraldine salt) spider-web network," Composites Science and Technology, 198, pp. 108293.

J. Stejskal *et al.*, "Conducting polymers: polyaniline," *Encyclopedia of polymer science and technology*, pp. 1-44, 2002.

Xie, X. *et al.* (2017) 'A Review of Smart Materials in Tactile Actuators for Information Delivery', *arXiv*, pp. 1–13.

Michel, S., Zhang, X. Q., Wissler, M., Löwe, C., & Kovacs, G. (2010). A comparison between silicone and acrylic elastomers as dielectric materials in electroactive polymer actuators. Polymer International, 59(3), pp. 391–399.

ISSN 2961 - 5410 (Online) |